UNIVERSITY OF OKLAHOMA

GRADUATE COLLEGE

QUANTITATIVE ANALYSIS OF RAPID-SCAN PHASED ARRAY WEATHER RADAR BENEFITS AND DATA QUALITY UNDER VARIOUS SCAN CONDITIONS

A DISSERTATION

SUBMITTED TO THE GRADUATE FACULTY

in partial fulfillment of the requirements for the

Degree of

DOCTOR OF PHILOSOPHY

By

WILLIAM ANDREW MAHRE

Norman, Oklahoma

2020

QUANTITATIVE ANALYSIS OF RAPID-SCAN PHASED ARRAY WEATHER RADAR BENEFITS AND DATA QUALITY UNDER VARIOUS SCAN CONDITIONS

A DISSERTATION APPROVED FOR THE
SCHOOL OF METEOROLOGY

BY THE COMMITTEE CONSISTING OF

Dr. Robert Palmer, Chair

Dr. Tian-You Yu, Co-Chair

Dr. David Bodine

Dr. Cameron Homeyer

Dr. Phillip Chilson

Dr. Mark Yeary

Acknowledgments

First, I would like to thank Dr. Tian-You Yu and Dr. David Bodine for meeting with me regularly and providing valuable guidance in all aspects of this project for the past several years. I would also like to thank my committee chair, Dr. Robert Palmer, for his support and feedback. Additionally, I would like to acknowledge Dr. Boonleng Cheong for his help with several aspects of this research, including (but not limited to) development of SimRadar, creating several plotting and visualization scripts, and helping to troubleshoot/modify SimRadar for this project.

Additionally, I would like to thank my parents, Peter Mahre and Valerie Mahre, for always supporting me from a young age. Finally, I would like to thank my wife Kimberlee for her unwavering support, for moving with me to Norman so I could pursue this degree, and for putting up with the long hours I've spent studying and working on my research. I couldn't have done this without her support (and the support of our two dogs, Minka and Clover).

This project was supported by NOAA/Oceanic and Atmospheric Research under NOAA-University of Oklahoma Cooperative Agreement #NA16OAR4320115, U.S. Department of Commerce, as well as the OU Graduate College's Bullard Dissertation Completion Fellowship.

Table of Contents

Acknowledgments **iv**

List Of Tables **vii**

List Of Figures **viii**

Abstract **xiii**

1 Introduction and Background **1**
1.1 Background and Motivation 1
1.2 Previous and Ongoing Research on Rapid-Scan PAR and Signal Processing Techniques 7
1.2.1 Weather Radar Testbeds and Demonstrators 7
1.2.2 Potential Radar Design Architectures 8
1.2.3 Signal Processing Techniques and Scanning Strategies 12
1.3 Goals 18

2 Effect of Scanning Strategy Choice on PAR Data Quality **20**
2.1 Introduction to Data Quality Assessment 20
2.1.1 Background and Previous Research 20
2.2 Methods 25
2.2.1 Radar Simulator (RSim) 25
2.2.2 Data Quality 29
2.3 Results 33
2.3.1 Data Quality and Error Estimation 33
2.3.1.1 Radar Reflectivity Factor (Z_H) 36
2.3.1.2 Radial Velocity (v_r) 44
2.3.2 Effect of Beam Spoiling on Mesocyclone Intensity Observations 50
2.4 Conclusions 55

3 Quantifying the Benefits of a Rapid-Scan PAR for Tornado Detection **60**
3.1 Rapid-Scan Introduction 60
3.1.1 Background 61
3.1.2 Previous Research on Rapid-Scan Benefits 64
3.2 High-Resolution Observations of TDS & TVS Growth 65
3.2.1 Methods 66

3.2.1.1 SimRadar . . . 66
3.2.1.2 Cloud Model 1 (CM1) . . . 71
3.2.1.3 Hydrometeor Classification Algorithm with Tornado Class . . . 71
3.2.2 Results . . . 75
3.2.2.1 CM1 Evolution: TVS and Vertical Velocity . . . 75
3.2.2.2 High-Resolution Observations of TDS Growth: Small Debris Initiation Domain . . . 77
3.2.2.3 High-Resolution Observations of TDS Growth: Large Debris Initiation Domain . . . 92
3.3 Estimating Tornado Detection Latency Time . . . 103
3.3.1 Methods . . . 104
3.3.1.1 Large-Eddy Simulation (LES) . . . 104
3.3.1.2 Tornado Detection Latency Time Calculation . . . 106
3.3.2 Results . . . 108
3.4 Conclusions . . . 114

4 Adaptive Scanning and Pulse Reallocation to Improve Data Quality 119
4.1 Introduction . . . 119
4.2 Methods . . . 123
4.2.1 Overview of Optimization Procedure . . . 123
4.2.2 Optimization and Cost Function Setup . . . 125
4.2.3 Datasets Analyzed . . . 129
4.3 Results . . . 131
4.3.1 Case #1: 16 May 2015 'Tipton, OK Tornadic Supercell' . . . 131
4.3.2 Case #2: 6 July 2015 'South Dakota MCS' . . . 140
4.4 Conclusions . . . 146

5 Conclusions and Future Work 150
5.1 Summary & Conclusions . . . 150
5.2 Future Work . . . 157

Bibliography 160

Appendix A
Effect of Beam Multiplexing on Radar Reflectivity Factor Variance Distribution . . . 172

List Of Tables

2.1 A list of the WRF model parameterizations used in this study. 27
2.2 A summary of the SENSR PPR for reflectivity factor, radial velocity, and spectrum width maximum standard deviation for a specified SNR and true spectrum width (σ_v). 32
2.3 A list of RSim scan parameters used in this study. 35

3.1 A summary of the five cases run in SimRadar for this study. 79

List Of Figures

1.1 NEXRAD coverage of the CONUS. Figure adapted from the NOAA Radar Operations Center (ROC). 2

1.2 A subset of possible designs for the NexPAR network. PD-1 and PD-2 represent a more dense network of smaller radars, similar in concept to the CASA system (McLaughlin et al. 2005). PD-3 closely resembles NEXRAD and the WSR-88D radars, and would essentially replace the parabolic dishes in NEXRAD with a planar PAR. PD-4 is a four-faced PAR, where each face covers a 90° sector. Figure from Weber et al. (2019). 11

1.3 Various scan modes available with PARs: beam multiplexing, radar imaging and digital beamforming, adaptive scanning, and the multiple-beam technique. 15

2.1 Improvement factor for Z_H (panel a) and v_r (panel b) as a function of SNR using BMX. The 3 lines represent spectrum width of 1 m s^{-1} (black line), 3 m s^{-1} (blue line), and 5 m s^{-1} (red line). 31

2.2 PPIs showing a) horizontal reflectivity factor (Z_H, in dBZ), b) radial velocity (in m s^{-1}), c) estimated spectrum width (in m s^{-1}), and d) signal-to-noise ratio (SNR, in dB). All PPIs are shown at 0124:00 UTC. Mean spectrum width is 2.48 m s^{-1}. The black contour corresponds to the region where Z_H is greater than 38 dBZ. . . . 34

2.3 PPIs showing the calculated RMSE of Z_H for a) a pencil beam using CPS with a scan time of 20 s per PPI, b) a pencil beam using CPS with a scan time of 10 s per PPI, c) a pencil beam using BMX (IPS) with a scan time of 20 s per PPI, and d) a 10° fan beam using CPS with a scan time of 20 s per PPI. All PPIs are at 0124:00 UTC, at 0.5° in elevation. The RMSE listed in each panel is the mean RMSE for 15 realizations of each scan method; these values may deviate from the mean RMSE of the PPI shown by up to 0.01 dBZ. 37

2.4 Histogram of mean Z_H RMSE estimates at 5 times and 3 elevation angles (0.5°, 4.0°, and 8.0°). The black vertical line represents the 1 dBZ suggested requirement (see Table 2.2). 38

2.5 PPIs showing the reference Z_H fields with the expected standard deviation added as AWGN. Note that the underlying reference field is different in panel d), due to the lowered sensitivity and higher antenna sidelobes. 40

2.6 As in Fig. 2.3, but for RMSE of v_r. RMSE values listed are the mean values from 15 PPIs, and may deviate from the mean RMSE of the PPI shown by up to 0.01 m s^{-1}. 45
2.7 As in Fig. 2.4, but for a histogram of v_r. The black vertical line represents the 1 m s^{-1} suggested requirement (see Table 2.2). 46
2.8 As in Fig. 2.5, but for v_r. 47
2.9 This figure plots the underlying Z_H reference fields for a pencil beam (top left), as well as those for a beam spoiled by 5°, 10°, and 20° in azimuth. Note the loss in sensitivity as beam spoiling is increased. . . 51
2.10 As in Fig. 2.9, but for v_r. The value for ΔV in each panel corresponds to the measured mesocyclone intensity with each amount of beam spoiling. 52
2.11 The azimuthal radial velocity profile across the rotational couplet at 0.5° in elevation (approximately 300 m AGL). Note that increasing the beam spoiling factor tends to decrease the measured ΔV velocity shear. 53
2.12 As in Fig. 2.10, but for spoiling in elevation, rather than azimuth. . . 54

3.1 RCS factor as a function of the height of the debris above ground level. Note that above ∼30 m AGL, over 90% of the RCS factor is 'activated'. 68
3.2 Example output from SimRadar. Panels show radar reflectivity factor (Z_H), radial velocity (v_r), HCA class, and correlation coefficient (ρ_{hv}). 70
3.3 A generalized membership function for variable x for a random class. Figure adapted from Snyder and Ryzhkov (2015). 73
3.4 The maximum vertical velocity at 15, 55, and 135 m AGL at each CM1 timestep (10 s apart). 76
3.5 The 99.9^{th} percentile of vertical velocity at 15, 55, and 135 m AGL at each CM1 timestep (10 s apart). 77
3.6 An analysis of ΔV near the domain center at 0.5°, 1.3°, and 2.4°. The ΔV is derived for a low-debris case, to minimize debris drag-induced bias. Note that the elevations/heights in this figure do not correspond to the heights listed in Figs. 3.4 and 3.5. 78
3.7 SimRadar output at 1-min temporal resolution. Note the significant frame-to-frame increase in Z_H (223 s to 283 s), rotational intensity (163 s to 223 s), and TDS area (163 s to 223 s, and 223 s to 283 s). . 80
3.8 SimRadar estimated ρ_{hv} for Case I at 0.5° and 1.8°. The time stagger/offset between 0.5° and 1.8° is due to the time taken to complete the 'rest' of the PPI. 83
3.9 As in Fig. 3.8, but for output from the hydrometeor classification algorithm. 84

3.10 A plot of the area of pixels corresponding to a TDS classification at various elevations as a function of time, for Case I. Elevations of TDS area plotted are 0.5°, 1.3°, 1.8°, and 2.4° (approximately 140 m, 340 m, 470 m, and 620 m AGL, respectively). The plotted ΔV is for Case III, such that debris-induced bias of ΔV is minimized. All times are relative to the start of the simulation. 85
3.11 SimRadar estimated ρ_{hv} for Case II at 0.5° and 1.8°. The time stagger/offset between 0.5° and 1.8° is due to the time taken to complete the 'rest' of the PPI. 88
3.12 As in Fig. 3.11, but for output from the hydrometeor classification algorithm. 89
3.13 As in Fig. 3.10, but for Case II. The plotted ΔV is for Case III such that debris-induced bias of ΔV is minimized. 90
3.14 SimRadar estimated ρ_{hv} for Case III at 0.5° and 1.8°. The time difference between the 0.5° and 1.8° scans is due to the delay in debris lofting between subsequent levels. 93
3.15 As in Fig. 3.14, but for output from the hydrometeor classification algorithm. 94
3.16 A plot of the area of pixels corresponding to a TDS classification at various elevations as a function of time, for Case III. Elevations of TDS area plotted are 0.5°, 1.3°, 1.8°, and 2.4° (approximately 140 m, 340 m, 470 m, and 620 m AGL, respectively). All times are relative to the start of the simulation. 96
3.17 SimRadar estimated ρ_{hv} for Case IV at 0.5° and 1.8°. The time difference between the 0.5° and 1.8° scans is due to the delay in debris lofting between subsequent levels. 98
3.18 As in Fig. 3.17, but for output from the hydrometeor classification algorithm. 99
3.19 As in Fig. 3.16, but for Case IV. The plotted ΔV is for case III such that debris-induced bias of ΔV is minimized. 100
3.20 SimRadar estimated ρ_{hv} for Case V at 0.5° and 1.8°. The time difference between the 0.5° and 1.8° scans is due to the delay in debris lofting between subsequent levels. 101
3.21 As in Fig. 3.20, but for output from the hydrometeor classification algorithm. 102
3.22 As in Fig. 3.16, but for Case V. The plotted ΔV is for case III such that debris-induced bias of ΔV is minimized. 103
3.23 An example showing the TDS area with time for a slow VCP (VCP A; 267 s update time, red line) and a fast VCP (VCP B; 53.4 s update time, green line). Note the fluctuations in TDS area for VCP B, leading to TDS latency times greater than the theoretical values. . . . 110
3.24 Histograms of bootstrapped means for TDS latency time with a low debris count (panel a) an a higher debris concentration (panel b). . . 112

3.25 A comparison of the changes in ρ_{hv} with 25 pulses per radial (panel a) and with 5 pulses per radial (panel b). 114

4.1 A high-level overview of the procedure for optimization in the proposed ROI^2 model. 124
4.2 A PPI of Z_H from 16 May 2015 at 2302 UTC, from the KFDR (Frederick, OK) NEXRAD radar. The black contour represents an SNR of 15 dB. Only 200 km x 200 km are plotted, as the example optimization shown herein only analyzes the nearest 100 km to the radar. . . . 131
4.3 As in Fig. 4.2, but for the case from 6 July 2015 at 0401 UTC, from the KFSD NEXRAD radar. 132
4.4 The regions which were segmented as being either 'high importance' or 'medium importance' for Case #1. This figure plots Z_H (in dBZ) for the high and medium importance regions only. In this example, the region to the northwest of the radar was classified as 'high importance', and the storm to the southwest of the radar was classified as 'medium importance'. 134
4.5 The importance level by radial, after region segmentation has been performed in Case #1. The storm to the northwest of the radar has been subjectively classified as high importance (10 out of 10) and the storm to the southwest of the radar has been classified as medium importance (7 out of 10). All other areas are classified as minimal importance (2 out of 10). 135
4.6 The 'new' number of pulses per radial after PR has been performed for Case #1. 136
4.7 A comparison of σ_{vel} before and after PR has been performed for Case #1. The black circled areas represent regions where data quality has improved by using PR, and red circles represent areas where data quality has gotten worse because of PR (generally in the regions of minimal importance). Black dashed lines represent the edges of the various regions in Fig. 4.5. 138
4.8 A measure of the difference in σ_{vel} before and after PR for Case #1. Blue (red) regions represent areas where data quality has gotten better (worse). 139
4.9 A comparison of data quality both before and after PR in each region type. The red line represents data before PR, and the blue line represents data after PR. 141
4.10 The regions which were segmented as being higher importance for Case #2. This figure plots Z_H (in dBZ) for the high importance region only. In this example, a portion of the MCS was classified as 'high importance', while the rest of the PPI was classified as minimal importance. 142

4.11 The 'new' number of pulses per radial after PR has been performed for Case #2. 143
4.12 As in Fig. 4.7, but for a comparison of σ_{vel} before and after PR has been performed for Case #2. 144
4.13 A measure of the difference in σ_{vel} before and after PR for Case #2. Blue (red) regions represent areas where data quality has gotten better (worse). 145

Abstract

Currently, NEXRAD provides weather radar coverage for the contiguous United States. It is believed that a replacement system for NEXRAD will be in place by the year 2040, where a major goal of such a system is to provide improved temporal resolution compared to the 5–10-min updates of NEXRAD. In this dissertation, multiple projects are undertaken to help achieve the goals of improved temporal resolution, and to understand possible scanning strategies and radar designs that can meet the goal of improved temporal resolution while either maintaining (or improving) data quality. Chapter 2 of this dissertation uses a radar simulator to simulate the effect of various scanning strategies on data quality. It is found that while simply reducing the number of pulses per radial decreases data quality, other methods such as beam multiplexing and radar imaging/digital beamforming offer significant promise for improving data quality and/or temporal resolution. Beam multiplexing is found to offer a speedup factor of 1.7–2.9, while transmit beam spoiling by 10° in azimuth can offer speedup factors up to ∼4 in some regions. Due to various limitations, it is recommended that these two methods be used judiciously for rapid-scan applications.

Chapter 3 attempts to quantify the benefits of a rapid-scan weather radar system for tornado detection. The first goal of Chapter 3 is to track the development of a common tornado signature (tornadic debris signature, or TDS) and relate it to developments in tornado strength. This is the first study to analyze the evolution

of common tornado signatures at very high temporal resolution (6 s updates) by using a storm-scale tornado model and a radar emulator. This study finds that the areal extent of the TDS is correlated with both debris availability and with tornado strength. We also find that significant changes in the radar moment variables occur on short (sub-1-min) timescales. Chapter 3 also shows that the calculated improvement in tornado detection latency time (137–207 s) is greater than that provided by theory alone (107 s). Together, the two results from Chapter 3 emphasize the need for sub-1-min updates in some applications such as tornado detection. The ability to achieve these rapid updates in certain situations will likely require a combination of advanced scanning strategies (such as those mentioned in Chapter 2) and adaptive scanning.

Chapter 4 creates an optimization-based model to adaptively reallocate radar resources for the purpose of improving data quality. This model is primarily meant as a proof of concept to be expanded to other applications in the future. The result from applying this model to two real-world cases is that data quality is successfully improved in multiple areas of enhanced interest, at the expense of worsening data quality in regions where data quality is not as important. This model shows promise for using adaptive scanning in future radar applications.

Together, these results can help the meteorological community understand the needs, challenges, and possible solutions to designing a replacement system for NEXRAD. All of the techniques studied herein either rely upon (or are most easily achieved by) phased array radar (PAR), which further emphasizes the utility of PAR

for achieving rapid updates with sufficient data quality. It is hoped that the results in this dissertation will help guide future decisions about requirements and design specifications for the replacement system for NEXRAD.

Chapter 1

Introduction and Background

1.1 Background and Motivation

Currently, high-resolution weather radar data is collected across the United States by the Next-Generation Radar system, or NEXRAD (Fig. 1.1). This system was designed in the late 1980s, and was installed nation-wide in the early 1990s to provide weather radar data for the majority of the Continental United States (CONUS). As of the year 2020, NEXRAD is approaching the end of its lifecycle. There is currently a service-life extension program (SLEP) underway to ensure that NEXRAD can persist through 2040. If a new radar system is to replace NEXRAD in the late 2030s, a design decision will need to be made by approximately 2028 (Weber et al. 2019). To meet this goal, there is fundamental research ongoing into polarimetric calibration for phased array radar (PAR; Ivić 2018; Ivić and Schvartzman 2020), data collection from similar, prototype-style systems (Weber et al. 2020; Torres et al. 2020), assessment of rapid-scan PAR benefits (Heinselman et al. 2012; Wilson et al. 2017; Cho and Kurdzo 2019; Kurdzo et al. 2020), and research of potential signal processing techniques (Yu et al. 2007; Melnikov et al. 2015; Zrnić et al. 2015). The research in this dissertation is designed to provide insight into some of the design

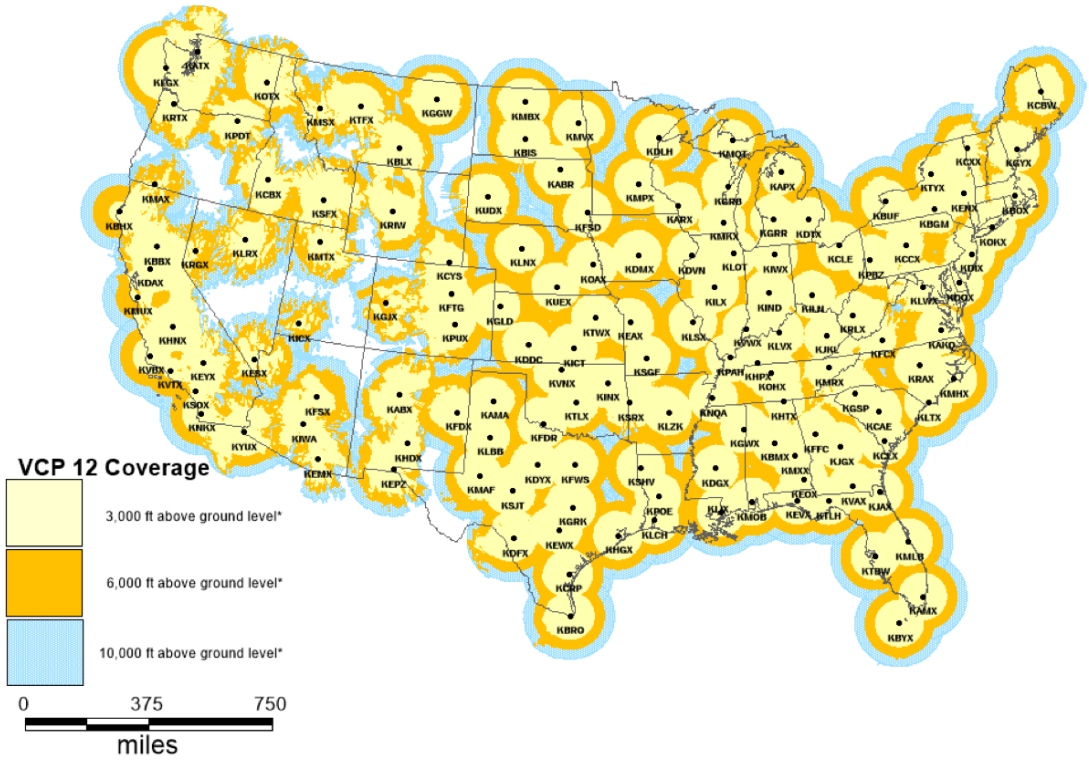

Figure 1.1: NEXRAD coverage of the CONUS. Figure adapted from the NOAA Radar Operations Center (ROC).

considerations for a replacement system (hereinafter referred to as 'NexPAR', in reference to the relatively high likelihood of a NEXRAD replacement system being a PAR).

It is a stated goal of the National Weather Service (NWS) to improve the temporal resolution relative to NEXRAD. According to the initial performance requirements for a similar system (Federal Aviation Administration 2017), desired temporal resolution is 1 min. This represents an approximate 5-fold improvement in

full-volume update time, as NEXRAD volumetric update times are generally ∼4–7 min for precipitation modes (NOAA OFCM 2017). Such a significant reduction in volumetric update time is believed to offer many advantages for meteorological operations. For example, Heinselman et al. (2012) and Wilson et al. (2017) have shown that the introduction of rapid scans with a phased array radar (PAR) leads to increased warning lead time, improved forecaster confidence, a higher probability of detection, and a lower false alarm ratio for tornadoes in a simulated operational setting. Wolfson and Meuse (1993) found that higher temporal resolution (3 min to 1 min) also improves warning lead time for low-level wind shear detection for aviation applications (2.2 min to 5.2 min). Also, data assimilation studies have shown the benefit of assimilating rapid-scan weather radar data to improve short-term numerical weather prediction (NWP) model accuracy (Yussouf and Stensrud 2010; Sun et al. 2014; Supinie et al. 2017), which could have important implications for future warning paradigms such as Warn-on-Forecast System (WoFS Lawson et al. 2018).

While the introduction of NEXRAD greatly improved warning lead time (Polger et al. 1994; National Research Council 1995; Bieringer and Ray 1996; Simmons and Sutter 2005), the lead time for warnings has remained largely stagnant since the mid-2000s, and has even decreased since 2012, likely due to an increased NWS emphasis on reducing false-alarm ratio (Brooks and Correia Jr. 2018). A lack of improvement in lead time is an issue for the NWS, as it has been shown that there is a statistically significant link between increased tornado warning lead time and a lower number of

injuries caused by tornadoes (Simmons and Sutter 2008). Because severe storms and tornadoes tend to evolve on timescales much faster than the 4–7-min VCP update time of NEXRAD (e.g., Carbone et al. 1985; French et al. 2013; Wurman and Kosiba 2013; French et al. 2014; Houser et al. 2015; Wakimoto et al. 2015; Tanamachi and Heinselman 2016; Kurdzo et al. 2017; Mahre et al. 2018; Bluestein et al. 2019; Griffin et al. 2019; Wakimoto et al. 2020), improved temporal resolution is a priority for the NWS for accurately issuing warnings and advisories. For example, rapid updates are especially important for accurate quantitative precipitation estimation (QPE), because urban flood and flash flood predictions rely on fast volumetric updates, as watersheds can respond rapidly to changes in rainfall (Wang and Chandrasekar 2010).

High-temporal-resolution weather radar data has also been shown to be essential for many research applications. As previously stated, tornadoes evolve on much faster timescales than the typical NEXRAD volumetric update time. Several radar-based studies on the dynamics of tornadoes (e.g., French et al. 2013; Wurman and Kosiba 2013; French et al. 2014; Houser et al. 2015; Kurdzo et al. 2017; Mahre et al. 2018; Bluestein et al. 2019; Griffin et al. 2019; Mahre et al. 2019) have shown that the dynamics of tornadoes can change significantly in less than a minute. For example, Mahre et al. (2018) found that debris lofting in and around an EF-3 tornado occurs rapidly, such that significant changes are observed at $\sim$30 s updates (Fig. 6 of Mahre et al. 2018). Using the same radar, Griffin et al. (2019) observed changes in tornado intensity and tilt at $\sim$10 s temporal resolution (their Figs. 5

and 8). French et al. (2013) also found that changes in tornadogenesis occur on very rapid timescales, by using 10 s volumetric data from a mobile radar to track the vertical development of a tornado. Additionally, Mahre et al. (2019) found that in several tornadoes, there appears to be a statistically significant oscillation in tornado intensity with a period of approximately 60–90 s. To properly observe this phenomenon (following the Shannon-Nyquist sampling theorem), the radar update time must be no longer than 30 s. Despite the evidence that many meteorological phenomena such as tornadoes require an update time of less than 1 min for proper observations, even 1-min updates would be more helpful for research applications than the current ∼5-min updates offered by NEXRAD. However, the results of these studies do underscore the point that in certain situations, updates faster than 1 min are desirable. With a PAR, adaptive scanning could allow for even faster updates if the need arises.

As a result of the growing body of evidence that improved temporal resolution (beyond 5-min updates) is essential for both research and operations, the NWS has expressed a desire to have volumetric updates on the order of 1 min. However, a 5-fold reduction in update time presents several challenges regarding the design of the NexPAR system. For example, a reduction in volumetric update time corresponds to poorer data quality (Mahre et al. 2020) and/or reduced volumetric coverage (Chrisman 2009; Heinselman and Torres 2011). This represents a challenge, as other techniques will have to be employed in order to achieve rapid updates without sacrificing data quality while still scanning the full volume. The exact speedup

factor necessary will depend upon radar architecture and the percentage of scan timeline available for weather observations, but initial estimates speculate that a scan speedup factor of 1.25–5x will be necessary relative to NEXRAD (Zrnić et al. 2015; Weber et al. 2017; Mahre et al. 2020).

To achieve these speedup factors, significant changes will have to be made to the design and signal processing of a NexPAR system. For example, mechanical limitations would not allow for a single radar (either PAR or parabolic dish) to be mechanically rotated at the rate necessary to achieve 1-min volumetric updates without significantly modifying the signal processing techniques or the volume coverage pattern. For example, the Rapid-Scan X-Pol Radar (RaXPol; Pazmany et al. 2013) uses a technique called frequency hopping to increase the number of independent samples per radial by transmitting pulse pairs in rapid succession, with each pulse pair shifted in frequency by a minimum of the pulse bandwidth to increase sample independence.

To achieve desired data quality, techniques other than simply altering the mechanical rotation rate need to be used to achieve the desired scan speedup. More information about possible radar architectures and scan techniques is provided in the following section.

1.2 Previous and Ongoing Research on Rapid-Scan PAR and Signal Processing Techniques

1.2.1 Weather Radar Testbeds and Demonstrators

To test the potential for a PAR solution as a NEXRAD replacement, multiple real-world radar systems have been used. One of the first PARs used for meteorological observations was the National Weather Radar Testbed (NWRT; Forsyth et al. 2005). The NWRT was an S-band PAR, where the antenna (SPY-1A) was originally deployed on a U.S. Navy ship. The NWRT became fully available to the research community in May 2004, and was the first PAR available to the meteorological research community on a full-time basis (Forsyth et al. 2005). The NWRT collected data on multiple meteorological cases, including tornadoes, intense storms, and other cases in which rapid-scan PAR data are useful (Forsyth et al. 2005; Zrnić et al. 2007; Heinselman et al. 2008; Newman and Heinselman 2012; Tanamachi et al. 2015; Kuster et al. 2016). These studies have shown the importance of rapid scanning radar for case studies of various phenomena, and much of the analysis conducted in those studies are only made possible by ∼1-min volumetric update times. Forecasters have evaluated the rapid-scan radar data and have generally determined that the faster updates are useful for operations. Perhaps most importantly, the NWRT was used to test various scanning strategies, algorithms, and signal processing techniques (e.g., Yu et al. 2007; Heinselman and Torres 2011; Curtis and Torres 2011;

Lakshmanan et al. 2013); the results from some of these studies will be discussed in Section 1.2.3.

The SPY-1A antenna was decommissioned in 2016, and the pedestal and radome which formerly housed the NWRT has been used to house the Advanced Technology Demonstrator (ATD; Torres et al. 2020). This demonstrator is the first full-scale, active, polarimetric, electronically scanned PAR for meteorological observations. It is a goal of the ATD to properly characterize PAR polarimetric performance and calibration, technology maturity, and the ability for a similar PAR system to meet the needs of the NWS (Torres et al. 2020). This work is especially important, as the exact design for a NexPAR system is still unknown (Weber et al. 2019; Weber and Herd 2019). For example, it is unknown if a NexPAR system would consist of a dense network of smaller radars, a NEXRAD-style network comprised of single-faced mechanically rotating PARs, or a NEXRAD-style network of four-faced PARs that electronically beamsteer, without any mechanical rotation in azimuth or elevation. By using the ATD, we can better assess the feasibility for a PPAR system for a full-scale, nationwide network of radars.

1.2.2 Potential Radar Design Architectures

As previously stated, the improvement in temporal resolution from $\sim$5 min to $\sim$1 min provides some challenges to preserve data quality while achieving fast updates. In this section, some of the research and techniques that have been studied

for rapid-scan PAR systems are detailed, and their feasibility for obtaining rapid updates for weather radars are discussed.

While it is unclear what the design of NexPAR will entail, it is assumed that a NEXRAD replacement system will be a PAR, rather than a parabolic dish. The assumption of a PAR architecture is made because of the many advantages of PAR, including (but not limited to) significant scan flexibility, graceful degradation (i.e., fewer single-point-of-failure components), and lower maintenance and operations costs. The NEXRAD system uses a parabolic dish, which mechanically rotates in azimuth and can tilt in elevation to provide a full volume of data every $\sim$5 min ('precipitation modes') to $\sim$10 min ('clear air modes'). The NEXRAD data has 250 m range resolution and 1° azimuthal resolution, and data are collected at successive elevation angles as prescribed by a pre-defined volume coverage pattern (VCP). NEXRAD can collect both single-polarization data (e.g., radar reflectivity factor, radial velocity, spectrum width) and polarimetric data (e.g., differential reflectivity, copolar correlation coefficient, and differential phase information).

The first iteration of a system that was proposed to replace NEXRAD was the Multifunction Phased Array Radar (MPAR; Weber et al. 2007; Reinoso-Rondinel et al. 2010; Zrnić et al. 2015; Weber et al. 2017). The idea of the MPAR system was to share design and operating costs between several partners; namely, the Department of Defense (DoD), the Federal Aviation Administration (FAA), and the National Oceanic and Atmospheric Administration (NOAA). Under the MPAR

paradigm, the radar needs of all these agencies would be met with a single national radar network, where each radar devotes a portion of the scan timeline to meteorological scanning, and the remainder to aviation and defense needs.

Much of the MPAR concept was rolled into a new concept called SENSR in 2016/2017. SENSR, or Spectrum Efficient National Surveillance Radar, is a planned national radar network similar in concept to MPAR. The goal of the SENSR project was originally to consolidate weather, aviation, and defense radar into a single band in the electromagnetic spectrum, and selling the then-vacated spectrum to private industry to pay for the new radar system. One distinct difference between MPAR and SENSR is that SENSR does not have as stringent requirements on the system design. For example, a possible SENSR solution could be a 'system of systems', rather than a single nationwide system of radars. In September 2018, NOAA made the decision to remove the high-resolution weather requirements from the SENSR requirements (Federal Aviation Administration 2017; Weber et al. 2019). For phased array weather radar research, this change effectively ensured that the weather radar system to replace NEXRAD will be a 'weather-only' system, such that the sole focus will be meteorological observations.

Because the architecture of an MPAR or SENSR system would likely be a four-faced stationary PAR, the withdrawal of NOAA/NWS requirements from SENSR re-opened the discussion about the design of a NexPAR system. As discussed in Weber et al. (2019) and Weber and Herd (2019), several designs can satisfy the

preliminary goals of NOAA and/or NWS. A subset of possible NexPAR designs is shown in Fig. 1.2.

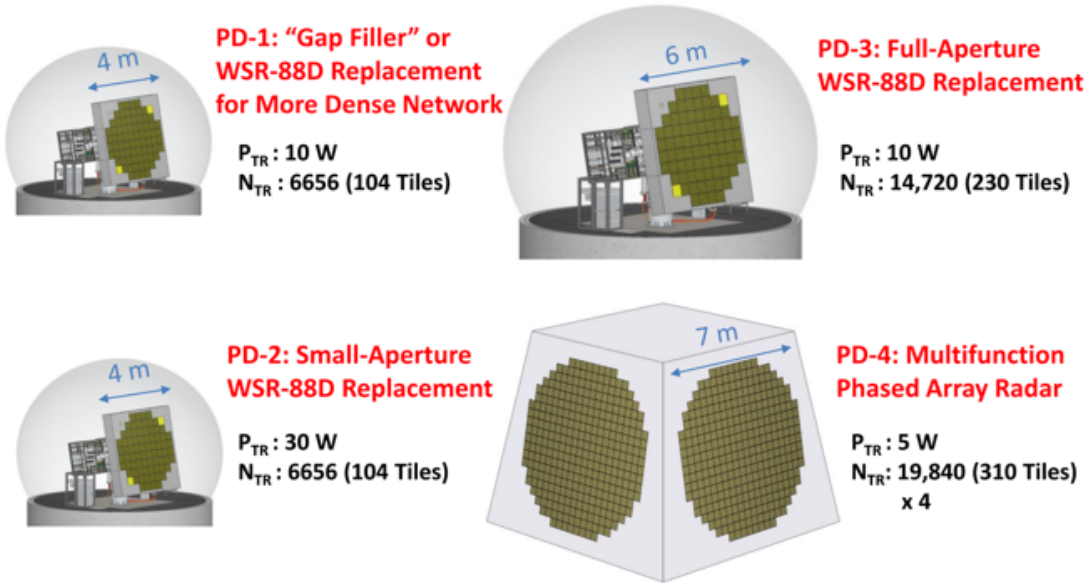

Figure 1.2: A subset of possible designs for the NexPAR network. PD-1 and PD-2 represent a more dense network of smaller radars, similar in concept to the CASA system (McLaughlin et al. 2005). PD-3 closely resembles NEXRAD and the WSR-88D radars, and would essentially replace the parabolic dishes in NEXRAD with a planar PAR. PD-4 is a four-faced PAR, where each face covers a 90° sector. Figure from Weber et al. (2019).

Another design solution that is not shown in Fig. 1.2 is a cylindrical PAR. A cylindrical PAR has a distinct advantage in its polarimetric capability, in that the transmit beam does not need to be steered off of broadside; rather, the columns of radiating elements are commutated sequentially around the array. This feature

ensures that there is no induced cross-polar radiation due to beamsteering off of broadside. The difficulty in achieving sufficient cross-polar isolation is a significant challenge for planar PAR (hereinafter PPAR), and this challenge has been a significant hurdle in the design of a four-faced PPAR (i.e., PD-4 in Fig. 1.2). In support of the cylindrical PAR design, a prototype has been built at the University of Oklahoma. This radar, called the Cylindrical Polarimetric Phased Array Radar (CPPAR; Zhang et al. 2011; Karimkashi and Zhang 2015; Fulton et al. 2017), has been used as a proof of concept for the cylindrical PAR design. Further testing is still ongoing to assess whether or not such a design could be feasible for a full-scale radar network.

1.2.3 Signal Processing Techniques and Scanning Strategies

In addition to the research ongoing to determine the design and architecture of a NexPAR system, there has been significant effort ongoing into examining the ability of PAR to improve data quality and/or achieve faster scans by using relatively novel signal processing techniques and scanning strategies. The techniques described in this section are the following:

- Beam multiplexing (BMX; Yu et al. 2007), where successive transmit pulse pairs are steered in different directions before returning to the original transmit direction in order to allow for more decorrelation of the received signals, increasing the number of independent samples per unit scan time; drawbacks

include a lack of support for ground-clutter filtering and staggered pulse repetition time (staggered PRT) processing;

- Radar imaging & digital beamforming (e.g., Isom et al. 2013), where the transmit beam is spoiled in azimuth and/or elevation in order to cover a larger area simultaneously at the expense of higher two-way sidelobes, lowered sensitivity, and a broader mainlobe, while digital beamforming (DBF) is used on receive to electronically form narrow, individual receive beams;

- Adaptive scanning (e.g., Reinoso-Rondinel et al. 2010; Heinselman and Torres 2011), where the beam is electronically steered toward areas of interest and away from areas not of interest to the user;

- Multiple-beam technique (MBT; Zrnić et al. 2015; Melnikov et al. 2015), where N beams ($N > 1$) are transmitted in N directions in rapid succession, using digital beamforming on receive.

The first technique described here is beam multiplexing (BMX). By transmitting successive pulse pairs in different directions, the radar returns between successive pulse pairs is assumed to be fully decorrelated, such that the pulse pairs are entirely independent. This increases the number of independent pulse pairs for a given dwell time, thereby improving data quality. The BMX method was detailed by Zrnić (1977), and validation of this method by using the NWRT is given by Yu et al. (2007). As expected, Yu et al. (2007) found that BMX does offer improved data

quality for a given dwell time. Furthermore, Yu et al. (2007) estimated that BMX affords a speedup factor of 2–4. In other words, the scan can be sped up by a factor of 2–4 without a reduction in data quality. However, there are certain limitations of BMX, including a lack of support for staggered PRT modes and an inability to perform ground clutter suppression (Siggia and Passarelli Jr. 2004). The impact of BMX over a larger area than that tested in Yu et al. (2007) is detailed in Chapter 2, and a more thorough mathematical treatment of BMX can be found in Section 2.2.2 and Appendix A.

Radar imaging and DBF is a method whereby the transmit beam is spoiled. In a non-imaging scan mode, the beamwidth is largely dictated by the size of the array aperture, roughly following

$$\theta(rad) = 1.27\frac{\lambda}{D} \tag{1.1}$$

where θ is the beamwidth of the radar in radians, λ is the wavelength of the radar, and D is the diameter of the aperture (Doviak and Zrnić 1993). Note that the aperture does not have to be square (e.g., ASR-9 radars), such that the beamwidth may be different in the azimuthal and elevation dimensions; in such a case, the elevation beamwidth is related to the height of the aperture, and the azimuthal beamwidth is related to the width of the aperture.

Radar imaging involves changing the amplitude and phase at each transmit element of the PAR, such that the transmit beam is wider than that dictated by the aperture size. The goal of radar imaging is to cover a larger area in a given time (e.g.,

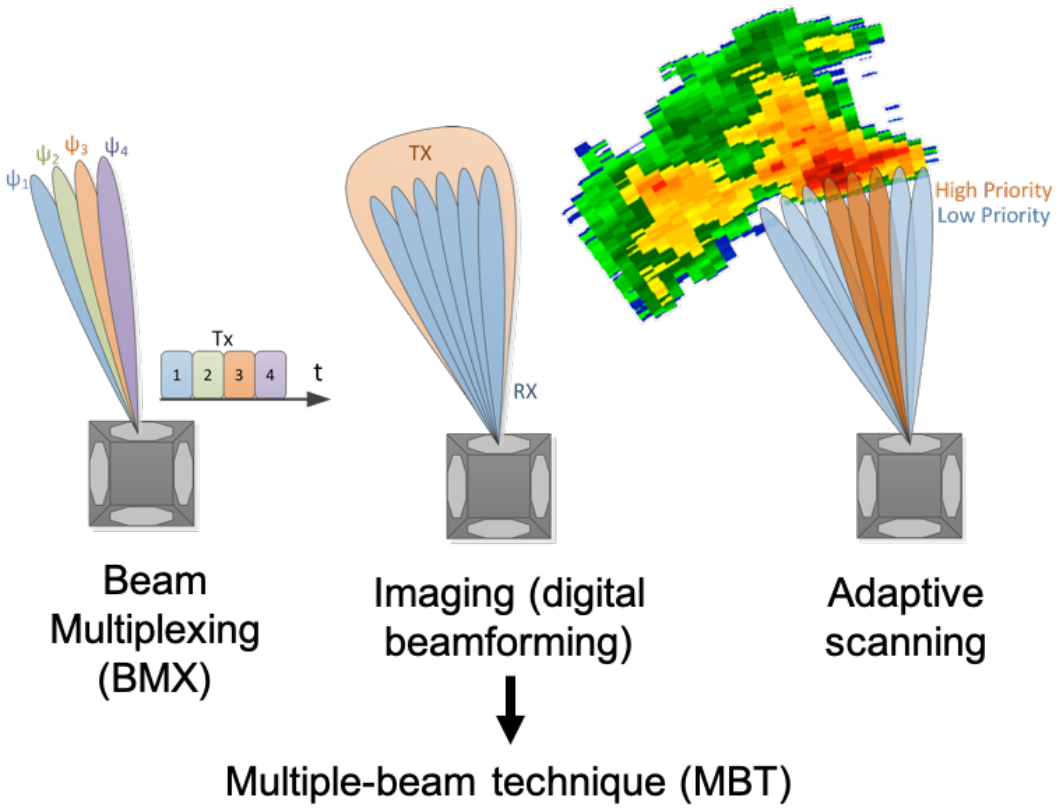

Figure 1.3: Various scan modes available with PARs: beam multiplexing, radar imaging and digital beamforming, adaptive scanning, and the multiple-beam technique.

Isom et al. 2013; Weber et al. 2017). This has several advantages, including overall scan speedup and improved data quality (as long as the higher two-way sidelobes do not create a bias in the data). Additionally, the data within a single transmit beam is collected simultaneously, such that advection does not need to be taken into account, especially between successive elevations if spoiling in elevation (e.g., Mahre et al. 2017). The Atmospheric Imaging Radar (AIR; Isom et al. 2013) is an

example of a system that uses radar imaging and DBF to collect rapid-scan weather radar data. Analysis of data collected by the AIR has yielded some insightful results about rapidly evolving changes in tornado and mesocyclone structure (Kurdzo et al. 2017; Mahre et al. 2018; Griffin et al. 2019; Pittman et al. 2020). Radar imaging has its own disadvantages, such as relatively high two-way sidelobes. This can cause an issue when there is a strong reflectivity gradient present in the same area and dimension in which the transmit beam is being spoiled. Additionally, the spoiled transmit beam has reduced sensitivity due to the lower incident power density at the scatterers. An assessment of using radar imaging in a radar simulator is included in Chapter 2.

The concept of adaptive scanning (and, more broadly, cognitive radar) has been applied rather extensively in defense and other non-meteorological applications (Capraro et al. 2006; Haykin 2006; Guerci 2010). Adaptive scanning in a PAR sense often involves using data from a 'surveillance scan' and an optimization framework to decide how to reallocate the resources of the radar. For example, a scan of the volume could be completed, and the radar can be electronically beam-steered toward areas of interest, and away from areas not of interest. NEXRAD has a mode called Automated Volume Scan Elevation Termination (AVSET; Chrisman 2009) that terminates all elevation angles above which there is minimal areas of high reflectivity.

However, the use of adaptive scanning and cognitive radar concepts have been relatively limited in weather radar, likely due to the fact that PARs are a relatively

new innovation for weather applications, and most cognitive radar techniques rely upon agile scanning capabilities of PAR. In recent years, machine learning, optimization, and other cognitive radar concepts have been used to redistribute radar resources toward a specific goal such as waveform design (Kurdzo et al. 2014, 2015b; Mitchell et al. 2018; Kurdzo et al. 2019), improved target tracking (Romero and Goodman 2013; Bell et al. 2019), or for the improvement of temporal resolution (Chrisman 2009; Reinoso-Rondinel et al. 2010; Heinselman and Torres 2011). For weather radars, Reinoso-Rondinel et al. (2010) showed that the scheduling system for a multifunction PAR can be altered to revisit regions of interest more frequently by scanning adaptively, and Heinselman and Torres (2011) showed that adaptive scanning can be used to achieve faster updates of severe local storms. Both of these studies have achieved promising results, but they do not rely on mathematical optimization to achieve the goal of rapid updates. It is believed that mathematical optimization (especially multi-objective optimization, or MOO) can lead to improved results in cognitive and fully adaptive radar systems, such as in Mitchell et al. (2018).

Finally, the Multiple-Beam Technique, or Multibeam Technique (MBT; Zrnić et al. 2015; Melnikov et al. 2015) is another scanning strategy that offers promise of improving data quality and/or volumetric update time. MBT is somewhat similar to radar imaging and DBF, except than in MBT, N narrow ('pencil') beams are transmitted sequentially in rapid succession–rather than one wide simultaneous

beam–and the pointing direction for each beam is chosen such that there is minimal sidelobe overlap between the N transmitted beams. As in radar imaging, DBF is performed on receive to electronically form narrow receive beams. Unlike radar imaging, the incident power density is not necessarily reduced at the scatterers, because the radar beam is still focused, rather than being spoiled in azimuth or elevation. However, duty cycle limitations still apply, such that additional accommodations need to be made, such as a reduction in power for each individual beam or a longer PRT. Because MBT should theoretically produce similar results to radar imaging (except with improved sidelobes and likely improved sensitivity), MBT is not explicitly simulated in this research.

1.3 Goals

The goals of this study are threefold: first, the impact of scanning strategy selection on simulated phased-array weather radar data quality is assessed in Chapter 2. To achieve this goal, a radar simulator with NWP data is used, and the expected root mean square error (RMSE) of moment data is calculated for multiple scan strategies. This research is undertaken in order to assess which scanning strategies and signal processing techniques can best achieve desired data quality in a rapid-scan PAR system. A paper based on this research is currently in peer review (Mahre et al. 2020).

Second, the benefits of a rapid-scan weather radar are quantified, as related to tornado detection latency time (Chapter 3). This is done to assess the direct impact of volumetric update time on a proxy for tornado warning lead time. The results from Chapter 3 also show that the tornadic debris signature (TDS) forms and evolves extremely rapidly, on timescales of less than 1 min, which is a novel result.

Finally, the ability to adaptively scan with a phased-array weather radar is assessed, with the goal in mind of improving expected data quality for radial velocity and radar reflectivity factor. This is achieved by mathematical optimization–somewhat similar in design to Mitchell et al. (2018). This research is largely described in Chapter 4. Finally, a summary of the conclusions of this paper and the implications of the results of this study are given in Chapter 5.

Chapter 2

Effect of Scanning Strategy Choice on PAR Data Quality

2.1 Introduction to Data Quality Assessment

2.1.1 Background and Previous Research

For the proposed NexPAR network for high-resolution weather observations in the United States, a primary goal of NOAA/NWS is to improve temporal resolution ($\sim$1 min) with respect to the current $\sim$5 min update time offered by the current national network of Weather Surveillance Radar-1988 Doppler (WSR-88D) radars (Weber et al. 2019). While the deployment of WSR-88Ds that comprise NEXRAD and subsequent technology upgrades have improved warning performance and lead times (Polger et al. 1994; National Research Council 1995; Bieringer and Ray 1996; Simmons and Sutter 2005), many observations of weather phenomena require even faster update times. The primary reason why rapid-scanning radar is necessary in meteorology is that many weather phenomena evolve on the order of tens of seconds or less, rather than on the order of several minutes (e.g., Carbone et al. 1985; Wolfson and Meuse 1993; French et al. 2013; Wurman and Kosiba 2013; French et al. 2014;

Houser et al. 2015; Wakimoto et al. 2015; Kurdzo et al. 2017; Mahre et al. 2017, 2018; Bluestein et al. 2019; Griffin et al. 2019). For forecasting and operational purposes, Heinselman et al. (2012) and Wilson et al. (2017) have shown that the introduction of rapid scans with a phased array radar (PAR) leads to increased warning lead time, improved forecaster confidence, a higher probability of detection, and a lower false alarm ratio for tornadoes in a simulated operational setting. Additionally, data assimilation studies have shown the benefit of assimilating rapid-scan weather radar data to improve short-term numerical weather prediction (NWP) model accuracy (Yussouf and Stensrud 2010; Sun et al. 2014; Supinie et al. 2017). In practice, however, consideration must be given to the fact that improvements in update time often come at the expense of degraded data quality or reduced total coverage volume (Heinselman and Torres 2011). An attempt to scan faster simply by decreasing dwell time per radial (i.e., rotating the radar dish faster in a non-phased array system) will result in deleterious effects on data quality, if all other scan parameters are held constant. In this chapter, 'data quality' is used to refer to expected errors from statistical fluctuations in radar variables, rather than other aspects of data quality such as biases.

One major factor that significantly impacts data quality is the radar design and architecture. While it is likely that a NEXRAD replacement network will utilize phased array technology, the aperture size, transmit power, and scanning mode (mechanical or electronic) are still undetermined (Weber et al. 2019). Additionally, the desired missions of the radar system (i.e., multifunction or weather-only) will

determine the scan timeline percentage that can be devoted to weather observations. Because of these system and network uncertainties, this study intends to investigate a representative subset of the possible radar architectures of the final system (e.g., PD-3 and PD-4 in Weber and Herd 2019, which are notional 6-7 m diameter high-resolution weather radars that are possible designs for a NexPAR system) using simulations, rather than attempting to account for all possible design architectures. Additionally, this study only analyzes data quality impact on horizontal reflectivity factor (Z_H) and radial velocity (v_r), as they are important non-polarimetric radar variables for operational forecasters. Polarimetric variables are not considered in this study, because polarimetric biases and considerations from radar architecture and system design are believed to play a larger role in overall polarimetric data quality than statistical fluctuations. However, we propose studying polarimetric statistical fluctuations as a possible future route of research. The conclusions herein are intended to provide a general framework for a discussion of the advantages and disadvantages of various scan techniques and radar design architectures.

It has been previously documented that speeding up a scan simply by reducing the number of samples per radial will inevitably lead to poorer data quality (Doviak and Zrnić 1993; Yu et al. 2007; Reinoso-Rondinel et al. 2010). This presents an obvious challenge when considering that an overall scan speedup of 1.25–5x is desired for NexPAR compared to NEXRAD, in order to achieve the NexPAR goal of 1-min volumetric updates (Weber et al. 2017, 2019). Thus, to achieve acceptable data

quality, other scan methods will need to be employed. A description of the scan methods tested in this chapter is given in section 1.2.3.

The purpose of this chapter is to quantify the effects of various scanning strategies on radar data quality by using RSim (described in section 2.2.1), a flexible dual-polarization radar emulator. This study is novel in that it quantifies and compares data quality from multiple scanning strategies and data collection methods for a large area, allowing for a direct comparison of data quality between scanning strategies. This is only achievable with a large-scale radar simulator (rather than an actual radar system) because the same simulated thunderstorm is used for each case, enabling direct comparisons. For this study, a supercell in the 31 May 2013 Central Oklahoma environment is used (Wurman et al. 2014; Wakimoto et al. 2015, 2016; Tanamachi and Heinselman 2016; Bluestein et al. 2018, 2019). This case was chosen because data quality is especially important for high-impact events where significant life and property are lost, and accurate forecasts are imperative.

Using a large-scale radar simulator like RSim with realistic weather inputs for data quality assessment is novel, and this method offers multiple advantages over other methods. First, it allows for assessment of data quality for a realistic case, offering insight into the full distribution of data quality over a large area and accounting for the spatial distribution of spectrum width and signal-to-noise ratio (SNR) and any dependence between these two variables. Second, RSim uses model data with an update time of 1 min; this offers advantages compared to simulators that use data with coarser temporal resolution as their basis. The reason why using

rapidly updating model data is advantageous is that the update time of the microphysical and velocity fields is on the order of the full volumetric update time for the envisioned NexPAR system. As such, no assumptions need to be made about vertical advection or temporal/spatial interpolation between scans.

The results from this study expand upon previous studies such as Yu et al. (2007) and Weber et al. (2017). For example, the achievable scan speedup factor with BMX is calculated using simulated radar data quality over a large area and at multiple times and several elevation angles, as opposed to calculating data quality over a small area or along one radial (e.g., Fig. 5 and Fig. 7 of Yu et al. (2007)). This should yield a more accurate estimate of speedup factor for a NexPAR-style system. Additionally, this paper focuses on the entire histogram of data quality estimates, rather than simply calculating the number of pixels which have 'unacceptable' data quality estimates, such as in Weber et al. (2017). Finally, the effect of beam spoiling on mesocyclone intensity calculation capability is shown for the first time. While it has previously been shown that changing the effective beamwidth of the radar by altering the azimuthal sampling can affect tornado detection capability (e.g., Brown et al. 2002), this is the first study to research the effect of changing the radar transmit pattern on measured rotation intensity.

Many of the scan speedup techniques tested in this study are only easily achievable with a fully flexible, all-digital phased array radar architecture (e.g., Palmer et al. 2019). The conclusions on error estimation and data quality can help determine which scanning strategies are viable for achieving full-volume updates on the

order of 1 min without sacrificing data quality. The results herein should be applicable to a wide range of NexPAR designs (e.g., four-faced stationary PAR, one-faced mechanically rotating PAR, etc.).

In this study, data quality is estimated from a simulated rapid-scan weather radar by comparing expected RMSE of radar variables. Data quality is then compared between multiple scan scenarios, where various methods are employed to achieve faster PPI scans. Comparisons of data quality include 1) altering the number of pulses per radial, 2) BMX and non-BMX data collection modes, and 3) varying levels of transmit beam spoiling with DBF on receive (i.e., imaging).

2.2 Methods

2.2.1 Radar Simulator (RSim)

For the analysis conducted herein, a radar simulator is used. Simulators can reveal important information regarding the expected fields from a number of controlled input scenarios, and can allow for direct comparison of data quality between scan methods because of the ability to re-analyze the same simulated weather event with different scanning strategies. This chapter utilizes output from a large-domain radar simulator–RSim–in order to assess and quantify the data quality of a rapid-scan weather radar system. Here, we assume that the radar being tested is a single-faced, mechanically rotating PAR.

RSim uses WRF model data (Skamarock et al. 2008) as an input, and computes moment data in the radar domain based on the number concentration and radial velocity of each hydrometeor type at each model grid point. RSim uses T-matrix scattering for four hydrometeor types: rain, graupel, snow, and ice. The T-matrix method relates scattering amplitudes to the particle size distribution (PSD) for each hydrometeor type (Mishchenko et al. 1996; Mishchenko 2000). More information about the T-matrix scattering method and polarimetric variable estimation can be found in Zhang et al. (2001) and Jung et al. (2008). The radar emulations derived through RSim account for angular and range weighting functions, by weighting the microphysical contributions at each model grid point based on the range and antenna weighting patterns. Each model grid point in RSim is weighted and summed to derive the expected moments at each azimuth, elevation, and range combination in the radar scan domain. Range weighting patterns and antenna beam patterns (proportional to sinc^2r and $\text{sinc}^2\theta\text{sinc}^2\phi$, respectively) used in this study are based on established patterns in Doviak and Zrnić (1993) and Orfanidis (2016), where r is the range, θ is the azimuth angle, and ϕ is the elevation angle. RSim provides significant scanning flexibility, in that radar imaging can be simulated using spoiled beams on transmit and pencil beams on receive; non-sequential beam positions can also be simulated.

For this study, the model parameterizations used for WRF are identical to those used in Bodine and Rasmussen (2017); the parameterizations are listed in Table 2.1. Two-way nesting is used between the grids, and 0.25° GFS data is used to initialize

Table 2.1: A list of the WRF model parameterizations used in this study.

Parameterization Type	**Parameterization Name**
Microphysics scheme	Morrison
Land surface scheme	Noah (Chen and Dudhia 2001)
Cumulus parameterization	Kain-Fritsch (at 27-km and 9-km grids)
PBL scheme	Yonsai University (YSU; Hong et al. 2006)
Longwave radiation scheme	RRTM (Mlawer et al. 1997)
Shortwave radiation scheme	Dudhia (Dudhia 1989)

the simulations. Additionally, 44 vertical grid points are used with maximum vertical resolution in the boundary layer. WRF was run at 1 km horizontal resolution and 1-min temporal resolution for a supercell in the 31 May 2013 Central OK environment, and larger 27-km, 9-km, and 3-km domains are used outside this innermost mesh to downscale from larger-scale conditions.

To estimate spectrum width, local thermodynamic data and radial velocity estimates are used. While the contribution of larger-scale shear on spectrum width can be estimated as the local standard deviation of velocity (σ_s; Doviak and Zrnić 1993), this does not capture smaller-scale turbulence, which has a significant contribution to the overall spectrum width of the resolution volume (Brewster and Zrnić 1986;

Doviak and Zrnić 1993; Nastrom and Eaton 1997; Zhang et al. 2009). The overall spectrum width can be estimated as

$$\sigma_v^2 = \sigma_s^2 + \sigma_t^2 \tag{2.1}$$

where σ_v is the spectrum width observed by the radar and σ_t is the turbulence contribution. Other contributions to spectrum width, such as antenna motion, hydrometeor vibrations, and differential hydrometeor fall speeds are ignored. With the shear contribution being estimated by the local spatial standard deviation of velocity (Doviak and Zrnić 1993), the turbulence contribution can be estimated by using a rearranged version of Equation (2) from Nastrom and Eaton (1997):

$$\sigma_t^2 = \frac{\epsilon A^{3/2}}{f_{BV}} \tag{2.2}$$

where ϵ is the turbulent eddy dissipation rate, $A = 1.6$ is the Kolmogorov constant, and f_{BV} is the Brunt-Väisälä frequency, where $f_{BV} = \sqrt{\frac{g}{\theta}\frac{d\theta}{dz}}$, g is gravitational acceleration, and θ is potential temperature. The turbulent eddy dissipation rate used in this study is 0.02 m^2 s^{-3}; this is lower than in most literature sources (0.06 or 0.10 m^2 s^{-3} in Frisch and Strauch (1976) and Doviak and Zrnić (1993), respectively). However, the value of 0.02 m^2 s^{-3} is used in this study to produce spectrum width values that are consistent with NEXRAD observations (Fang et al. 2004). Brunt-Väisälä frequency is estimated using thermodynamic data from each grid point in the WRF domain.

2.2.2 Data Quality

For the purposes of this study, data quality is defined as the expected RMSE of radar variables in question. For signal power and radial velocity estimates with non-BMX data collection mode (also called contiguous pulse sampling, or CPS) and a pulse-pair processor, the variance of the velocity estimator is given by Zrnić (1977), Doviak and Zrnić (1993), and Yu et al. (2007):

$$\frac{\mathrm{var}(\hat{S}_C)}{S^2} = \frac{1}{M+1}\left[\sum_{l=-M}^{M}\frac{M-|l|+1}{M+1}\rho^2(lT_s) + \frac{N^2}{S^2} + 2\frac{N}{S}\right] \tag{2.3}$$

$$\begin{aligned}\mathrm{var}(\hat{v}_C) = \frac{\lambda^2}{32\pi^2 M\rho^2(T_s)T_s^2}\Bigg[(1-\rho^2(T_s))\sum_{l=-(M-1)}^{M-1}\frac{M-|l|}{M}\rho^2(lT_s) \\ + \frac{N^2}{S^2} + 2\frac{N}{S}\left[1-\frac{M-1}{M}\rho(2T_s)\right]\Bigg]\end{aligned} \tag{2.4}$$

where λ is the radar wavelength, M is the number of pulse pairs (equal to the number of pulses minus one for contiguous pulse pairs), T_s is the pulse repetition time (PRT), ρ is the normalized autocorrelation function, S is the signal power, N is the noise power, and $\hat{S}$ and $\hat{v}$ are the estimators for signal power and radial velocity, respectively. The signal power S (and by extension signal-to-noise ratio, or SNR) is derived from the Z_H calculated from the forward operator. The correlation between samples as a function of time, $\rho(T)$, is given by Doviak and Zrnić (1993):

$$\rho(mT_s) = \exp[-8(\pi\sigma_v mT_s/\lambda)^2], \text{where } m = 0, 1, 2, ...(M-1) \tag{2.5}$$

where σ_v is the spectrum width, and m is equal to 1 for CPS mode. For BMX applications (also called independent pulse sampling, or IPS), in which pulse pairs are

independent rather than contiguous, the variance of the velocity estimator reduces to the following equation from Yu et al. (2007):

$$\frac{\mathrm{var}(\hat{S}_I)}{S^2} = \frac{1}{2L}\left[1 + \rho^2(T_s) + \frac{N^2}{S^2} + 2\frac{N}{S}\right] \tag{2.6}$$

$$\mathrm{var}(\hat{v}_I) = \frac{\lambda^2}{32\pi^2 L\rho^2(T_s)T_s^2}\left[1 - \rho^2(T_s) + \frac{N^2}{S^2} + 2\frac{N}{S}\right] \tag{2.7}$$

where L is the number of pulse pairs, equal to the number of total pulses divided by two in BMX data collection mode. To obtain the standard deviation of reflectivity factor, the following equation is used:

$$\mathrm{SD}(\hat{Z}_H) = 10\ \log_{10}(1 + \frac{\mathrm{SD}(\hat{S})}{S}) \tag{2.8}$$

where $\mathrm{SD}(\hat{Z}_H)$ is the standard deviation of horizontal reflectivity factor. For this study, RMSE is calculated as follows:

$$\mathrm{RMSE}(\hat{X}) = \sqrt{\mathrm{SD}(\hat{X})^2 + (\hat{X} - X_{ref})^2} \tag{2.9}$$

where $\hat{X}$ is the estimated radar variable, and X_{ref} is the value of X in the reference field, such that RMSE is equal to the square root of the statistical fluctuation squared plus the bias (relative to the reference field) squared. Note that this definition of bias is not the statistical definition of a biased estimator, but rather is intended to compare the difference between a 'baseline' scan truth value and the 'new' truth value. For all scanning strategies except for radar imaging, the bias values are assumed to be zero, such that the RMSE is equal to the standard deviation(s) calculated in (2.3)-(2.8).

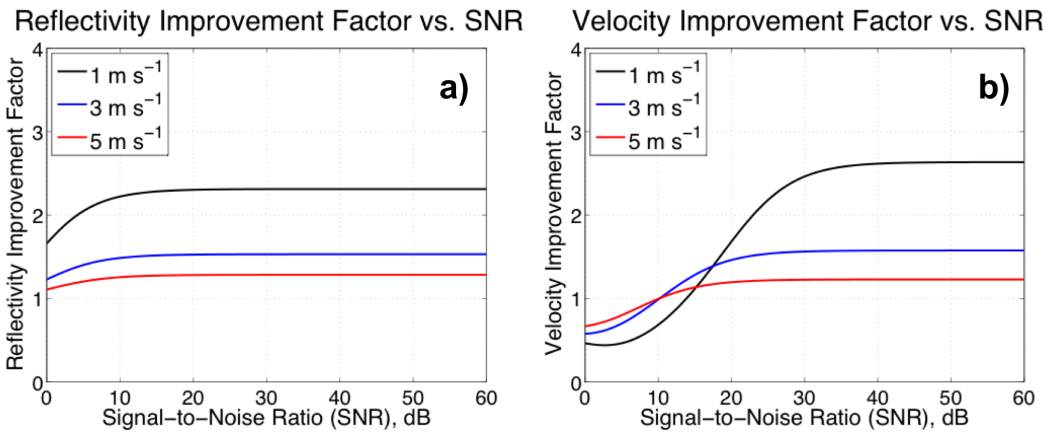

Figure 2.1: Improvement factor for Z_H (panel a) and v_r (panel b) as a function of SNR using BMX. The 3 lines represent spectrum width of 1 m s^{-1} (black line), 3 m s^{-1} (blue line), and 5 m s^{-1} (red line).

In practical weather applications, moment variance depends on 1) the number of pulses or pulse pairs, 2) spectrum width, and 3) SNR, defined as $\frac{S}{N}$. Additionally, data collection mode (BMX versus non-BMX) affects moment variance by changing the equation(s) used. The number of pulses per radial and data collection mode are the variables over which the radar operator has control, through VCP and scanning strategy design. In BMX, the number of pulse pairs for velocity estimation is reduced by a factor of $\frac{M}{L} = \frac{P-1}{\frac{P}{2}} = (2 - \frac{2}{P})$ compared to CPS, where P is the number of pulses along each radial. Thus, it is possible for velocity estimates to worsen, especially in areas of high spectrum width and/or low SNR (e.g., Fig. 4b in Yu et al. (2007)) due to the decrease in the number of pulse pairs. Fig. 2.1 shows a plot of both reflectivity and velocity improvement factor as a function of SNR for three values of spectrum width, where reflectivity (velocity) improvement factor

Table 2.2: A summary of the SENSR PPR for reflectivity factor, radial velocity, and spectrum width maximum standard deviation for a specified SNR and true spectrum width (σ_v).

	SNR	σ_v	Standard Deviation Requirement
Z_H	> 10 dB	4 m s^{-1}	< 1 dBZ
v_r	> 8 dB	4 m s^{-1}	< 1 m s^{-1}
σ_v	> 10 dB	4 m s^{-1}	< 1 m s^{-1}

is defined as the ratio between expected statistical standard deviation of Z_H (v_r) using CPS ((2.3)–(2.4)) divided by the statistical standard deviation of Z_H (v_r) using BMX/IPS ((2.6)–(2.7)). At low SNR, generally less than 10-15 dB, improvement factor is less than 1 for v_r, indicating that CPS yields better velocity estimates compared to BMX/IPS. Also, the improvement factor reaches a different asymptote at high SNR for each spectrum width value. For the high spectrum width case, the improvement factor at high SNR for Z_H (v_r) generally does not exceed 1.28 (1.23). Thus, the improvement in data quality by using BMX is very limited for high spectrum width. However, it should be noted that under no circumstances is RMSE for Z_H or differential reflectivity factor (Z_{DR}) negatively affected by using BMX instead of CPS.

For the data quality requirements used in this study, the preliminary program requirements (PPR) for the SENSR program are used (Federal Aviation Administration 2017), which are similar to current NEXRAD data requirements. A summary of the data quality requirements in the PPR is given in Table 2.2. For this study, the 1 m s^{-1} velocity RMSE requirement and the 1 dBZ reflectivity RMSE requirement are used for expected data quality in a rapid-scan system, although the final NexPAR design may alter the data quality requirements listed in Table 2.2. This study will focus on the effect of scanning strategies on the expected RMSE of the Z_H and v_r estimators.

2.3 Results

2.3.1 Data Quality and Error Estimation

In this section, RSim is used to examine expected RMSE of radar variables in a supercell case. Errors for different scan modes are examined based on estimates of data quality from (2.3)–(2.8). This analysis is performed on moment data output from RSim and is conducted for 15 PPIs: 0124, 0126, 0128, 0130, and 0132 UTC at 0.5°, 4.0°, and 8.0° in elevation. All results from this section use a WRF supercell case from 31 May 2013 in Central Oklahoma; PPIs of relevant radar variables at 0124 UTC are shown in Fig. 2.2. The selected times and heights were chosen to capture multiple times where the tornado was near its strongest intensity, and the heights were chosen to sample the low-, mid-, and upper-levels of the storm (near

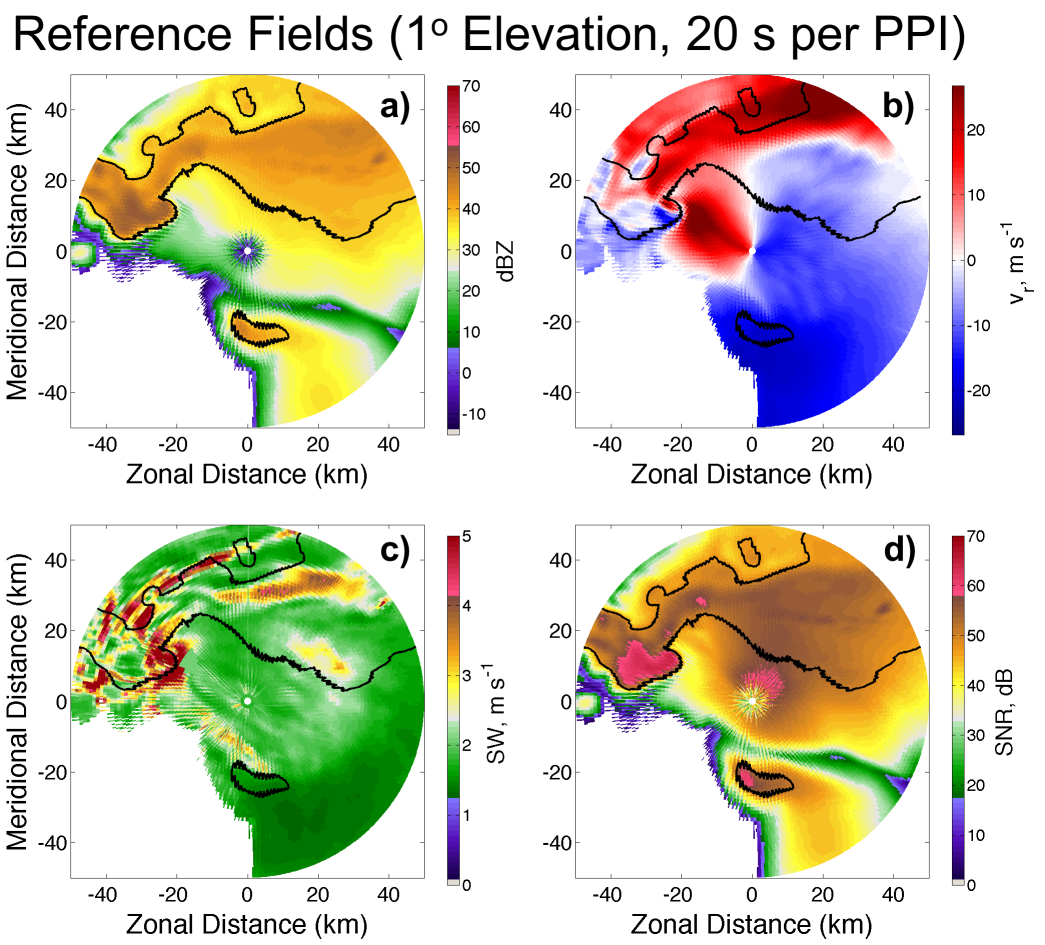

Figure 2.2: PPIs showing a) horizontal reflectivity factor (Z_H, in dBZ), b) radial velocity (in m s^{-1}), c) estimated spectrum width (in m s^{-1}), and d) signal-to-noise ratio (SNR, in dB). All PPIs are shown at 0124:00 UTC. Mean spectrum width is 2.48 m s^{-1}. The black contour corresponds to the region where Z_H is greater than 38 dBZ.

250 m, 2 km, and 4 km AGL, respectively). The simulated radar has a beamwidth of 1°, oversampled to 0.5° in azimuth. The data shown are thresholded at 3 dB of SNR, and a range resolution of 1 km is assumed. While this range resolution is

Table 2.3: A list of RSim scan parameters used in this study.

Scan Parameter	**Value(s)**
Scan times	0124, 0126, 0128, 0130, 0132 UTC
Elevation angles	0.5°, 4.0°, and 8.0°
Radar wavelength	0.107 m
PRT	1 ms
Range resolution & sampling	1 km
Azimuthal sampling	0.5°
Noise floor	-7.5 dBZ at 50 km
SNR threshold	3 dB

coarser than NEXRAD, it should be noted that this range resolution is constant across all cases studied herein, such that comparisons should hold at any realistic range resolution. A list of relevant RSim scan parameters are shown in Table 2.3.

For an estimation of expected RMSE, several assumptions are made regarding the radar system. Representative parameters for a notional NexPAR system are used as inputs into RSim; for example, a radar wavelength of 0.107 m and a PRT of 1 ms are used, with a similar noise floor estimate (-7.5 dB at 50 km) to that of NEXRAD. Here, a relatively short (1 ms) PRT is used to simulate a 'velocity cut' in NEXRAD. Additionally, a desired azimuthal sampling of 0.5° is assumed. These values are used as input into (2.3)–(2.7), along with the PPIs of SNR and spectrum

width at a given time, to generate a PPI of signal power, reflectivity factor, and velocity error estimates in both BMX and non-BMX data collection modes. Holding these system parameters constant, it is then possible to alter the scanning strategy to assess the data quality impact on each radar variable of interest.

2.3.1.1 Radar Reflectivity Factor (Z_H)

First, this study will analyze the effect of scanning strategy choice on data quality for Z_H. Data quality is assessed by using (2.3), (2.6), and (2.8), where the scanning strategies used are described below. Different scanning strategies are used to assess the impact on data quality, and to calculate any possible scan speedup, where scan speedup is the ability to complete a scan more quickly while maintaining the same level of data quality. Fig. 2.3 shows the RMSE of $\hat{Z}_H$ under four scanning strategies, analyzed at one time (0124 UTC) and one elevation angle (0.5°). Panel a) is a NEXRAD-style 'reference' scan, to which the other data collection techniques are compared. This NEXRAD-style scan transmits a 'pencil beam' (1° x 1°), collects a full PPI in 20 s (similar to the low-level scan rate in VCP 215), and uses CPS data collection mode. The data collection strategy in panel b) is identical to the technique in panel a), except that the time to complete the PPI is decreased from 20 s to 10 s by reducing the number of samples per radial. Panel c) transmits a pencil beam with a scan time of 20 s, but uses BMX (IPS) data collection mode rather than CPS data collection mode. In panel d), imaging (10° in azimuth) is used with a scan time of 20 s; this has the effect of increasing the number of samples

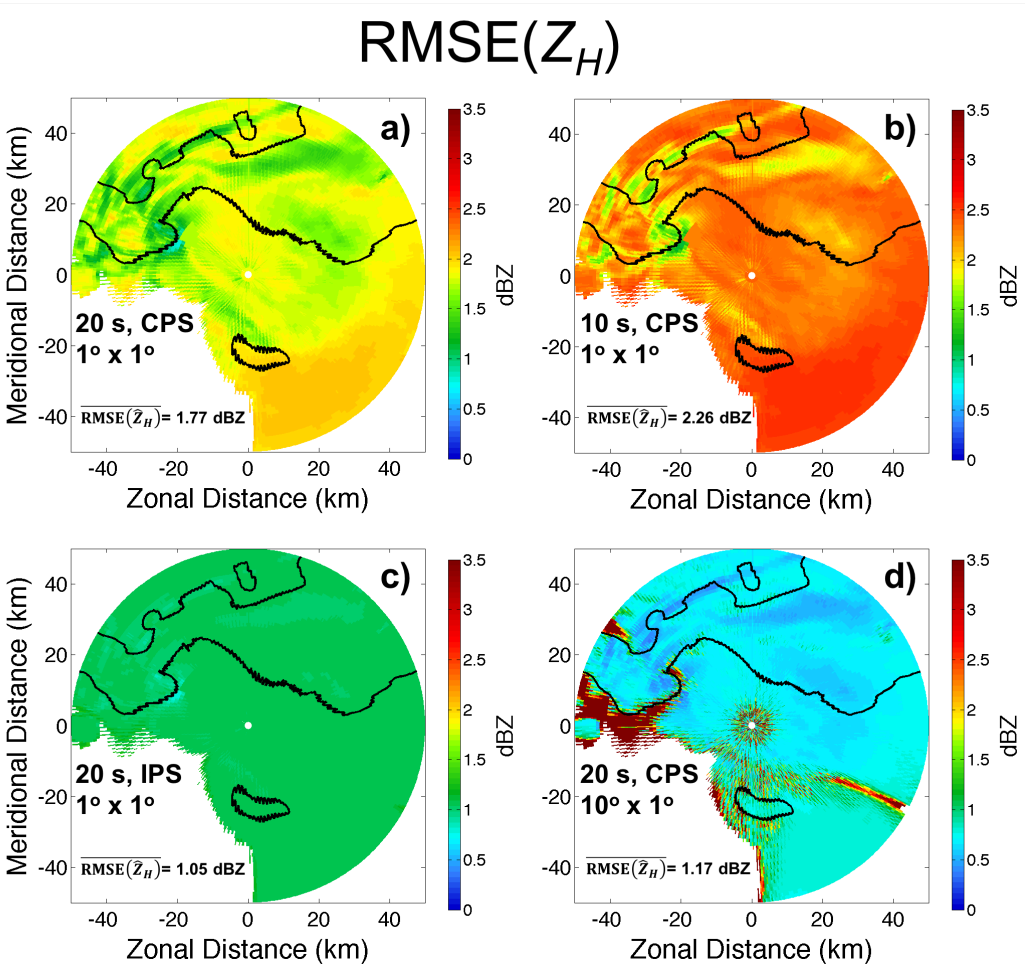

Figure 2.3: PPIs showing the calculated RMSE of Z_H for a) a pencil beam using CPS with a scan time of 20 s per PPI, b) a pencil beam using CPS with a scan time of 10 s per PPI, c) a pencil beam using BMX (IPS) with a scan time of 20 s per PPI, and d) a 10° fan beam using CPS with a scan time of 20 s per PPI. All PPIs are at 0124:00 UTC, at 0.5° in elevation. The RMSE listed in each panel is the mean RMSE for 15 realizations of each scan method; these values may deviate from the mean RMSE of the PPI shown by up to 0.01 dBZ.

per radial, at the expense of higher two-way antenna sidelobes in azimuth. Note that because the reference fields for panels a)-c) are identical, the RMSE plotted in Figs. 2.3 and 2.4 is simply equal to the statistical standard deviation.

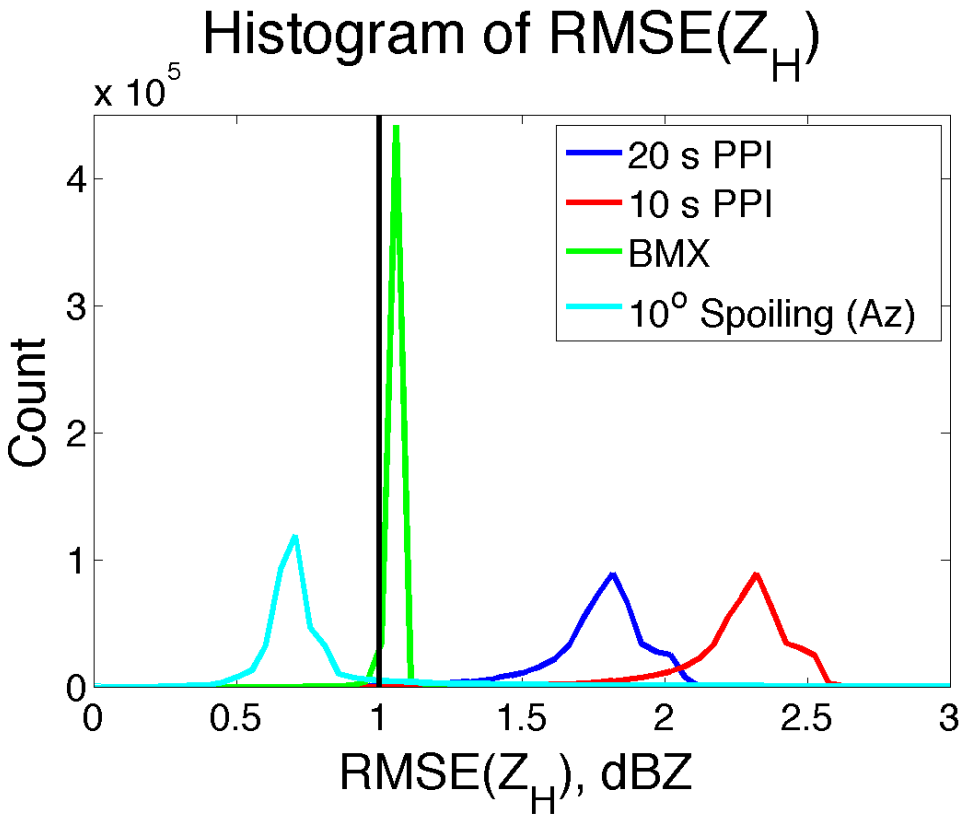

Figure 2.4: Histogram of mean Z_H RMSE estimates at 5 times and 3 elevation angles (0.5°, 4.0°, and 8.0°). The black vertical line represents the 1 dBZ suggested requirement (see Table 2.2).

To achieve rapid scans for a weather radar system, the most straightforward method is to decrease the number of samples along each radial (assuming a constant PRT). This decreases the number of pulses available for moment estimation

(i.e., a decrease in M in (2.3) and (2.4), and a decrease in L in (2.6) and (2.7)). For a mechanically rotating radar system, this could correspond to an increased rotation rate of the antenna. For a stationary (electronically scanning) system, such a change could come as the result of changing from a weather-only radar system to a multifunction system. The change in data quality for a simulated supercell on 31 May 2013 is shown in panels a) and b) of Fig. 2.3, where PPIs of calculated RMSE are shown for $\hat{Z}_H$. As is shown in Fig. 2.3, data quality is degraded (i.e., RMSE increases) when the scan time decreases (panel b compared to panel a).

To examine these errors with a larger sample size of data, mean RMSE($\hat{Z}_H$) is computed for all four scan scenarios for five different times and three different heights ($\sim$500,000 points). The effect on data quality is evident in Fig. 2.4, as the red curve, representing the histogram of RMSE values from 10 s PPIs, is clearly shifted to the right of the dark blue curve, representing the distribution of RMSE values from 20 s PPIs in CPS mode. The mean RMSE($\hat{Z}_H$) values for the set of $\sim$500,000 points are 1.77 dBZ (2.26 dBZ) for PPIs lasting 20 s (10 s), corresponding to a 28% increase in RMSE when the number of samples is reduced by a factor of 2. This is expected, as var($\hat{Z}_H$) is roughly inversely proportional to the number of pulses in (2.3). This difference in data quality can be seen qualitatively in Fig. 2.5, when comparing panels a) and b), as Fig. 2.5b shows increased granularity and a 'coarser' appearance than Fig. 2.5a.

The next scan speedup method tested in this study is BMX. By qualitatively analyzing Fig. 2.3, there is clear spatial homogeneity in the PPI of RMSE($\hat{Z}_H$)

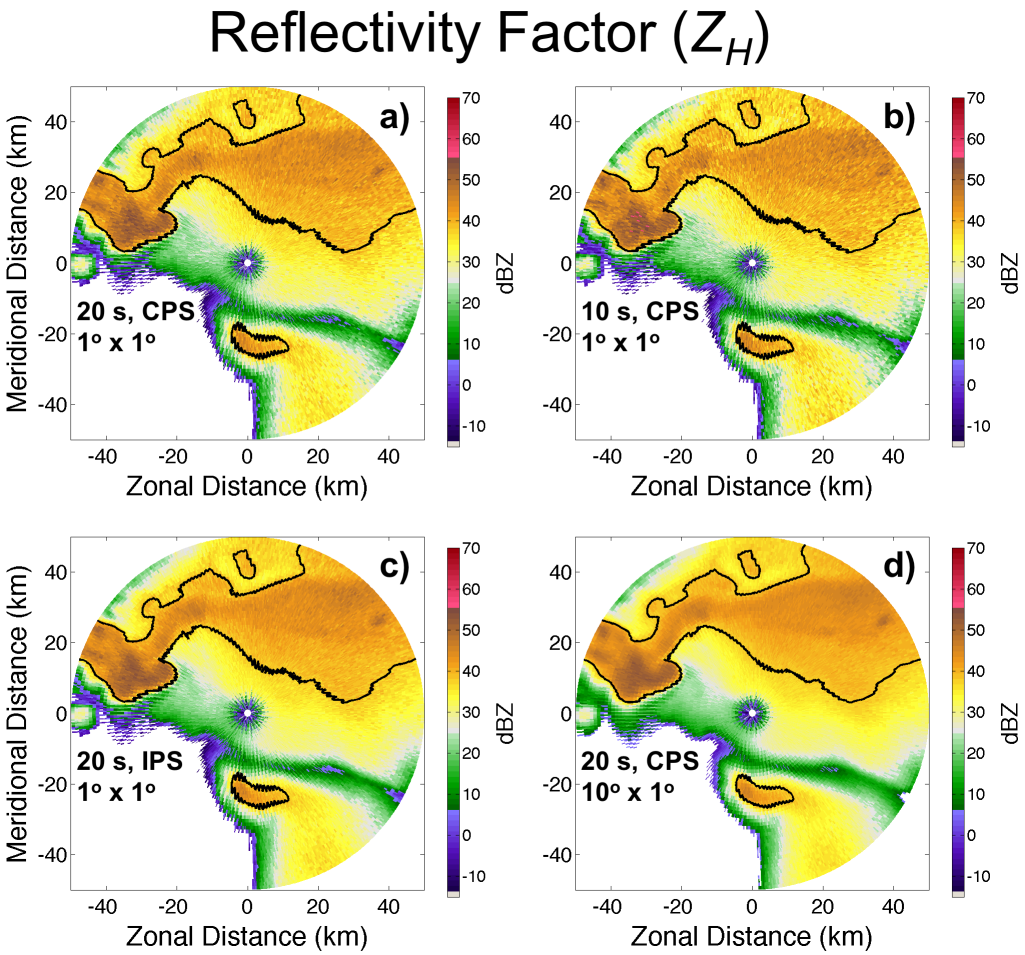

Figure 2.5: PPIs showing the reference Z_H fields with the expected standard deviation added as AWGN. Note that the underlying reference field is different in panel d), due to the lowered sensitivity and higher antenna sidelobes.

values, reflected in the distinct histogram shape of BMX RMSE($\hat{Z}_H$) data (green curve in Fig. 2.4). A mathematical explanation of this phenomenon can be derived

by expanding all terms in (2.3) and (2.6), and making use of (6.12) in Doviak and Zrnić (1993):

$$\frac{1}{M_I} = \sum_{l=-M}^{M} \frac{M - |l| + 1}{M + 1} \rho^2(lT_s) \tag{2.10}$$

where M_I is the total number of independent samples, and all other variables are as defined in (2.3). Then, (2.3) and (2.6) can then be separated into similar and dissimilar terms, and values plugged in for $\rho(T_S)$ show that the range of error estimates yielded by (2.3) is wider than error estimates yielded by (2.6), especially at high SNR. This explains the difference in histogram shape between the BMX error estimates (green curve in Fig. 2.4) and all other histograms plotted in Fig. 2.4; a more complete mathematical explanation of this phenomenon can be found in Appendix A. For the collection of ∼500,000 data points (example PPI in Fig. 2.3c), the mean RMSE($\hat{Z}_H$) is equal to 1.05 dBZ. This shows a significant improvement over the 1.77 dBZ mean RMSE($\hat{Z}_H$) value obtained for CPS (non-BMX) data collection in the 15 PPIs analyzed.

Because (2.6) is inversely proportional to the number of samples, it is concluded that the expected mean RMSE($\hat{Z}_H$) is 1.48 dBZ when the scan time is reduced from 20 s to 10 s per PPI. This number is calculated by multiplying the standard deviation of Z_H in BMX/IPS data collection mode by the square root of the difference in scan time ($\sqrt{2}$). Thus, it can be said that BMX can offer improved data quality, even in situations where the total scan time is decreased by a factor of 2. Working backwards, the inverse proportionality between variance and number of samples

can be leveraged to determine an 'equivalent speedup factor'. This corresponds to the factor by which the number of samples per radial can be reduced, while still maintaining the same data quality (as determined by mean RMSE($\hat{Z}_H$) of the NEXRAD-style scan). For a comparison between RMSE($\hat{Z}_H$) for CPS and BMX, the speedup factor is equal to the ratio of mean RMSE($\hat{Z}_H$) squared. For this comparison, the equivalent speedup factor is $\left(\frac{1.77}{1.05}\right)^2 = 2.84$. Thus, it can be said that when switching from CPS to BMX/IPS data collection mode, the scan time can be decreased by a factor of 2.84, while keeping data quality for Z_H constant.

Finally, radar imaging (10° azimuthal beam spoiling on transmit) is evaluated as a possible scan speedup method. Beam spoiling while keeping the scan time constant (i.e., 20 s per PPI) increases the number of samples per radial, while decreasing the SNR at each point because of the reduction in incident power density; this was simulated by decreasing antenna gain on transmit. This has the effect of generally improving data quality in areas where there is minimal reflectivity or radial velocity gradient in the direction of beam spoiling, because in this area, the increase in the number of pulse pairs improves data quality more than higher two-way sidelobes and lower SNR reduce data quality. This is seen in Fig. 2.3d, where many of the estimates of RMSE($\hat{Z}_H$) are shown to be significantly improved (cyan colors in Fig. 2.3d), compared to Fig. 2.3a-c. However, there is a significant reduction in data quality around the edges of the supercell, especially to the southwest of the hook echo, where a sharp horizontal gradient in Z_H is present. This results in very poor data quality (e.g., RMSE($\hat{Z}_H$)$>$ 15 dBZ), because the values derived with the

spoiled beam are biased with respect to the pencil beam due to higher sidelobes. This is represented by the dark red area on the western side of the PPI in Fig. 2.3d; the colorbar in Fig 2.3d is capped at 3 dBZ for consistency with the other panels in Fig. 2.3, but some of the values in panel d) exceed 15 dBZ. The histogram appears to show that beam spoiling performs better than BMX for improving data quality (Fig. 2.4), but the area of extremely high RMSE($\hat{Z}_H$) values (not shown in Fig. 2.4) creates a situation where the mean RMSE($\hat{Z}_H$) is 1.17 dBZ, which is higher than that of BMX (1.05 dBZ). This underscores the point that beam spoiling should be applied in an adaptive manner (e.g., Weber et al. 2017).

Based on mean RMSE($\hat{Z}_H$) alone, the speedup factor compared to a NEXRAD-type scan is 2.29 for beam spoiling to 10° in azimuth. However, many meteorologists may find the regions with extremely high RMSE (bias, in this case) to be unacceptable, despite the apparent 'improvement' in data quality when simply considering the mean RMSE over the whole domain. Additionally, the loss in sensitivity that is apparent in Fig. 2.5d is a consideration, especially when trying to detect weak radar echoes such as developing precipitation, light precipitation, and fine-line features such as cold fronts and gust fronts.

For radar imaging, it is clear that the method does a good job of improving the data quality in the heavier precipitation cores and away from large reflectivity/radial velocity gradients, but creates a situation where data quality may be extremely poor in regions near reflectivity and radial velocity gradients as a result of higher antenna sidelobes and where the loss of sensitivity reduces available data for forecasters.

Thus, it is likely that the 'best' method for utilizing beam spoiling is to adaptively spoil the beam, in order to avoid spoiling across areas of sharp reflectivity and/or radial velocity gradients.

2.3.1.2 Radial Velocity (v_r)

In addition to analyzing the data quality impact on Z_H, this study also analyzes the impact on v_r using the same approach and methods described in Chapter 2.3.1.1. Again, data quality is compared between four scan strategies: 20 s PPIs with a pencil beam on transmit in CPS mode, 10 s PPIs with a pencil beam on transmit in CPS mode, 20 s PPIs with a pencil beam on transmit in IPS (BMX) mode, and 20 s PPIs with a 10° azimuthally spoiled transmit beam in CPS mode.

The RMSE of $\hat{v}_r$ is calculated using (2.4), (2.7), and (2.9) for each scanning strategy; an example for one PPI per scan method is plotted in Fig. 2.6. Qualitatively, decreasing the scan time to 10 s (example in Fig. 2.6b) produces poorer data quality than for 20 s PPIs in CPS mode (Fig. 2.6a). For the collection of 15 PPIs, this corresponds to an increase in RMSE($\hat{v}_r$) from 0.76 m s^{-1} to 1.06 m s^{-1} (39% increase in RMSE; histogram shown in Fig. 2.7). The difference in data quality can be seen qualitatively in Fig. 2.8, where panel b) appears to be noisier than panel a). This phenomenon is most pronounced along and near the zero-isodop in the northeastern quadrant of the PPI.

By analyzing the distribution of the RMSE histogram in Fig. 2.7, it is also possible to compare the percentage of pixels that are of 'acceptable' data quality

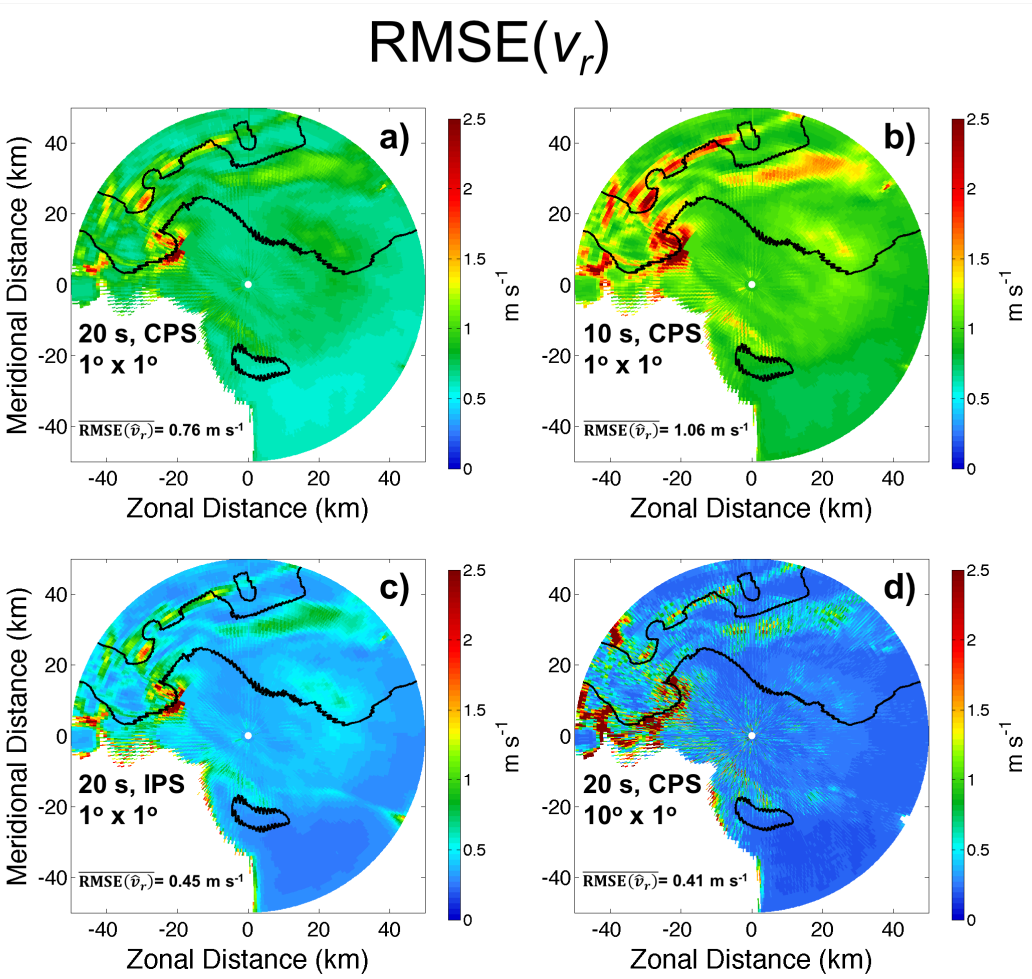

Figure 2.6: As in Fig. 2.3, but for RMSE of v_r. RMSE values listed are the mean values from 15 PPIs, and may deviate from the mean RMSE of the PPI shown by up to 0.01 m s^{-1}.

under different scanning strategies. For the NEXRAD-style scan, 94.3% of pixels are of acceptable data quality for $\hat{v}_r$ (i.e., RMSE($\hat{v}_r$)$<$ 1 m s^{-1}). When the scan time is decreased from 20 s to 10 s, the percentage of pixels with acceptable RMSE($\hat{v}_r$) estimates decreases to 49.5%. So, for a 10 s PPI collecting data in CPS mode,

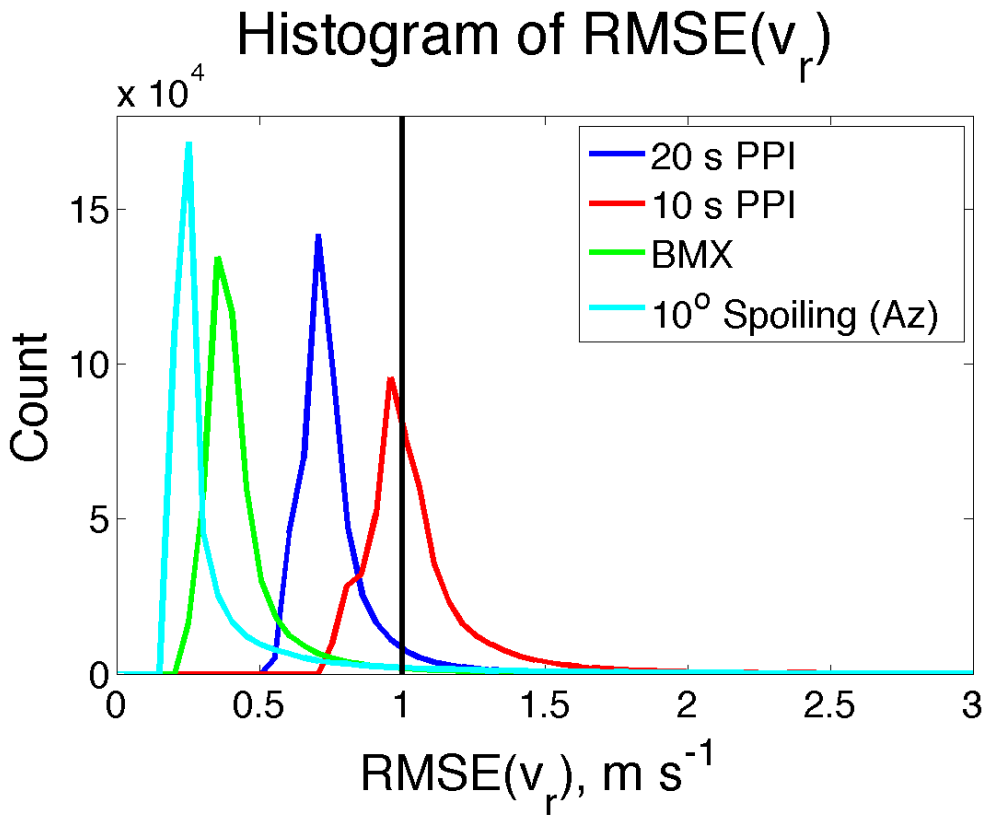

Figure 2.7: As in Fig. 2.4, but for a histogram of v_r. The black vertical line represents the 1 m s^{-1} suggested requirement (see Table 2.2).

over half of the estimates of v_r are not acceptable–and nearly 45% of estimates change from acceptable to unacceptable when moving from 20 s PPIs to 10 s PPIs, based on the 1 m s^{-1} requirement from the initial SENSR PPR (Federal Aviation Administration 2017).

Panel c) in Fig. 2.6 plots RMSE($\hat{v}_r$) for a 20 s PPI where BMX/IPS mode is used. As expected, data quality is generally improved in BMX/IPS mode, compared with data quality in CPS mode. For all 15 PPIs analyzed in BMX mode, the mean

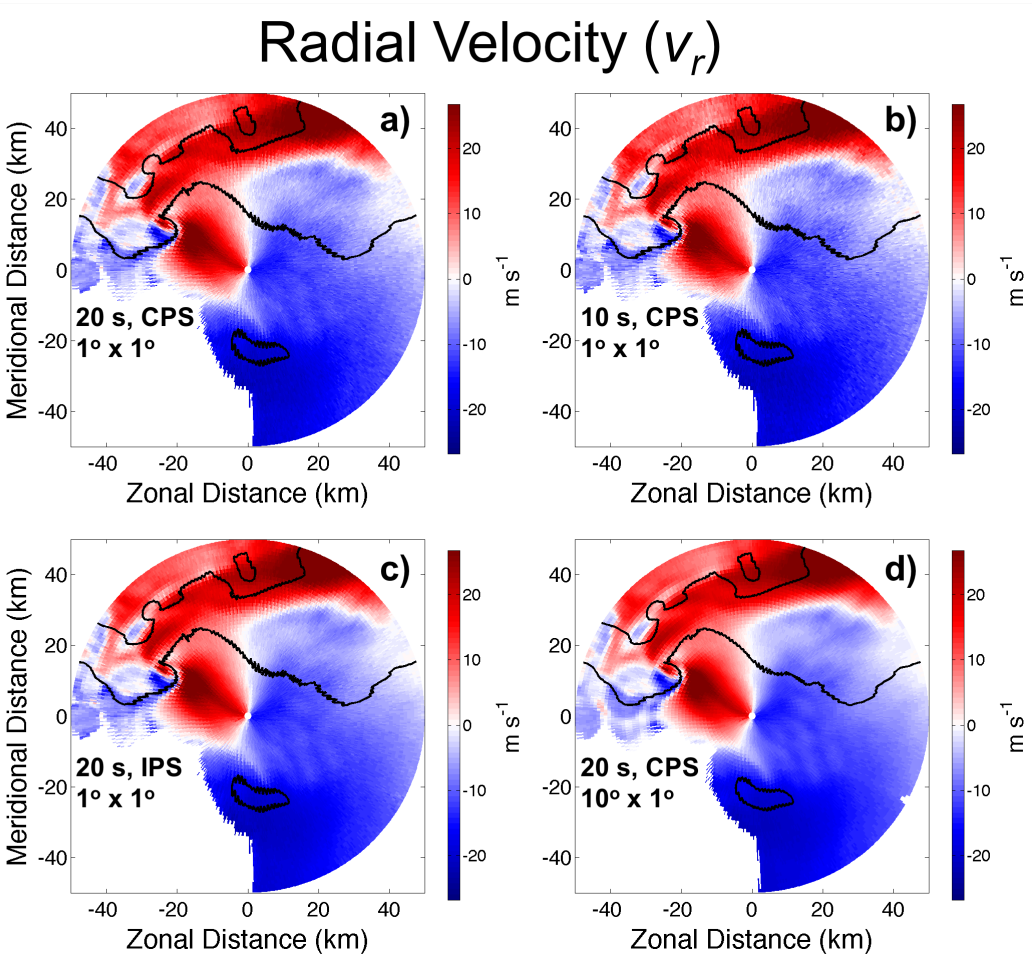

Figure 2.8: As in Fig. 2.5, but for v_r.

RMSE($\hat{v}_r$) is 0.45 m s^{-1}; the corresponding histogram is plotted in Fig. 2.7. The equivalent speedup factor for BMX in this case is 2.85 when comparing the mean RMSE($\hat{v}_r$) of the two scanning methods. In this case, it is also possible to calculate speedup factor based on the percentage of pixels in the domain with acceptable data quality. This is achieved by multiplying the RMSE estimates using BMX by the square root of the speedup factor, and then calculating the percentage of pixels that

have 'acceptable' data quality. Using this method, BMX offers a speedup factor of 1.69 compared to CPS.

An interesting phenomenon that is present in Fig. 2.6c (BMX) that is not present in any of the other panels of this figure (or any panels in Fig. 2.3) is the relatively poor data quality around the periphery of the precipitation echo. Notably, the area along the edge of the storm (to the south and west of the radar) has worse data quality than in CPS mode, in Fig. 2.6a. This result is expected, and is caused by the fact that the number of pulse pairs–and, by extension, the number of samples for estimation of v_r–is reduced by approximately a factor of 2 for BMX, compared to CPS. For example, a scan where 50 pulses per radial are transmitted would result in 50 Z_H samples in both CPS and BMX/IPS modes, 49 v_r samples in CPS mode, but only 25 v_r samples in BMX/IPS mode, although all 25 v_r samples are entirely independent. If inter-pulse correlation ($\rho(T_S)$) is low (as can be the case in low-SNR regions), then it is possible that CPS mode could yield more independent v_r samples than BMX/IPS mode. In this scenario, BMX/IPS data collection mode could produce poorer data quality than CPS data collection mode. This phenomenon corresponds to the portion of Fig. 2.1b for which the improvement factor is less than 1. However, this is dependent on several variables, including spectrum width and the number of pulses used, in addition to SNR. The reduction of v_r data quality in low-SNR environments may be mitigated by adaptive application of BMX in relatively high SNR areas only.

Finally, the difference in data quality between a pencil beam and a 10° azimuthally spoiled beam is analyzed. In Fig. 2.6d, it is clear that most of the domain shows improved data quality when compared to the other three methods. However, there are regions of very poor data quality around the edge of the storm, especially to the south and west of the mesocyclone. Despite this area, the mean RMSE($\hat{v}_r$) for 10° of beam spoiling is 0.41 m s^{-1} (cyan curve in Fig. 2.7). The corresponding speedup factor is 3.44. However, as mentioned in Chapter 2.3.1.1, the higher two-way antenna sidelobes may produce regions where data quality is unacceptable for forecasters. This is exemplified by analyzing the percentage of pixels with acceptable data quality; as previously stated, the 20 s PPI with CPS data collection resulted in 94.3% of the pixels having acceptable data quality for v_r (i.e., RMSE($\hat{v}_r$)$<$ 1 m s^{-1}). For a 10° azimuthally spoiled transmit beam with all other scan parameters held constant, the percentage of 'acceptable' pixels is 94.1%. As a result, no significant improvement in the percentage of pixels with acceptable RMSE($\hat{v}_r$) estimates can be found via beam spoiling in azimuth, due to the introduction of bias from the higher two-way sidelobes.

One interesting feature in Fig. 2.6 compared to Fig. 2.3 is the relative RMSE in the areas of high spectrum width. In Fig. 2.3, RMSE($\hat{Z}_H$) tends to decrease in the areas of high spectrum width, such as those near the mesocyclone and inflow region of the supercell. This is because each estimate of Z_H is produced by a single pulse (i.e., a lag-0 estimator), such that decreased inter-pulse correlation within a pulse pair improves the number of independent samples, thereby improving data quality.

For BMX/IPS, this is reflected mathematically in (2.6) by the fact that in the high-SNR limit, the var($\hat{S}_I$) is directly proportional to $(1 + \rho^2(T_S))$, such that decreasing sample correlation decreases the expected statistical variance. Conversely, RMSE of $\hat{v}_r$ tends to increase in areas where spectrum width is larger. For the variance of radial velocity in (2.7), in the high-SNR limit, var($\hat{v}_r$) is proportional to $\left(\frac{1}{\rho^2(T_S)} - 1\right)$, such that decreasing inter-pulse correlation within a pulse pair increases the resulting variance. The increase in the number of independent samples is why data quality improves for Z_H in areas of high spectrum width, but data quality is degraded for v_r in areas of high spectrum width due to decreased inter-pulse correlation. A more complete mathematical explanation of this phenomenon can be found in Zrnić (1977).

2.3.2 Effect of Beam Spoiling on Mesocyclone Intensity Observations

To assess the impact that radar imaging has on observed mesocyclone intensity, PPIs of v_r with varying degrees and directions of beam spoiling have been simulated. The two-way beam pattern is simulated by multiplying a transmit beam of 1°, 5°, 10°, and 20° in azimuth (1° in elevation), and a narrow (∼1° x 1°) receive beam. Each of the four two-way beam patterns are used to scan the mesocyclone, and the mesocyclone strength is calculated by using ΔV, the difference between the maximum inbound and outbound v_r in the mesocyclone.

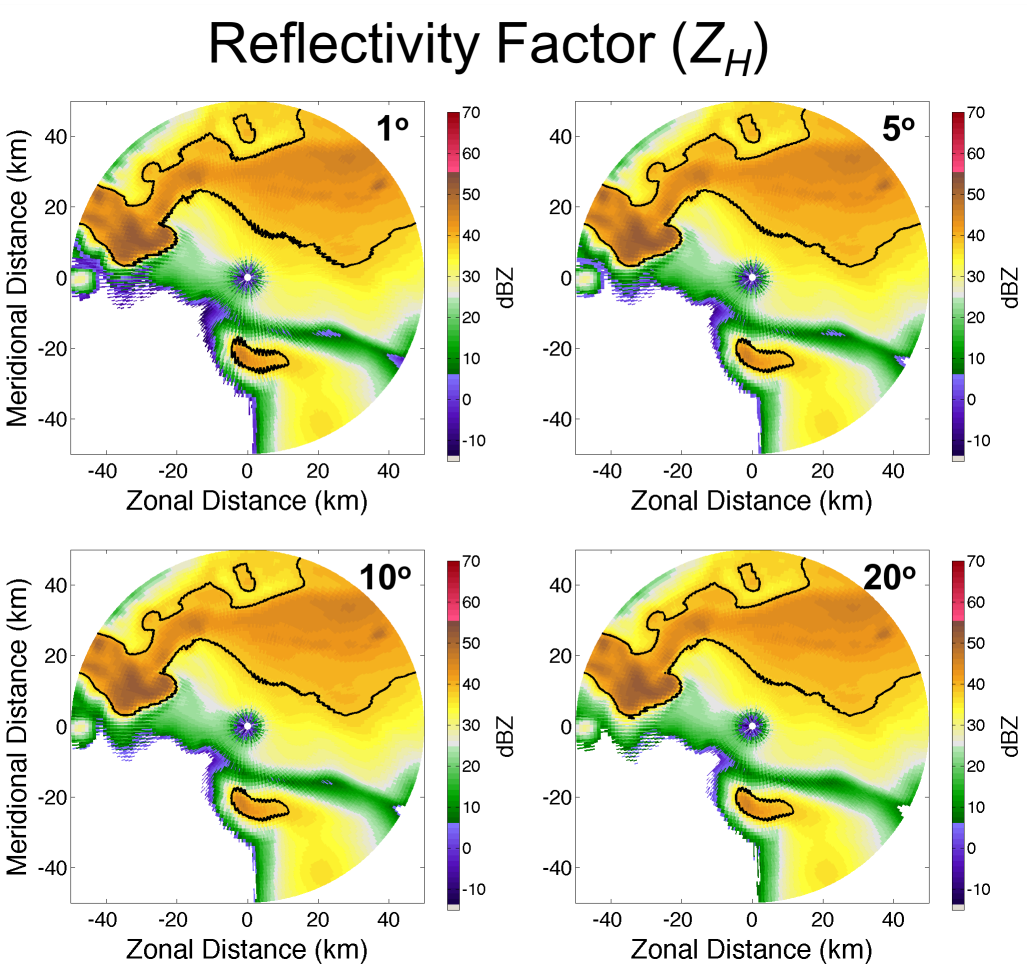

Figure 2.9: This figure plots the underlying Z_H reference fields for a pencil beam (top left), as well as those for a beam spoiled by 5°, 10°, and 20° in azimuth. Note the loss in sensitivity as beam spoiling is increased.

The results of spoiling the transmit beam to 1°, 5°, 10°, and 20° in azimuth are shown in Figs. 2.9 and 2.10. As beam spoiling increases in the azimuthal direction, the measured ΔV begins to decrease; the calculated ΔV values are listed in each panel of Fig. 2.10. With a 1° pencil beam on transmit, the measured ΔV

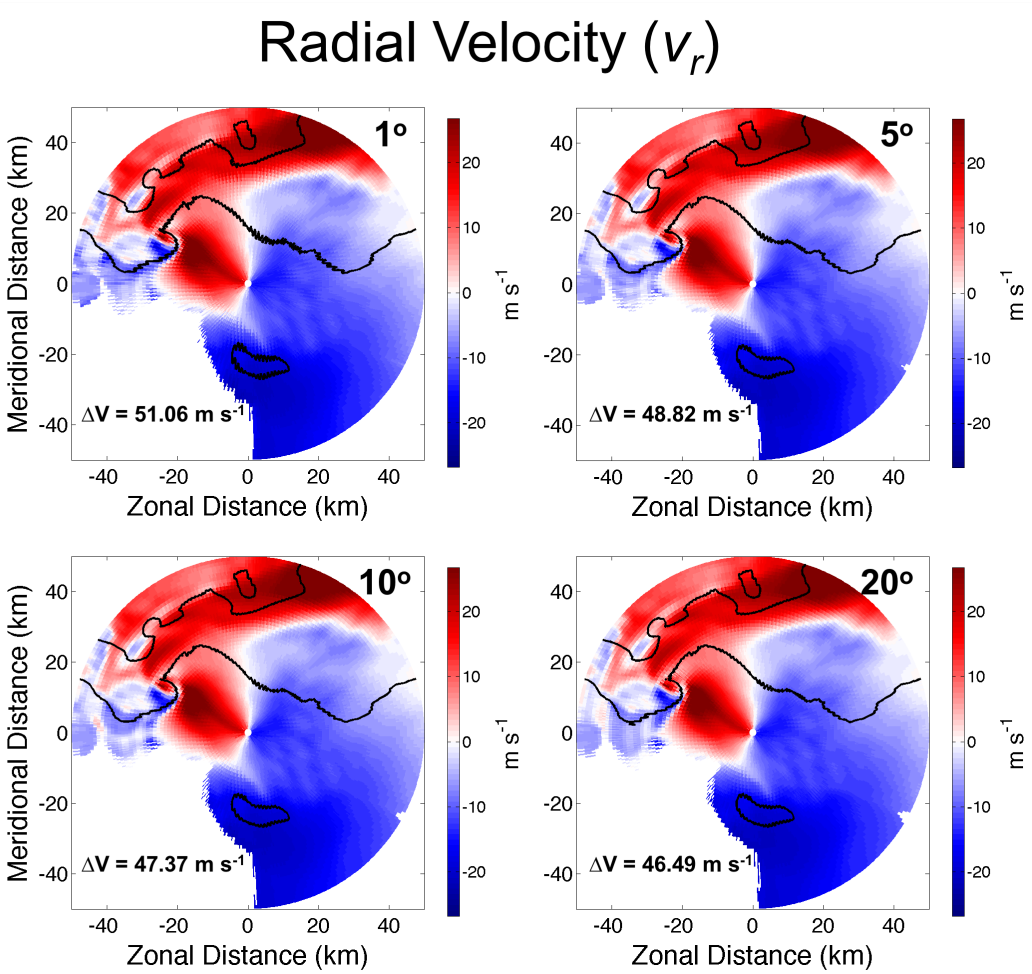

Figure 2.10: As in Fig. 2.9, but for v_r. The value for ΔV in each panel corresponds to the measured mesocyclone intensity with each amount of beam spoiling.

is 51.06 m s^{-1}. When transmit beam spoiling is increased, however, the measured ΔV value continually decreases. When spoiling by 20° on transmit, measured ΔV is 46.49 m s^{-1}. The 4.4–9.0% underestimation in mesocyclone intensity for 5-20° of beam spoiling is caused by 'smearing' of the velocity couplet signature, which can be thought of in similar terms to a low-pass filter.

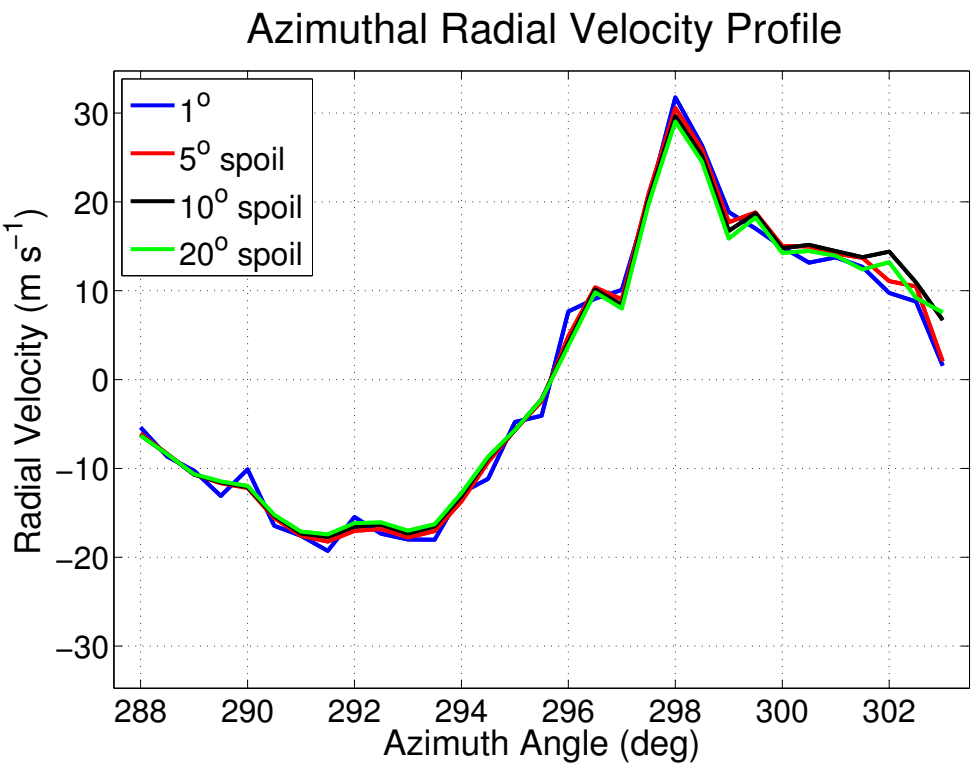

Figure 2.11: The azimuthal radial velocity profile across the rotational couplet at 0.5° in elevation (approximately 300 m AGL). Note that increasing the beam spoiling factor tends to decrease the measured ΔV velocity shear.

This effect can be observed in a radial velocity profile across several angles at a given range (Fig. 2.11). The magnitudes of the extrema are generally smaller for the cases with more beam spoiling (i.e., green curve in Fig. 2.11) compared to the pencil beam case (i.e., dark blue curve in Fig. 2.11). This agrees with Brown et al. (2002), where tornado detection capability is assessed under native and enhanced resolution for a simulated WSR-88D. The results from Brown et al. (2002) show that Doppler velocity signatures generally appear stronger when the azimuthal sampling

is reduced from 1.0° to 0.5°. Our study is different, however, in that a full beam pattern is simulated for a notional phased array radar (i.e., wide beam on transmit and narrow beam on receive).

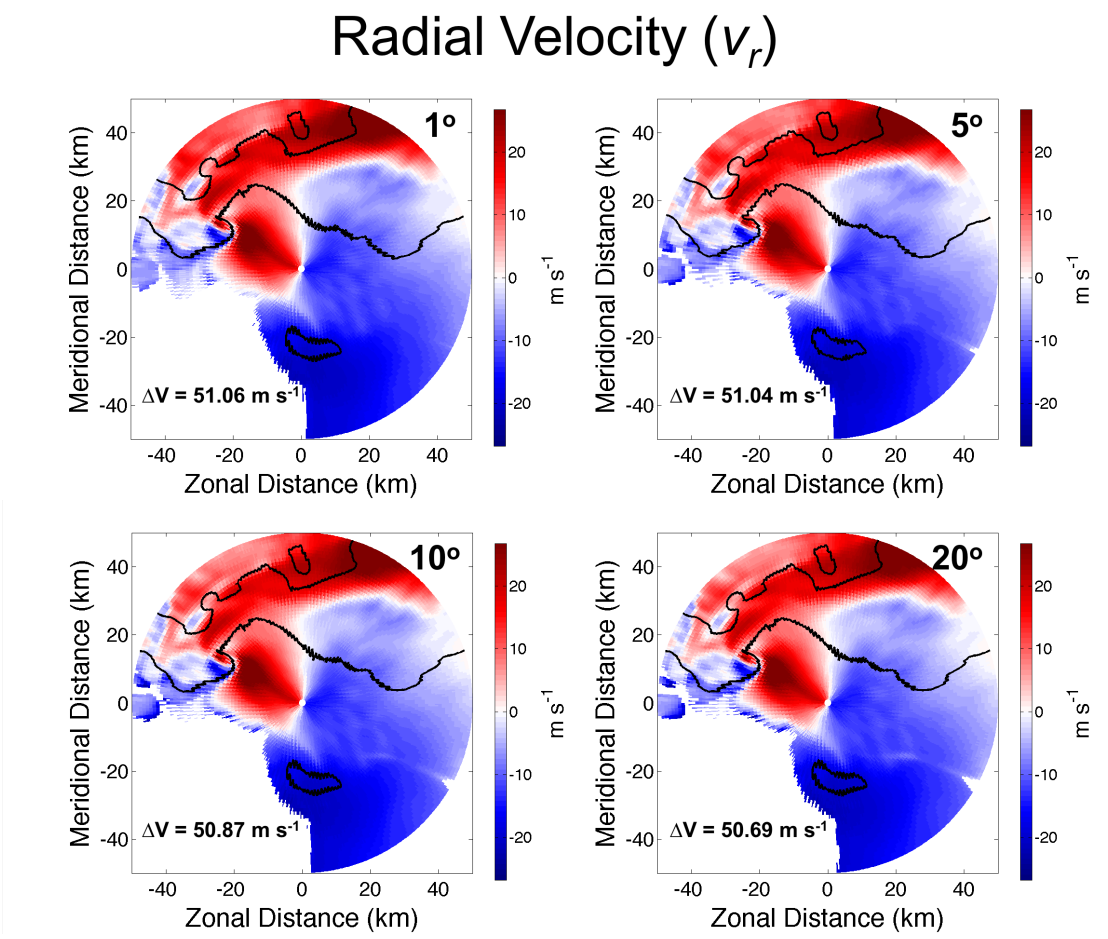

Figure 2.12: As in Fig. 2.10, but for spoiling in elevation, rather than azimuth.

This procedure is also performed for 1°, 5°, 10°, and 20° of spoiling in the elevation dimension. The interesting result for this supercell case is that the calculated ΔV values in and around the mesocyclone do not change appreciably when spoiling is increased in elevation (Fig. 2.12). It is hypothesized that this result is due to

the fact that for this case, the primary Z_H and v_r gradients are in the azimuthal dimension, rather than the elevation dimension. While the result in this study indicates that spoiling in elevation may be favorable compared to spoiling in azimuth for correctly assessing mesocyclone strength, this is only one application of assessing the effect of radar imaging. This result may change for a different case, if stronger vertical gradients in Z_H and/or v_r are present. For example, the Atmospheric Imaging Radar (AIR; Isom et al. 2013) operates by transmitting a 1° x 20° (azimuth x elevation) beam; artifacts from vertical sidelobes and/or grating lobes have been shown in some datasets collected by the AIR (Kurdzo et al. 2017; Mahre et al. 2018).

2.4 Conclusions

In this study, data quality in and around a simulated supercell is assessed by using a large-domain weather radar simulator. This research is done in order to inform decisions about which scan speedup strategy (or combination of strategies) can provide the highest quality data and is shown here for a prototypical high-impact weather event (tornadic supercell). The results of this study can be used to guide the design of VCPs for a NexPAR system, and can be used to assess the expected data quality for various volumetric update times. Scanning strategies tested include CPS data collection mode, BMX/IPS data collection mode, decreasing the number of samples per radial, and transmit beam spoiling (radar imaging).

The results in this study show that meeting a rapid-scan timeline simply by decreasing dwell time offers extremely poor data quality compared to typical sampling rates, as expected. When decreasing the number of samples per radial by a factor of 2, the mean RMSE($\hat{Z}_H$) increased from 1.77 dBZ to 2.26 dBZ, while the mean RMSE($\hat{v}_r$) increased from 0.76 m s^{-1} to 1.06 m s^{-1}. This reduced the percentage of pixels with acceptable data quality (with respect to v_r) from 94.3% to 49.5%. This result is consistent with expectations, such that other data collection and scan speedup methods need to be employed to preserve data quality.

Another scan speedup method evaluated in this study is beam multiplexing (BMX). This method shows considerable promise for obtaining rapid-scan weather radar data with acceptable data quality. For RMSE($\hat{Z}_H$), it is shown that a speedup factor of 2.84 is achievable, such that the scan can be sped up by a factor of 2.84 without an increase in the mean RMSE($\hat{Z}_H$) value. For a similar assessment of v_r data quality, the expected speedup factor is 1.69–2.85. This result of BMX offering a speedup factor of 1.69–2.85 is generally consistent with results in Yu et al. (2007), which posited that a speedup factor of 2–4 should be possible with BMX. The results of this study show significant promise for BMX as a viable option for meeting a rapid-scan timeline. While this technique must be used judiciously at low levels and in low SNR regions, and is not compatible with staggered PRT data collection or ground clutter filtering, it generally offers a significant improvement in data quality, and the time in which a full volume can be scanned without degrading data quality.

In addition to using BMX to improve volumetric update times, beam spoiling has previously been shown to be a viable option for speeding up total volumetric update time. When calculating the speedup factor associated with a 10° azimuthally spoiled beam, each scan can be sped up by a factor of 2.29–3.44 when considering the mean RMSE value to be the metric for data quality. However, this does not fully capture the effects that a region of extremely poor data quality might have on an operational forecaster. For v_r considerations, the speedup factor reduces to approximately 1 when calculating the percentage of 'acceptable' pixels between the two methods, such that no net gain is afforded. Additionally, regions of extremely biased data may be present, and sensitivity to weak echoes is reduced. Thus, radar imaging should not be applied to an entire domain without first analyzing which areas are most susceptible to negative effects of beam spoiling (i.e., areas with a strong reflectivity or radial velocity gradient). This is one area where adaptive scanning and/or cognitive radar may help to realize benefits of beam spoiling. Because both BMX and radar imaging are most easily achievable with an all-digital phased array radar, the results presented in this study can help to inform decisions about possible radar architectures for a future NEXRAD replacement system.

Finally, the effects of radar imaging on the calculated mesocyclone strength are analyzed and discussed. It is shown that the derived mesocyclone strength decreases as beam spoiling increases in azimuth. This is expected, and echoes results in Brown et al. (2002). An interesting result from this study is that the magnitude of change in derived ΔV is 4.4–9.0% when spoiling in azimuth by 5° to 20°. Additionally, ΔV

is calculated for 1°, 5°, 10°, and 20° of spoiling in elevation; for the case analyzed in this study, there is no appreciable effect on ΔV. It is believed that this is due to a lack of strong reflectivity or velocity gradients in the vertical dimension, and the fact that the rotation (mesocyclone) is vertically aligned. Based on these results alone, spoiling in elevation is favorable compared to spoiling in azimuth for examining trends in rotational characteristics. However, further study will be necessary to examine if spoiling in elevation is better for estimating ΔV for mesocyclones and tornadoes in most or all cases.

In the future, we plan to extend this study to cover adaptive scanning and its effects on data quality. One advantage of a fully digital phased array radar is the ability to control the location and shape of the radar beam. Controlling the radar beam location can allow for more pulses to be sent out along radials of interest, as fewer pulses are sent out along radials of lesser interest. Adaptive reallocation of receive beam clusters (adaptive radar imaging) has been explored in Weber et al. (2017) to speed up scans while minimizing effects on data quality from higher sidelobes on transmit. It would be a goal of such a study to adaptively reallocate pulses to improve data quality for a set scan time, or to maintain a certain level of data quality while decreasing scan time. Additionally, it would be beneficial to test these scanning strategies on an all-digital phased array radar system (i.e., Horus; Palmer et al. 2019) to verify the simulated results, and to compare simulated results to observed cases of various weather phenomena. This would be especially beneficial for assessing polarimetric data quality under various scanning conditions;

polarimetric data quality is not considered in this study because the contributions of the phased array radar architecture to the expected radar variable errors could be larger than the contributions due to the statistical fluctuations alone. However, addressing the statistical fluctuations of polarimetric data is still an area which will have to be addressed for a NexPAR system in the future. For future uses of a radar simulator such as RSim, the effects of the radar architecture and design on radar data quality should be considered.

This study can also be expanded to other methods of scan speedup. For example, the multiple-beam technique (MBT) proposed in Zrnić et al. (2015) can be implemented under various conditions (varying the number of beams, the pulse length, etc.). Additionally, this framework can be used to compare the changes in expected data quality when pulse compression techniques are used to increase the number of independent samples in the along-range direction. Finally, this simulation framework can be applied to multiple meteorological events to evaluate if these findings are representative of scenarios beyond the supercell case considered in this study (e.g., different convective modes such as squall lines or ordinary convection, flash flooding, and quantitative precipitation estimation).

Chapter 3

Quantifying the Benefits of a Rapid-Scan PAR for Tornado Detection

3.1 Rapid-Scan Introduction

In Chapter 2, the primary focus is on ensuring that fast updates can be achieved on a rapid-scan PAR for weather observations, with special attention paid to the specific scan strategies and signal processing techniques that can provide high quality radar data in a relatively short scan time. This portion of the dissertation research is intended to quantify the benefits of a rapid-scan weather radar system in an objective manner.

There are two primary goals in this chapter: the first is to use a tornadogenesis simulation and a tornado detection algorithm to show how rapidly changes in tornado intensity and debris lofting occur, while classifying changes between differing heights and debris counts with time. This is the first study of the correlation between tornado intensity and the amount of debris lofting by using a storm-scale simulation. The second goal is to measure how changes in tornado detection latency

time are affected by radar update time, by simulating a mature tornado while artificially changing the debris contribution. More succinctly, as it relates to faster updates, Chapter 2 is intended to answer the question of 'how?', whereas this chapter is intended to answer the question of 'why?', for a subset of cases where rapid updates are believed to be useful.

3.1.1 Background

As stated in Chapter 1, a primary goal of NOAA/NWS for a NEXRAD replacement system is an improvement in the volumetric update time for the radars. While NEXRAD offers volumetric updates on the order of ∼5 min, this is not sufficient for complete analysis of many rapidly evolving phenomena such as tornadoes (French et al. 2013; Wurman and Kosiba 2013; French et al. 2014; Kurdzo et al. 2015a; Wakimoto et al. 2015; Houser et al. 2015, 2016; Kurdzo et al. 2017; Mahre et al. 2018; Bluestein et al. 2019; Griffin et al. 2019), severe storms (Carbone et al. 1985; Zrnić et al. 2007; Heinselman et al. 2008; Newman and Heinselman 2012; Tanamachi et al. 2015; Tanamachi and Heinselman 2016; Kuster et al. 2016), and QPE applications (e.g., 1-min updates assessed in Wang and Chandrasekar 2010).

In an operational setting, there are multiple methods that can be used by forecasters to detect a tornado for warning issuance. During the advent of Doppler radar for research and operational use, a tornado vortex signature (TVS, roughly defined

as a region of significant shear in radial velocity indicating strong vorticity) was theorized to be useful for tornado detection (Donaldson Jr. 1970); this was confirmed for use by Burgess et al. (1975) and Brown et al. (1978). With the development (and now operational use) of polarimetric weather radar, the use of polarimetric signatures for tornado detection has been studied in the past 15 years. A primary polarimetric signature for tornado detection is a tornadic debris signature, or TDS.

A TDS is generally defined as a co-location of a tornado vortex signature, elevated radar reflectivity factor, and a region of lowered co-polar correlation coefficient (ρ_{hv}), indicative of lofted debris (Ryzhkov et al. 2005; Bluestein et al. 2007; Kumjian and Ryzhkov 2008). In previous studies, TDS characteristics have been leveraged to achieve both automated tornado detection (by fuzzy-logic algorithms (Snyder and Ryzhkov 2015) or by neuro-fuzzy algorithms (Wang et al. 2008; Wang and Yu 2015)) and manual tornado detection. The presence of a TDS is indicative of a tornado that is strong enough to loft debris, and is therefore more common for stronger tornadoes (Schultz et al. 2012; Bodine et al. 2013; Van Den Broeke and Jauernic 2014). Schultz et al. (2012) and Bodine et al. (2013) found that the characteristics of a TDS (e.g., height and area) were correlated with EF-scale damage. Expanding on these smaller sample size studies, it has been shown in Van Den Broeke and Jauernic (2014) and Thompson et al. (2017) that changes in the TDS may correlate with changes in tornado intensity based on analysis of hundreds of cases. Conversely, debris loading can affect the tornado dynamics (and, subsequently, the strength of the tornado). Lewellen et al. (2008) and Bodine et al. (2016a) examined the effect

of debris loading on low-level tornado dynamics; Lewellen et al. (2008) found that the low-level wind speeds could be reduced by as much as 50%, and Bodine et al. (2016a) found that wind speeds below 10 m AGL could be reduced by 30–60% under high debris loading.

It has previously been shown that TDSs can improve tornado detection and lead time. In fact, Van Den Broeke (2015) found that about 10% of tornadoes have a TDS prior to tornadogenesis. Furthermore, Van Den Broeke (2017) found that tornado warning lead times could be improved by using TDSs in negative lead time scenarios (i.e., when a tornado is present but unwarned), as well as in cases where no warning is issued at all. TDSs are usually observed at close range (<100 km) due to beam broadening effects and poorer low-level sampling at longer radar standoff ranges (Kumjian and Ryzhkov 2008; Bodine et al. 2013). Previous studies have shown that tornado strength, tornado path length, debris type and availability, and distance between the tornado and the radar have the most bearing on whether or not a TDS is detected (Van Den Broeke and Jauernic 2014). Additionally, Van Den Broeke and Jauernic (2014) show that TDSs typically extend to 1 km to 4 km above ground level (AGL), such that scans in the lowest few km AGL are necessary to properly detect a TDS. Taken alongside the fact that tornadoes typically evolve on the order of a minute or less, this would indicate that rapid re-sampling of the lowest elevation angles is paramount to early detection of tornadoes.

3.1.2 Previous Research on Rapid-Scan Benefits

Tornadoes in particular require rapid radar updates for timely detection and subsequent warning issuance. It has been shown that NEXRAD has improved tornado warning lead times (Polger et al. 1994; National Research Council 1995; Bieringer and Ray 1996; Simmons and Sutter 2005), and that there is a proven link between tornado warning lead time and the number of injuries caused by a tornado (Simmons and Sutter 2008).

The utility of rapid-scan weather radar data (i.e., finer temporal resolution than NEXRAD) for both operations and research has been previously demonstrated. For forecasting and operational purposes, Heinselman et al. (2012) and Wilson et al. (2017) have shown that more rapid radar updates leads to increased lead time, improved forecaster confidence, a higher probability of detection, and a lower false alarm ratio for tornadoes in a simulated operational setting. In a more climatological study, Cho and Kurdzo (2019) developed a benefit model for tornado detection across the CONUS. Their study found that NEXRAD provides a tornado-based benefit of about $490 million per year, and moving to a rapid-scanning radar system could coincide with an additional benefit of $157 million per year. It is important to note, however, that this benefit is specific to tornadoes; additional benefits are associated with flash flood detection (Cho and Kurdzo 2020) and other radar-based warnings such as those for hail and severe winds.

Wolfson and Meuse (1993) also showed the utility of rapid updates in operations; they found that reducing the scan time from 3 min to 1 min in a Terminal Doppler Weather Radar (TDWR) significantly increases the lead time for automated microburst detection (2.2 min to 5.2 min of lead time), leading to improved capability of aircraft to avoid hazardous areas on takeoff and landing. Additionally, data assimilation studies have shown the benefit of assimilating rapid-scan weather radar data to improve short-term numerical weather prediction (NWP) model accuracy (Yussouf and Stensrud 2010; Sun et al. 2014; Supinie et al. 2017; Huang et al. 2020). Thus, it is believed that decreasing the volumetric update time to $\sim$1 min would be extremely beneficial for a future national weather radar network.

3.2 High-Resolution Observations of TDS & TVS Growth

As stated in section 3.1, the first goal of this chapter is to attempt to quantify the timescales on which a major signature of tornadoes (a TDS) grows and evolves. This is analyzed as a function of time, height, and debris concentration, and is compared with changes in the TVS, where herein ΔV is used as a proxy for TVS. This is done in order to assess the necessary temporal resolution for proper observations of tornadoes for both research and operations. The methods and techniques for assessing the TDS and TVS are described within section 3.2.1, and the results of this portion of the study are described in section 3.2.2.

3.2.1 Methods

3.2.1.1 SimRadar

In the absence of a radar testbed where meteorologists can evaluate the collected data, a radar simulator may be used. Radar simulators can reveal important information regarding the expected derived fields from a number of controlled input scenarios. This is especially important, as a radar simulator can recreate the same scenario, such that the effect of radar and environment variables (scan time, debris concentration, etc.) can be evaluated directly. This study utilizes output from a radar simulator ("SimRadar") designed for tornado-scale simulations to assess and quantify the benefits of a rapid-scanning weather radar system.

SimRadar (Cheong et al. 2017) is a dual-polarization radar emulator that combines high-resolution numerical model input with dual-polarization electromagnetic scattering data. A unique feature of SimRadar is the ability to accurately simulate trajectories and radar cross-sections (RCSs) for various debris types, including leaves and wood boards (2" x 4" x 12" in size) which are used in this study. The debris trajectories are computed using a 6 degree-of-freedom model that is based on drag and moment coefficients derived from wind tunnel measurements, while debris RCSs are computed from a lookup table based on the orientation angle of the debris. SimRadar simulates in-phase and quadrature (I/Q) data by applying realistic range and angular weighting functions, and coherently summing the point scatterers. The I/Q data can then be used to compute moment data, including reflectivity factor

(both horizontal and vertical), differential reflectivity, copolar correlation coefficient, radial velocity, and spectrum width. More information regarding SimRadar can be found in Cheong et al. (2017) and Umeyama et al. (2018).

For this study, various concentrations of debris are used; the two types of debris simulated herein are leaves and wood boards. Other debris types such as metal sheets and bricks are also supported by SimRadar. Additionally, raindrops are simulated with a Marshall-Palmer drop-size distribution (DSD). The resulting probability density function (PDF) is one that simulates five sizes of raindrops: 1, 2, 3, 4, and 5 mm in diameter. Each size within a hydrometeor distributions is simulated as a point scatterer, where each scatterer has the same DSD at the beginning of the radar simulation. The initial PDF values (i.e., at t = 0 s) for each of the five raindrop sizes are as follows: 90% of the drops are 1 mm in size, 9% are 2 mm in size, 0.9% are 3 mm in size, 0.09% are 4 mm in size, and 0.009% are 5 mm in size. At each timestep of the radar simulation, the DSD at each point can change, and the resulting RCS contribution from hydrometeors is recalculated. The changing DSD is a result of different sizes of hydrometeors having different trajectories; for example, this method allows for larger hydrometeors to be centrifuged when advecting around a tornado.

In this simulation, the RCS of debris is scaled below 50 m AGL. The exact scaling follows the equation

$$\sigma' = \frac{\sigma}{1 + e^{-(h-25)/3}} \tag{3.1}$$

where σ is the inherent RCS, σ' is the scaled RCS, and h is the height of the debris AGL, in meters. A plot of the RCS scaling factor as a function of height is

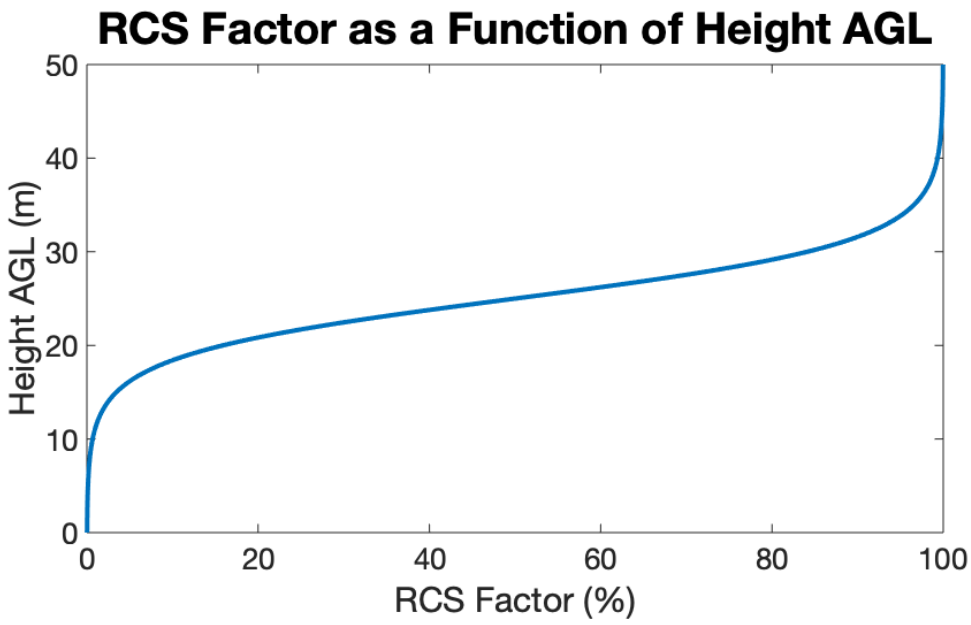

Figure 3.1: RCS factor as a function of the height of the debris above ground level. Note that above ∼30 m AGL, over 90% of the RCS factor is 'activated'.

shown in Fig. 3.1. This RCS scaling is done in order to ensure that debris moving across/near the ground do not affect the measured radar variables, as debris are populated in the domain prior to tornadogenesis. Debris are generated at 10 m AGL, and at a random location in the x-y plane within an inner domain of N m by N m (where N = 400 m or 1000 m) around the center of the scan domain. Debris are generated at 10 m in height (rather than a more realistic height of 1–2 m AGL) to increase the efficiency of the debris lofting within the model.

The simulations in the first goal of this study use the Cloud Model 1 (CM1; Bryan and Fritsch 2002), described further in section 3.2.1.2. The CM1 model used herein provides a realistic wind field before, during, and after tornadogenesis of a rapidly evolving, violent tornado at 10 m resolution (Orf 2019). A visualization of SimRadar using the CM1 model wind field is shown in Fig. S1 (`https://drive.google.com/open?id=1ebWLGJtVX7CRIsLds4xmzaFWi1Hgtyf1`), where the tornado is in the mature stage.

The scan pattern for this study uses 25 pulses per radial, with a pulse repetition time (PRT) of 0.25 μs. Such a short PRT is chosen to avoid velocity aliasing, which could affect TDS detection, because the TDS classification uses velocity shear (described in more detail in section 3.2.1.3). The center of the analysis domain is located approximately 14.75 km away from the radar, and spans 1.44 km in range and approximately 2.4 km in azimuth (-5° to 5°). The CM1 domain is restricted to 2 km x 2 km x 700 m in the zonal, meridional, and height dimensions, respectively. The radar uses a beamwidth of 1° in azimuth and elevation, and is oversampled to 0.5° in azimuth, with a range resolution of 30 m. Each individual plan-position indicator (PPI) is assumed to take 1 s, and 6 PPIs are sampled for each volume scan (i.e., a 6 s volumetric update time).

An example of output from SimRadar is shown in Fig. 3.2, where 350,000 leaves and 150,000 wood boards have been released into the scan domain, along with hydrometeors. The debris are placed in the domain at the beginning of the simulation, and new pieces of debris are replenished whenever a piece of debris exits the scan

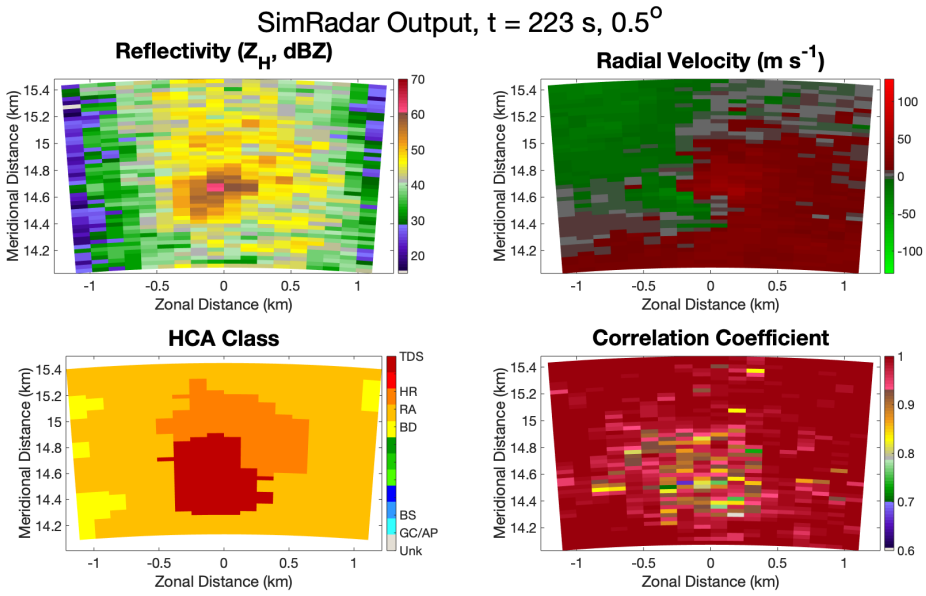

Figure 3.2: Example output from SimRadar. Panels show radar reflectivity factor (Z_H), radial velocity (v_r), HCA class, and correlation coefficient (ρ_{hv}).

domain; however, these pieces of debris are not lofted initially because of weak vertical motion such that they do not reach the altitude of the radar beam and are artificially suppressed by the RCS scaling (Fig. 3.1). The example shown in Fig. 3.2 closely coincides in time with tornadogenesis and with initial debris lofting. A rotational couplet can be observed in the v_r field, and a region of high Z_H and lowered ρ_{hv} is observed ($\sim$14.6 km in meridional range, near the center in the zonal dimension). As debris are lofted by the tornado, the area of high Z_H and lowered ρ_{hv} grows with time. This causes an increase in the total area identified as a TDS (dark red pixels in Fig. 3.2). This behavior of increasing Z_H and decreasing ρ_{hv} and Z_{DR} (not shown) is consistent with the observed evolution of TDSs during and just

after tornadogenesis (Ryzhkov et al. 2005; Bodine et al. 2013; Van Den Broeke and Jauernic 2014). However, these studies have used NEXRAD data which lacked the temporal resolution to document the time scales over which this occurs.

3.2.1.2 Cloud Model 1 (CM1)

To realistically simulate tornadogenesis, version 16 of the Cloud Model 1 (CM1; Bryan and Fritsch 2002) is used, with a 10 s temporal resolution. CM1 is a three-dimensional, nonhydrostatic cloud model that is primarily used for idealized simulations of storms and tornadoes (Orf et al. 2017; Orf 2019). For the simulation used in this study, a sounding in the environment of the 24 May 2011 El Reno, OK EF-5 tornado is used (French et al. 2015; Houser et al. 2015; Tanamachi et al. 2015; Orf et al. 2017). The near-storm environment is associated with very large instability and shear (SBCAPE of 4893 J kg^{-1} and 27 m s^{-1} 0-6 km wind shear). Other environmental parameters (528 m LCL, 371 m^2 s^2 SRH) are also very favorable for supercells and tornadoes. The sounding and hodograph used is shown in Fig. 1 of Orf et al. (2017). The near-storm thermodynamic conditions from the re-analysis data are used as an input into the CM1 model, which then produces a simulated violent tornado.

3.2.1.3 Hydrometeor Classification Algorithm with Tornado Class

To assess the presence of a tornado, a hydrometeor classification algorithm (HCA) is used. An HCA is a fuzzy-logic algorithm that uses input from several radar moment

variables–reflectivity factor, differential reflectivity, correlation coefficient, etc.–and uses a set of membership functions to determine the most likely class at each radar pixel.

A membership function is a trapezoidal class- and variable-specific function, which maps a variable into a probabilistic space (zero to one) based on its correlation with a specific class. For example, the membership function for Z_H for the 'rain' class is 0 below 5 dBZ, linearly increases to a value of 1 between 5 dBZ and 10 dBZ, remains at a value of 1 between 10 dBZ and 45 dBZ, and linearly decreases back to 0 between 45 dBZ and 50 dBZ. An example membership function for variable x of a given class is shown in Fig. 3.3. In the notation of the example membership function of Fig. 3.3, 5, 10, 45, and 50 dBZ are the x_1, x_2, x_3, and x_4 values, respectively. That notation of x_i values, where $i = 1$–4, will be used herein.

Each class and variable has its own membership function, as well as its own weight between 0 and 1. At each pixel, there is an aggregation value for each potential class, which is then normalized by the sum of the weights for each potential class. This yields a value of 0 to 1 for each potential class; the class with the highest 'score' from the HCA is then determined to be the most likely class at a given radar pixel. Because of the varying sums of weights, 'ties' between multiple classes for the most likely class are uncommon. In real-world data, ties would be resolved by the use of confidence vectors ($\mathbf{Q}$). However, in the simulations in this study, 'ties' are rare enough even without confidence vectors (<0.1% of pixels) that they are not believed to significantly alter the results of this study.

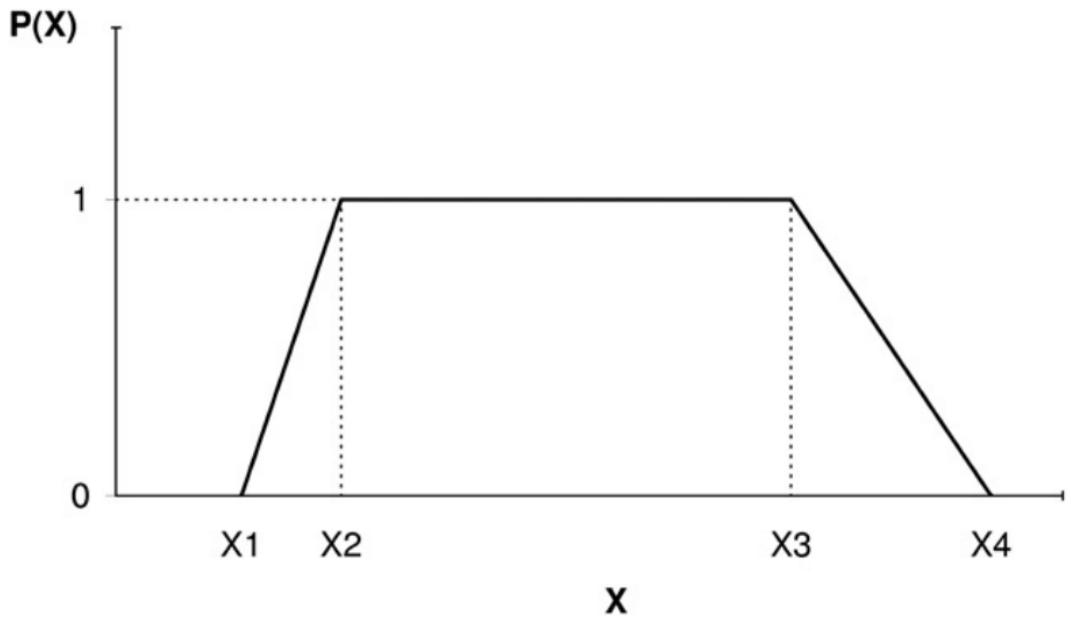

Figure 3.3: A generalized membership function for variable x for a random class. Figure adapted from Snyder and Ryzhkov (2015).

The operational version of the HCA is defined in Park et al. (2009), and uses six variables (Z_H, Z_{DR}, ρ_{hv}, K_{DP}, and spatial variance of Z_H and Φ_{DP}) to discriminate between 10 possible classes: ground clutter and anomalous propagation (GC/AP), biological scatterers (BS), dry snow (DS), wet snow (WS), ice crystals (CR), graupel (GR), large raindrops (BD), light/moderate rain (RA), heavy rain (HR), and rain & hail (RH). Since these simulations do not include frozen precipitation classes, the classes involving ice, snow, or hail (DS, WS, CR, GR, and RH) are not considered in this study, as well as the 'large hail' and 'giant hail' classes that have been added to the operational HCA in recent years. Additionally, because 1) the number of pulses per radial in this simulation is relatively small, and 2) specific differential

phase (K_{DP}) generally requires significant averaging in range, K_{DP} is not considered in this implementation of the HCA. This only affects the HR class; without K_{DP} measurements, the weights of the RA and HR classes are identical, and only the membership functions of Z_H and ρ_{hv} differentiate the two.

The non-suppressed classes (GC/AP, BS, BD, RA, and HR) are otherwise assessed using the same thresholds, weights, and membership functions as those in Park et al. (2009), although confidence vectors ($\mathbf{Q}$) are not considered herein. Hard thresholds are then used to suppress incorrect class identification, following Table 3 in Park et al. (2009). After the initial HCA is run, a mode filter (5 range gates x 3 azimuth angles) is run in order to 'smooth' the output, suppress some spurious classifications, and mitigate major effects of any 'ties' between classes in the filtered region. If multiple modes exist in the filtered region, the region is iteratively expanded by 2 range gates and 2 azimuth angles until only one mode exists.

In addition to these five classes, another class (TDS) is evaluated using the variables outlined in Snyder and Ryzhkov (2015). The TDS class uses the same six variables as the operational HCA, as well as a dilated azimuthal shear (AS) variable (Snyder and Ryzhkov 2015). The TDS class is shown in this study to predict a TDS in areas near the center of rotation after tornadogenesis, and is generally co-located with regions of high Z_H and/or lowered ρ_{hv}, as predicted in section 3.1. The results from this analysis are shown in sections 3.2.2.2 and 3.2.2.3.

3.2.2 Results

3.2.2.1 CM1 Evolution: TVS and Vertical Velocity

An analysis of the model-derived maximum and 99.9^{th} percentile vertical velocity (w) is shown in Figs. 3.4 and 3.5, and an analysis of the radar-derived ΔV is shown in Fig. 3.6. One of the primary factors that influences debris lofting is the vertical (updraft) velocity. The 99.9^{th} percentile of vertical velocity is plotted in Fig. 3.5 (rather than maximum velocity) such that a single grid point of high w cannot bias the w estimate, when a single grid point with large w may not necessarily be representative of the lofting over a large region. The 99.9^{th} percentile represents the 48 grid points (out of 48,400) with the largest vertical velocities, corresponding to an area of 4800 m^2. In Fig. 3.4, it is clear that between t = 250 s and t = 300 s, there is a sudden increase in w at all analyzed levels; this phenomenon is still present (although somewhat muted) in Fig. 3.5. By comparing the increase in w with ΔV in Fig. 3.6, it is clear that the increase in w coincides with the time at which the ΔV estimates at 0.5° begins to deviate from those at 1.3° and 2.4°. Prior to t = 250 s, the ΔV estimates between the three elevations correspond closely. After this time, ΔV at 0.5° is lower than ΔV at 1.3° and 2.4°, likely because lofted heavier debris (wood boards) is causing a negative bias in the derived wind field (caused by drag, such that wood boards will dominate the spectrum and move more slowly than the background wind). This result of a negative bias in radar-derived wind speed agrees with previous research (e.g., Dowell et al. 2005), which showed that larger

debris moves more slowly than the surrounding air motion. These heavier debris are expected to primarily be lofted after an increase in w.

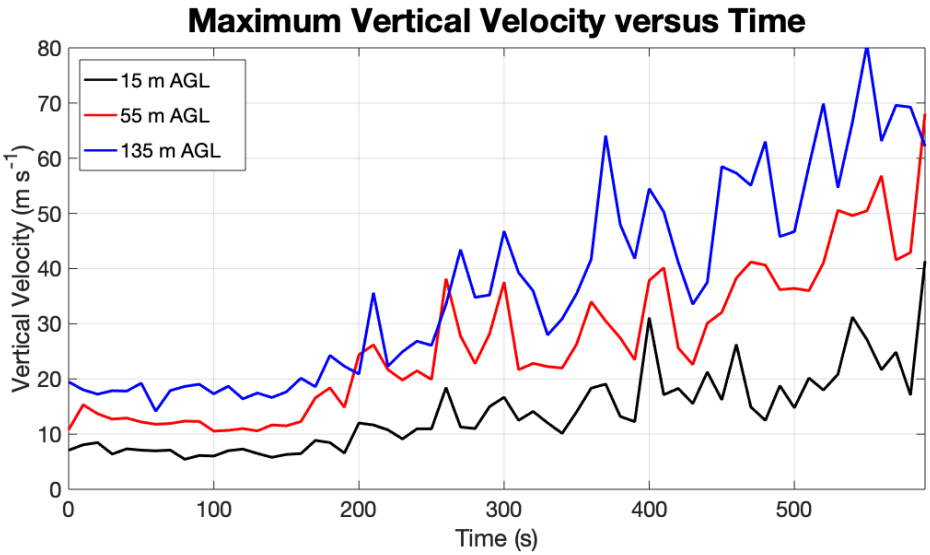

Figure 3.4: The maximum vertical velocity at 15, 55, and 135 m AGL at each CM1 timestep (10 s apart).

Although an automated TVS algorithm exists, this algorithm is not implemented in this study. Instead, tornado intensity is quantified in terms of ΔV. As shorthand, the tornado strength (measured in terms of ΔV) is sometimes referred to as TVS strength in this study, such that the development of both the TVS and TDS are tracked and analyzed as a function of time, height, and debris count. The TVS is calculated as the magnitude of difference between the maximum inbound and maximum outbound radial velocities in the vicinity of the tornado at a given time and elevation angle.

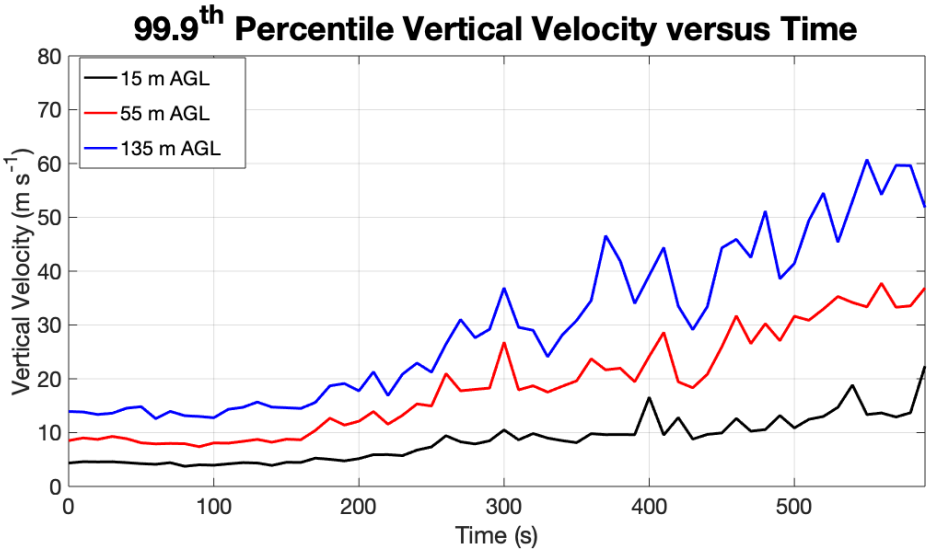

Figure 3.5: The 99.9^{th} percentile of vertical velocity at 15, 55, and 135 m AGL at each CM1 timestep (10 s apart).

3.2.2.2 High-Resolution Observations of TDS Growth: Small Debris Initiation Domain

In this portion of the study, the primary variable analyzed is the areal extent of the TDS, as determined by the HCA class method described above. Initially, SimRadar was run using the CM1 model as the input model wind field, with two debris counts: 150,000 leaves and 50,000 wood boards, and 350,000 leaves and 150,000 wood boards, where debris were initialized in an 'inner domain' of 400 m x 400 m in the zonal and meridional dimensions. The initial location of the tornado was slightly outside of this inner domain, limiting the amount of debris available for lofting for the first few minutes after tornadogenesis. These two simulations are hereinafter referred to as 'Case I' and 'Case II', respectively. A description of each of the cases in this

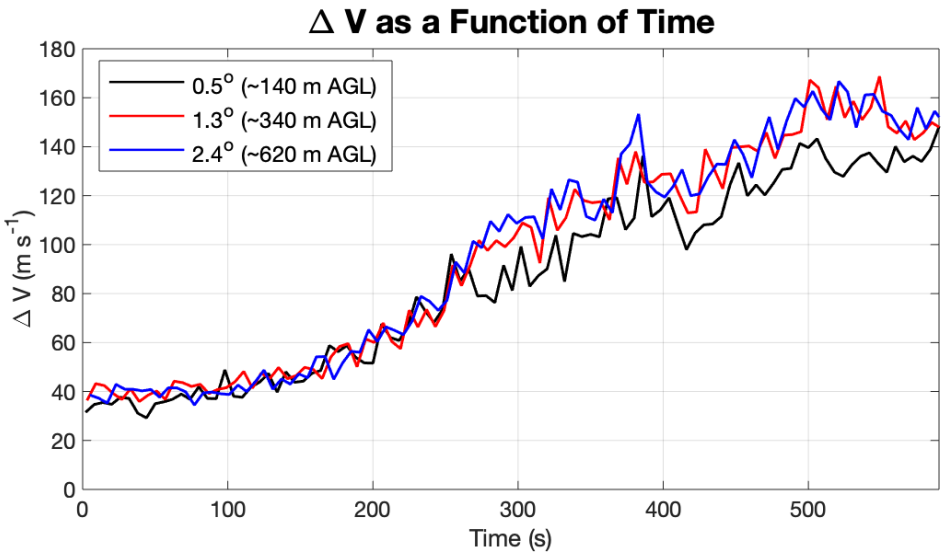

Figure 3.6: An analysis of ΔV near the domain center at 0.5°, 1.3°, and 2.4°. The ΔV is derived for a low-debris case, to minimize debris drag-induced bias. Note that the elevations/heights in this figure do not correspond to the heights listed in Figs. 3.4 and 3.5.

study (i.e., the size of the debris initiation domain and the debris amount) is given in Table 3.1.

These two experiments may be a realistic simulation of a tornado that initially forms over an area with very little loftable debris, and then moves into an area with more debris (e.g., a wooded area, a housing development, etc.). To assess how the debris fields might evolve during tornadogenesis in a region with homogeneous debris availability, the simulations were run again with the initial debris placement spread out over a larger domain (1000 m x 1000 m); these results are discussed in section 3.2.2.3.

Table 3.1: A summary of the five cases run in SimRadar for this study.

Case Number	Debris Initiation Domain Size	Debris Amount
1	400 m x 400 m	150,000 leaves, 50,000 boards
2	400 m x 400 m	350,000 leaves, 150,000 boards
3	1000 m x 1000 m	35,000 leaves, 15,000 boards
4	1000 m x 1000 m	150,000 leaves, 50,000 boards
5	1000 m x 1000 m	350,000 leaves, 150,000 boards

The radar simulation were run for 600 s; tornadogenesis and initial debris lofting occurred ∼150-200 s after the start of the radar simulation. The simulation was initially run at a temporal resolution of 60 s temporal resolution at each PPI. The results from before, during, and after tornadogenesis are shown in Fig. 3.7 for an elevation of 0.5° (approximately 140 m AGL) from Case I. The first time (t = 163 s) occurs shortly before tornadogenesis and subsequent debris lofting, as evidenced by the relatively low Z_H, high ρ_{hv}, and broad rotation and the lack of strong gate-to-gate velocity shear. This is further evidenced by the classification of all pixels in the HCA as either rain or 'big drops'. By the time of the next SimRadar scan at 0.5° (t = 223 s), a noticeable increase in Z_H is present, which is co-located with a decrease in ρ_{hv} and a tightening of the v_r couplet. In the HCA, there is a quasi-circular region of pixels where the HCA has indicated that a TDS is likely present. This is expected, as this appearance of the TDS coincides with all of the 'classic'

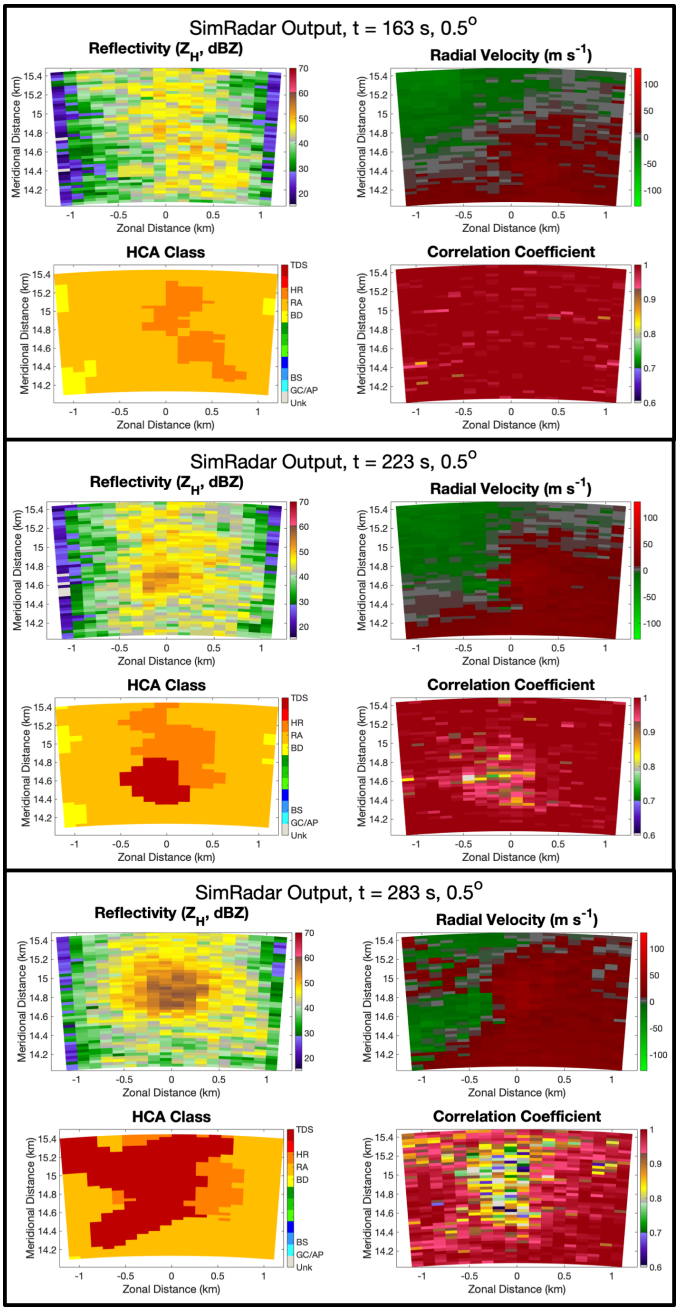

Figure 3.7: SimRadar output at 1-min temporal resolution. Note the significant frame-to-frame increase in Z_H (223 s to 283 s), rotational intensity (163 s to 223 s), and TDS area (163 s to 223 s, and 223 s to 283 s).

signs of a TDS: increased Z_H, lowered ρ_{hv}, and a tightening of the v_r couplet. At the following time (t = 283 s), the TDS area has substantially grown, likely owing to the large area of lowered ρ_{hv} from further debris lofting. It should be noted, however, that the increase in Z_H is still primarily centered around the rotational couplet. We theorize that the large increase in Z_H near the center of rotation is primarily caused by the lofting of wood boards–which require stronger updrafts in order to be lofted–whereas the more widespread lowering of ρ_{hv} is caused mainly by leaves being lofted and dispersed around the tornado since they take longer to fall out due to smaller fall speeds. The stronger correlation between TDS and ρ_{hv} (relative to the correlation between TDS and Z_H) is likely due to the fact that ρ_{hv}, azimuthal shear, and Z_{DR} are weighted more strongly in the TDS class determination than Z_H. Additionally, the x_1 and x_2 values for Z_H in the TDS class are 30 and 35 dBZ, respectively (Snyder and Ryzhkov 2015), such that most of the scan domain contains Z_H values at or above these values.

Upon analyzing Fig. 3.7, it is clear that many significant changes occur regarding the appearance and development of a TDS signature over the course of 1 min, in less than the time of a full NEXRAD volume scan. While many studies on tornadoes have suggested that sub-1-min updates may be necessary to properly observe tornadoes for research purposes, it has not previously been shown whether or not 1-min updates would be sufficient in an operational setting. The results and analysis related to Fig. 3.7 indicate that a TDS could appear on faster timescales than 1 min. As a result of this finding, the temporal resolution of the simulation was

then improved by a factor of 10 at each elevation (6 s), in order to assess whether sub-1-min updates can reveal further information about the evolution of the TDS.

Case I An example of the output at 6 s temporal resolution for Case I is available as supplemental figure Fig. S2 (`arrc.ou.edu/~mahre/FourPanel_6s_150k50k.mp4`). This animation shows the rapid evolution of the TDS in Z_H, v_r, HCA class, and ρ_{hv}. Several frames from this animation are shown in Figs. 3.8 and 3.9, at 0.5° in elevation (left two columns) and at 1.8° in elevation (right two columns). Frames are shown at the full 6-s resolution.

First, the rapid changes at 0.5° in elevation in these figures are analyzed. It is apparent that at 0.5° in elevation, a localized region of lowered ρ_{hv} is not present at the first time (t = 199 s), but becomes increasingly evident over the next several frames. By t = 229 s, this region expands significantly in size, and the lowest ρ_{hv} values become significantly lower. By t = 241 s, there are several pixels with ρ_{hv} less than 0.6, indicating a significant presence of debris. What is particularly surprising is the rate at which the area of lowered ρ_{hv} grows; noticeable, substantial changes are observed in the ρ_{hv} field from one frame to the next. For example, t = 223 s to t = 229 s in Fig. 3.8 shows that the total area of lowered ρ_{hv} has grown significantly, and the magnitude of the lowering of the ρ_{hv} values has increased. This phenomenon of significant changes occurring in 6 s intervals is also observed for the total HCA-identified TDS area (Fig. 3.9). The TDS area–defined as the total area of pixels where a TDS is the most likely class as determined by the HCA–at 0.5°

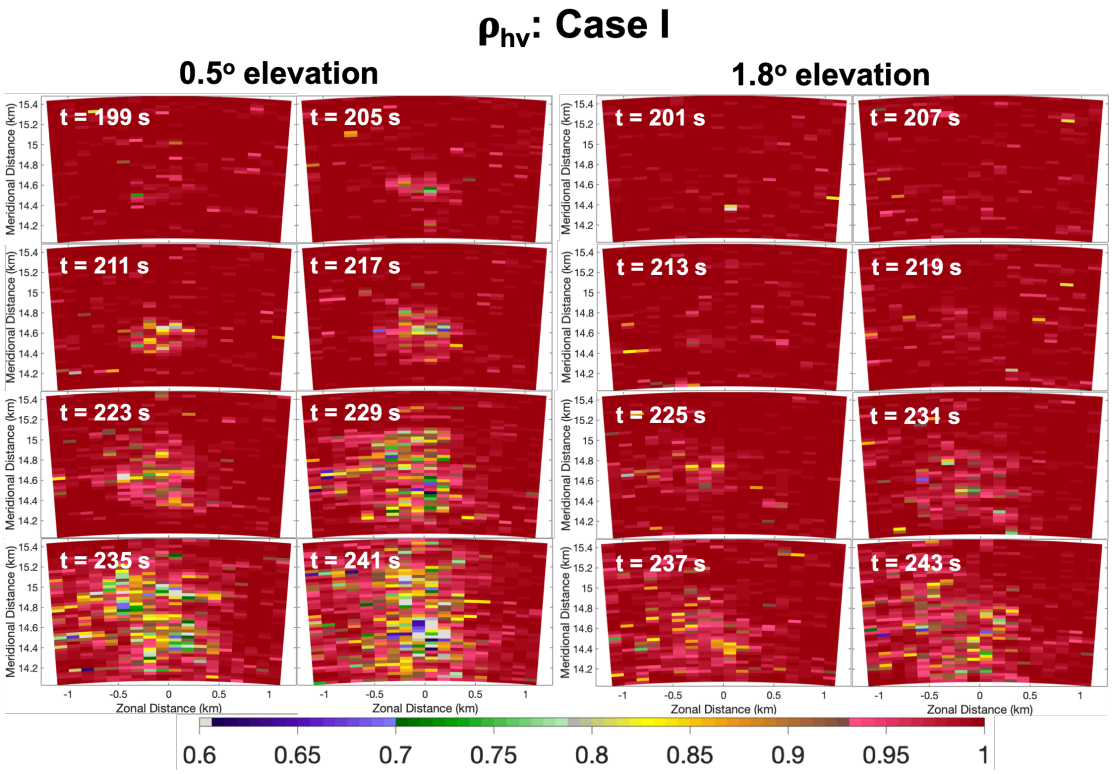

Figure 3.8: SimRadar estimated ρ_{hv} for Case I at 0.5° and 1.8°. The time stagger/offset between 0.5° and 1.8° is due to the time taken to complete the 'rest' of the PPI.

grows from 0 km^2 at t = 199 s to an area of 0.34 km^2 at t = 217 s, to 1.43 km^2 at t = 241 s. The trend in TDS area is plotted for several elevation angles in Fig. 3.10. While the warning issuance decision is more complex than a simple TDS area threshold, the rapid growth of the TDS would seem to indicate that forecasters may significantly benefit from shorter update times than 1 min. This also allows for faster communication to the public about a confirmed tornado producing damage. Additionally, having 6 s scans from a PAR may have other effects on forecasters.

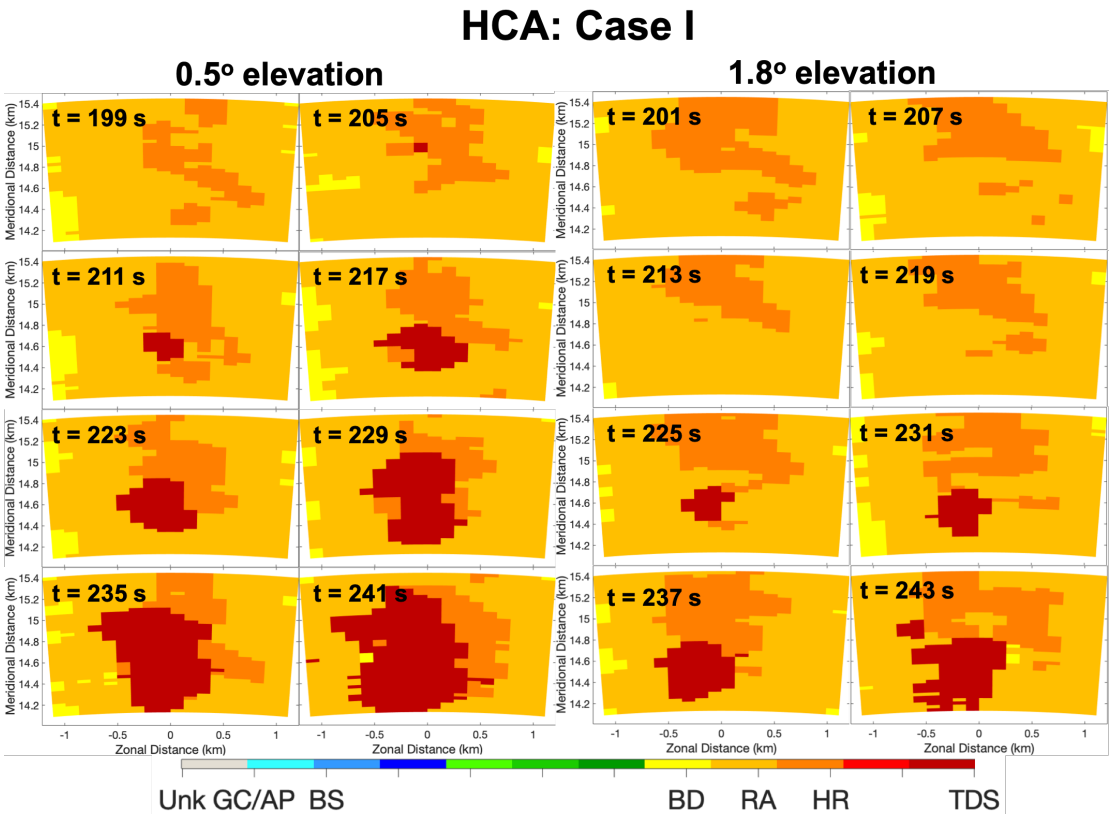

Figure 3.9: As in Fig. 3.8, but for output from the hydrometeor classification algorithm.

For example, having updates every 6 s could ensure that the tornado is detected in near-real time, and seeing consecutive scans with the same features could improve forecaster confidence, rather than having to wonder whether a specific feature is transient and/or an artifact. More specifically, a shorter update time could allow forecasters to see a consistent trend of TDS area increasing with time with a sub-1-min scan, whereas a 60 s or 300 s scan would likely show more discrete jumps in TDS area between scans. Thus, shorter update times could make temporal trends

easier to extract during real-time operations. Furthermore, changes in TDS area could indicate a change in tornado intensity (e.g., Thompson et al. 2017), which could be important information for the messaging that forecasters use to warn the public.

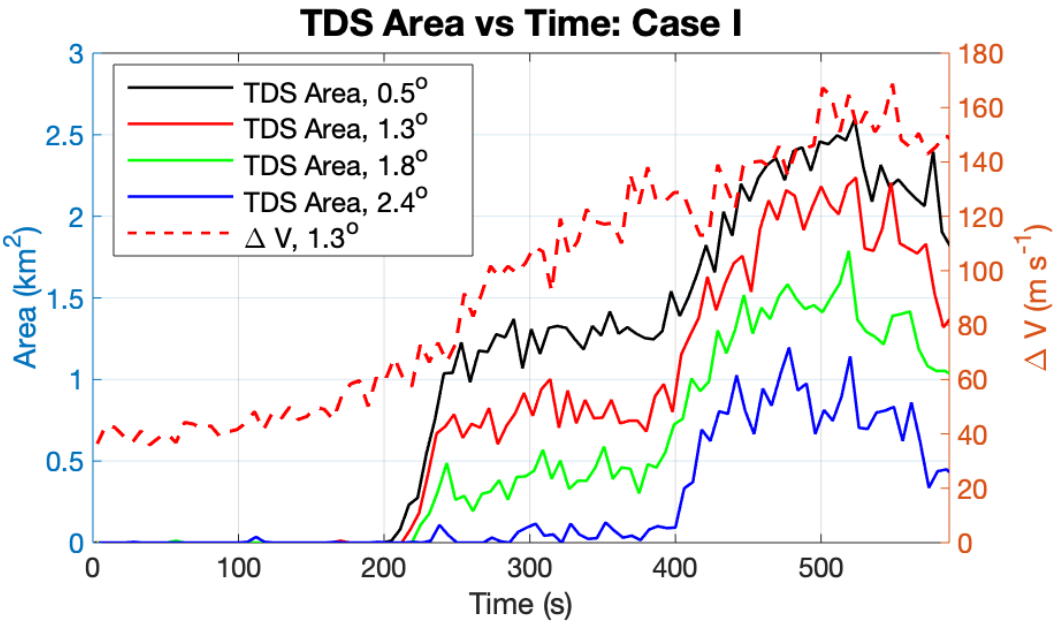

Figure 3.10: A plot of the area of pixels corresponding to a TDS classification at various elevations as a function of time, for Case I. Elevations of TDS area plotted are 0.5°, 1.3°, 1.8°, and 2.4° (approximately 140 m, 340 m, 470 m, and 620 m AGL, respectively). The plotted ΔV is for Case III, such that debris-induced bias of ΔV is minimized. All times are relative to the start of the simulation.

Next, the simulation is analyzed at 1.8° in elevation; this beam height corresponds closer to the lowest height that a radar might observe in/around a tornado at longer stand-off ranges, albeit with better spatial resolution. Analyzing the same

simulation at 1.8° (∼470 m) in Fig. 3.8 and 3.9, it is observed that while the same general trend holds true–that changes in the TDS area occur relatively rapidly–the changes in the ρ_{hv} field are more subtle. There is a ∼20 s delay in the initial appearance of lowered ρ_{hv} at 1.8° in elevation, compared to 0.5° in elevation. Additionally, the lowered ρ_{hv} region appears to be more spread out and diffuse at 1.8° (i.e., at t = 243 s) compared to 0.5°. This is likely due to the fact that debris are initially generated and lofted in a relatively small region around the tornado center. As the debris are lofted, the debris disperses radially outward due to centrifuging, leading to a lower number of pieces of debris per radar pixel, even if the same total amount of debris reaches that level. Additionally, some debris is prone to 'falling out' before reaching these higher elevations (Dowell et al. 2005; Bodine et al. 2014) and thus debris concentrations are lower. This is consistent with the TDS observed at 1.8° (Fig. 3.10). From t = 250 s to t = 400 s, the TDS area at 0.5° holds relatively steady around 1.25 km^2, and the TDS area at 1.8° is relatively constant at ∼0.4 km^2. After t = 400 s, the TDS area for the 0.5° scan peaks at just above 2.5 km^2 while the maximum TDS area at 1.8° is ∼1.75 km^2; for reference, the maximum possible TDS area (based on the size of the scan domain) is approximately 3.5 km^2. Thus, it can be said that the total TDS 'footprint' is diminished at higher elevations, which could possibly make tornado detection based on TDS difficult to predict, especially in real-world scenarios where debris lofting is more transient, and the debris count is constantly changing. These types of cases become more common as the range from the radar to the tornado increases, and low-level radar coverage is reduced.

After t = 400 s, significant, sustained debris lofting is observed at even higher elevations, such as 2.4° (∼620 m AGL) and 3.1° (not shown). It should be noted that the beam height at 3.1° is at ∼800 m AGL, which is above the top of the model wind field input into SimRadar. As a result, the TDS area values at 3.1° in elevation may not be fully representative of the expected lofting at these levels, and debris lofting will generally not extend beyond 700 m AGL, and as such the TDS will not reach the same heights as observed in real-world cases (e.g., Van Den Broeke and Jauernic 2014). As a result, no in-depth analysis is conducted at 3.1° and above in this study.

One note is that in many of the frames of Fig. 3.9, the outer radials at each time tend to indicate the presence of 'big drops'. It is believed that this is simply an artifact of the domain size; the domain extends to -1 km to +1 km in the zonal dimension, such that most returns along the outer radials are from the outer portions of the radar beam, causing anomalously low Z_H because of the lack of scatterers in much of the radar beam. It is believed that this artifact does not adversely affect the results and conclusions herein. Another artifact that appears in Fig. 3.10 is the downward trend in TDS area at all elevations between t = ∼525 s and the end of the simulation (600 s). The cause for this is believed to be somewhat artificial; the center of circulation moves toward the east during this time, away from the center of the scan domain (see Fig. S2). As a result, much of the debris is 'ejected' out of the scan domain while circulating the tornado, causing an artificial lowering in TDS area.

Case II Some results from Case II are shown in Figs. 3.11 and 3.12. Interestingly, the debris lofting begins at nearly the exact same time as in Case I; the increased debris count does not cause the TDS to appear earlier than before. However, as seen in the simulations with larger debris initiation domains (Cases III to V, in section 3.2.2.3), this result may not be robust.

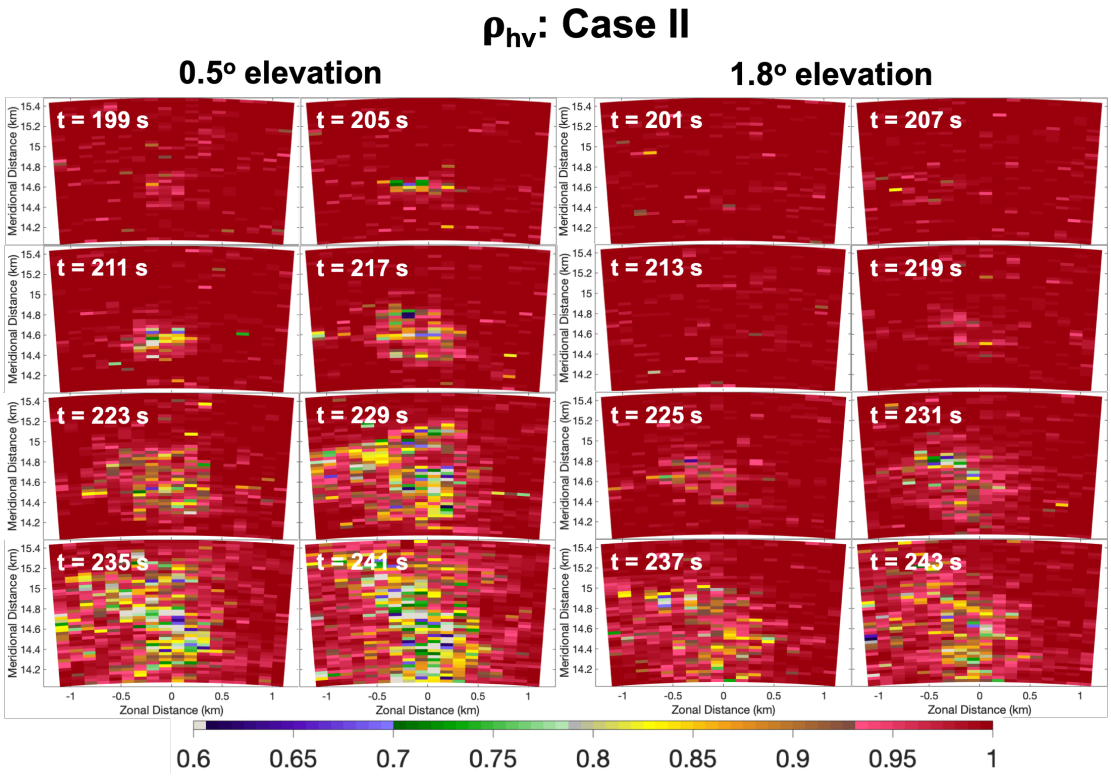

Figure 3.11: SimRadar estimated ρ_{hv} for Case II at 0.5° and 1.8°. The time stagger/offset between 0.5° and 1.8° is due to the time taken to complete the 'rest' of the PPI.

The qualitative results remain largely the same with Case II as with Case I; the area of lowered ρ_{hv} appears to grow in a similar manner in Fig. 3.11 as in Fig. 3.8.

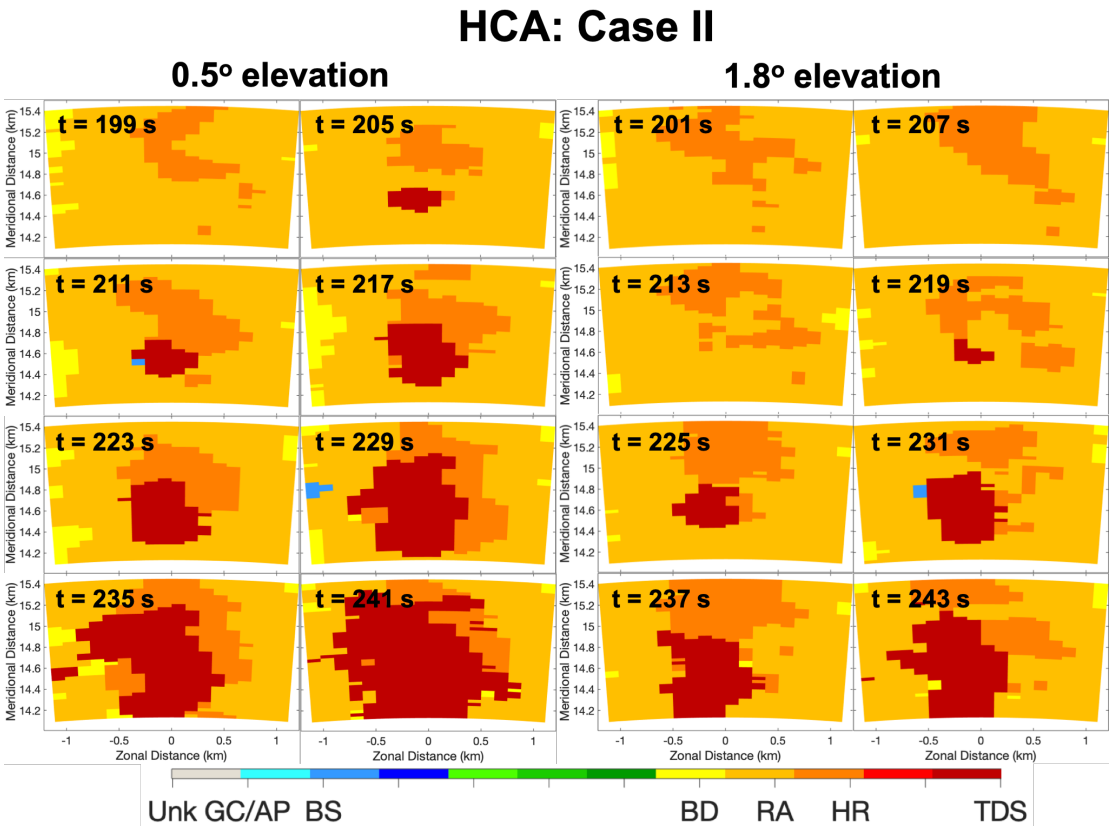

Figure 3.12: As in Fig. 3.11, but for output from the hydrometeor classification algorithm.

Additionally, the results of the HCA in Fig. 3.12 appear largely unchanged from those of Fig. 3.9. The area identified as a TDS grows similarly to Case I, but in analyzing Fig. 3.13, the 'plateau' of TDS area between 250 s and 400 s at 0.5° is higher for Case II than Case I (∼1.75 km^2 compared to 1.25 km^2). Additionally, the TDS area for 0.5°, 1.3°, and 1.8° reaches ∼2.75 km^2 at a time of ∼500 s, indicating that nearly the entire scan domain is 'saturated' with debris at these

levels. This would indicate that the 'true' TDS area is likely higher than what SimRadar observes, due to the size of the scan and simulation domains.

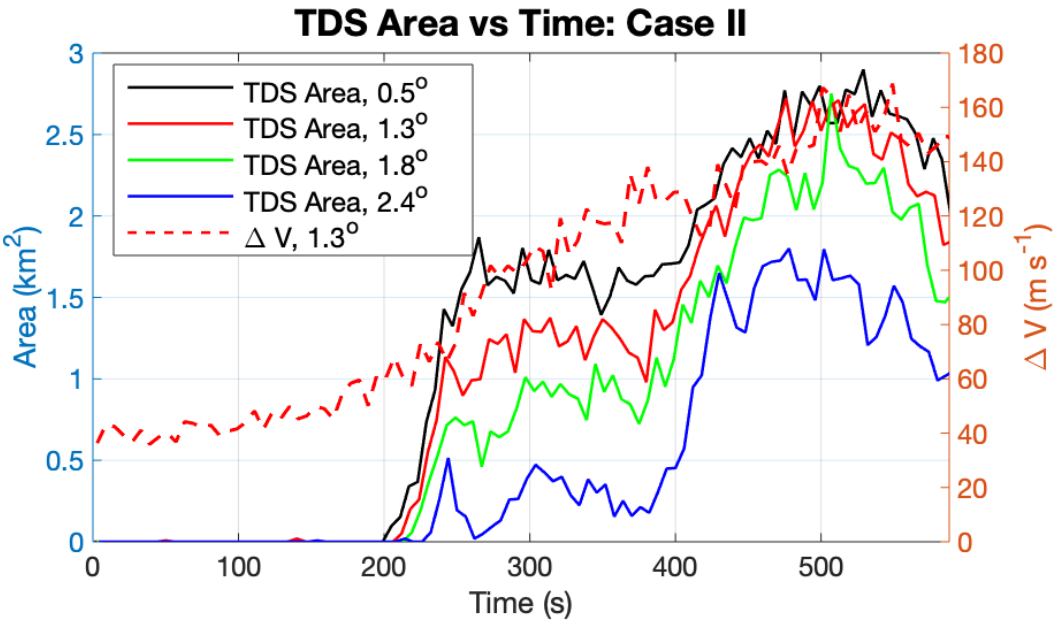

Figure 3.13: As in Fig. 3.10, but for Case II. The plotted ΔV is for Case III such that debris-induced bias of ΔV is minimized.

In multiple frames of Fig. 3.12, the HCA predicts biological scatterers (BS) as the scatterer type. In SimRadar, no biological scatterers are present, meaning that this is a misidentification. The most heavily weighted variables in determining the BS class are ρ_{hv}, and standard deviation of Z_H and Φ_{DP}. The membership function for ρ_{hv} is maximized for ρ_{hv} values between 0.5 and 0.8, and an inhomogeneous spatial texture for Z_H and Φ_{DP} distinguishes the BS class from the analyzed hydrometeor classes. Because the misidentification of the BS class primarily appears at the periphery of the TDS region (i.e., t = 211 s and t = 231 s in Fig. 3.12), it is theorized

that the high spatial variance of Z_H and Φ_{DP} causes the spurious identification of biological scatterers.

After Cases I and II were run, a major question posed by the data was why the TDS area has a 'plateau' between t = 250 s and t = 400 s, when the tornado strength appears to generally increase in a nearly linear fashion from t = 150 s to t $\sim$ 550 s. Once the simulations were analyzed in the visualization software (e.g., Fig. S1), it was clear that the tornado formed on the periphery of the small debris initiation domain (400 m by 400 m). Thus, the initial debris lofting may be delayed. Furthermore, the tornado eventually moved into the center of the small debris initiation domain, which appears to correspond with the increase in TDS area between t = 400 s and t = 450 s in Figs. 3.10 and 3.13. As a result, it was determined that many of the changes in TDS area in Cases I and II are an artifact of the size of the debris initiation domain, rather than being purely caused by changes in the tornado strength; the total TDS area calculated is likely a function both of tornado strength and of debris availability. Again, this phenomenon could occur in real-world data in a situation where debris availability changes, such as when a tornado moves into an area with more available debris, such as a wooded area or a housing development. Therefore, it was decided to run the simulations again with a larger (1 km x 1 km) debris initiation domain (Cases III–V); Fig. S1 shows a visualization for this 1 km x 1 km debris initiation domain. The results from the HCA output and the ρ_{hv} field for the three simulations are shown in section 3.2.2.3.

3.2.2.3 High-Resolution Observations of TDS Growth: Large Debris Initiation Domain

Case III The results from Case III are shown in Figs. 3.14 and 3.15. As is evident in the ρ_{hv} field for the 0.5° elevation scan, a lowering in ρ_{hv} begins at roughly t = 175 s, and becomes more pronounced at t = 193 s. The initial lowering of ρ_{hv} at t = 175 s corresponds with w exceeding 20 m s^{-1} and ΔV reaching 50–55 m s^{-1} (Figs. 3.4 and 3.6). Debris lofting coinciding with ΔV reaching 50–55 m s^{-1} is consistent with previous studies that have used 55 m s^{-1} as a threshold for tornadogenesis (e.g., Houser et al. 2015). Between t = 193 s and t = 211 s, the magnitude of the ρ_{hv} decrease is more pronounced in a region to the southwest of the domain center. This generally corresponds to an increase in the total TDS area at these times, where the location of the TDS region corresponds closely with the lowered ρ_{hv} region. Approximately 4 min after the beginning of the lowering of ρ_{hv} and the increase in TDS area, an initial lowering in ρ_{hv} is evident at 1.8° in elevation. However, the lowering is significantly more diffuse than at 0.5° in elevation, and the magnitude of ρ_{hv} lowering is not as large. As stated in Cases I and II, this is likely due to a difference in the debris types contributing to the lowered ρ_{hv} and the appearance of a TDS area, as well as a difference in the density of scatterers at the given elevation. More diffuse scatterers would imply that even for a constant debris count, the ratio of debris to hydrometeors in the resolution volume would be reduced, thus causing a less substantial lowering in ρ_{hv} (Bodine et al. 2014, 2016b).

The TDS area in Fig. 3.15 at 1.8° appears to be more transient and less consistent than that at 0.5°. These types of transient features are better-suited for detection by a rapid-scan system.

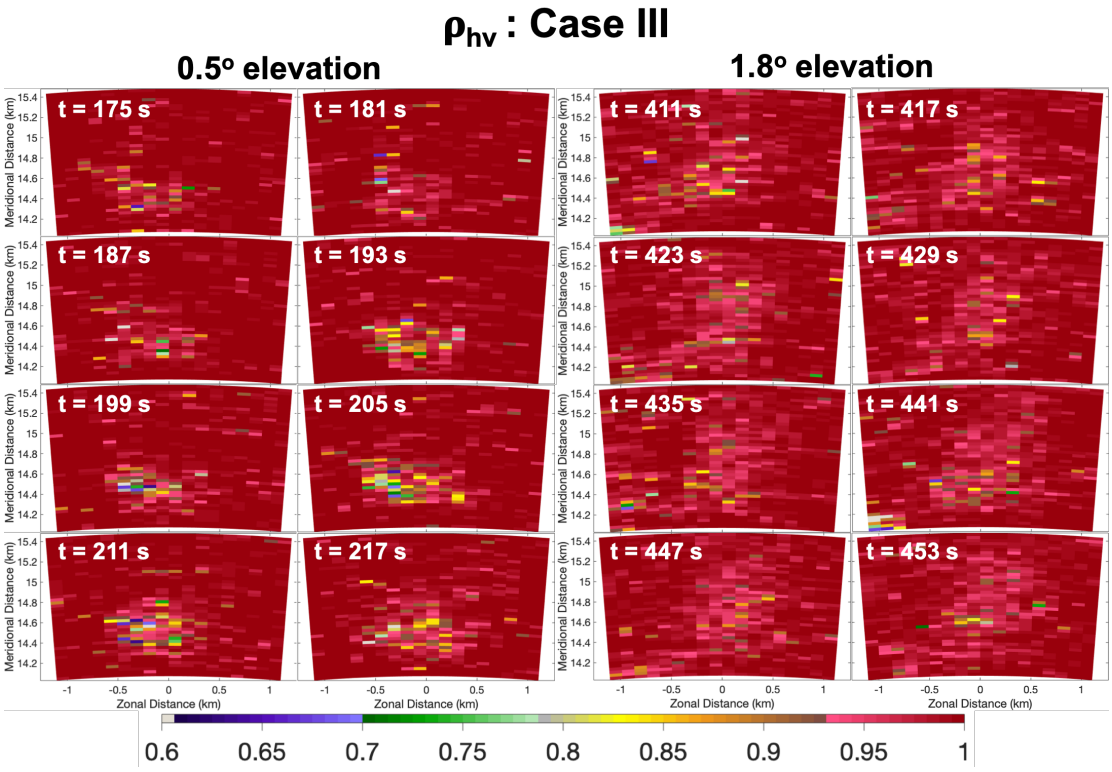

Figure 3.14: SimRadar estimated ρ_{hv} for Case III at 0.5° and 1.8°. The time difference between the 0.5° and 1.8° scans is due to the delay in debris lofting between subsequent levels.

One note is the difference in times between the times in the 0.5° scans and the 1.8° scans. In Cases I and II, the time between the appearance of a TDS at successive elevation angles is decreased. This is likely due to the lower effective debris concentration; when the debris are confined to a smaller initiation domain,

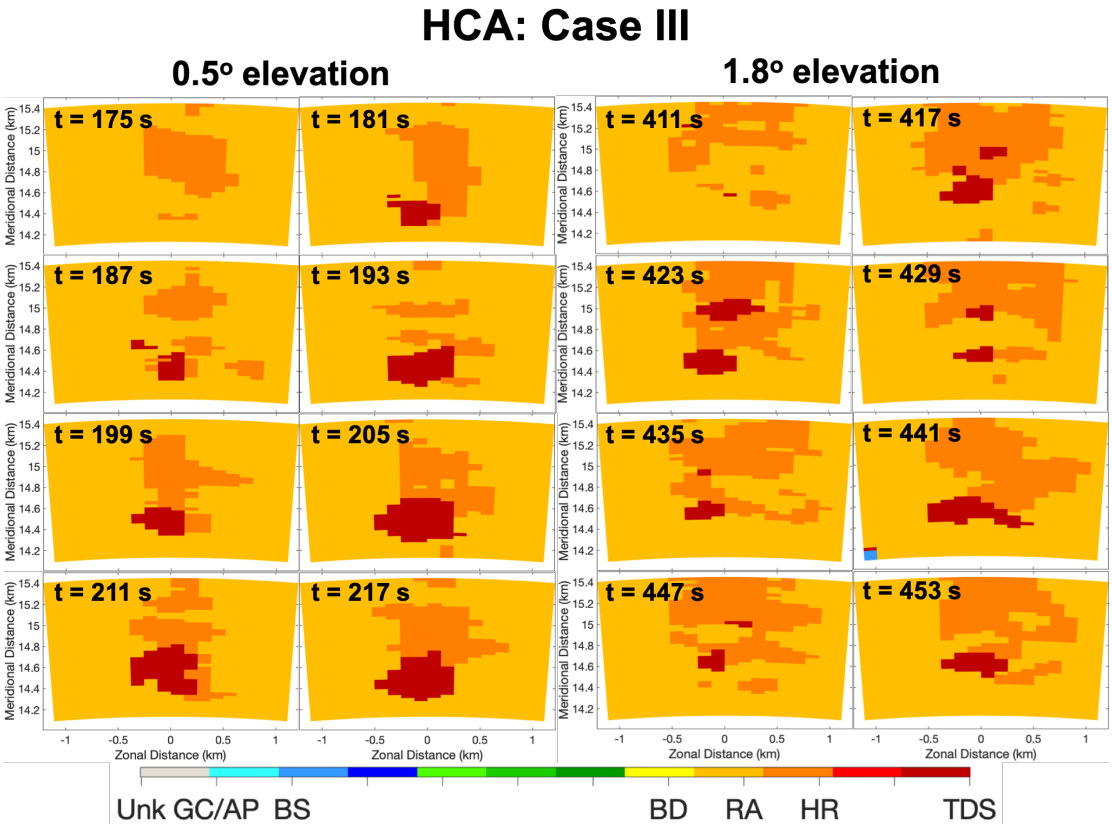

Figure 3.15: As in Fig. 3.14, but for output from the hydrometeor classification algorithm.

the number of pieces of debris per unit area increases. When the initiation domain is expanded from 0.16 km^2 to 1 km^2, the number of pieces of debris per unit area decreases by roughly a factor of six. For a fixed updraft area, this means that effectively, the number of pieces of debris that are 'loftable' is reduced by a factor of six.

From analyzing Fig. 3.16, it is possible to estimate the rate of increase in the total TDS area in the scan domain. For instance, at 0.5°, the total TDS area increases

from 0 km^2 at t = 175 s to approximately 1.4 km^2 at t $\sim$ 525 s. This represents an increase of approximately 4000 m^2 s^{-1} in the total TDS area. At higher elevations such as 1.3°, this increase is slower, by roughly a factor of two. This would imply that at lower heights AGL, the onset of a TDS is more sudden, likely due to the relative sparseness of debris after significant lofting has occurred. In general, the total TDS area tends to decrease with height, despite a similar TVS at 1.3° and 2.4°, both of which appear stronger than the TVS at 0.5° (Fig. 3.6). This suggests that the amount of debris lofted tends to decrease with height, likely due to debris fallout.

In Case III, the TDS area appears to directly correlate with the strength of the tornado as measured by ΔV (Fig. 3.16). The radar-measured ΔV in Fig. 3.16 first reaches 50 m s^{-1} at t = 170 s. It is around this time that an increase in w is first observed in Figs. 3.4 and 3.5. The sudden increase in ΔV and in w would seem to indicate tornadogenesis; this is consistent with the ΔV value of 55 m s^{-1} found in Houser et al. (2015). Thus, it is not surprising that initial debris lofting is observed at 0.5° in elevation at t = 181 s. A TDS signature at 1.3° in elevation ($\sim$200 m higher) initially appears about 75 s later, which would indicate that the upper end of the lofted debris cloud is 'moving' upward at approximately 3 m s^{-1} in this layer. The TDS area continues to grow at 0.5°, 1.3°, and 1.8° until approximately t = 550 s. Between t = 550 s and t = 600 s, both the TDS area and ΔV are reduced. This agreement between TDS area and ΔV appears to be more natural–and less prone to artifacts of the tornado moving relative to the initial debris placement–than the

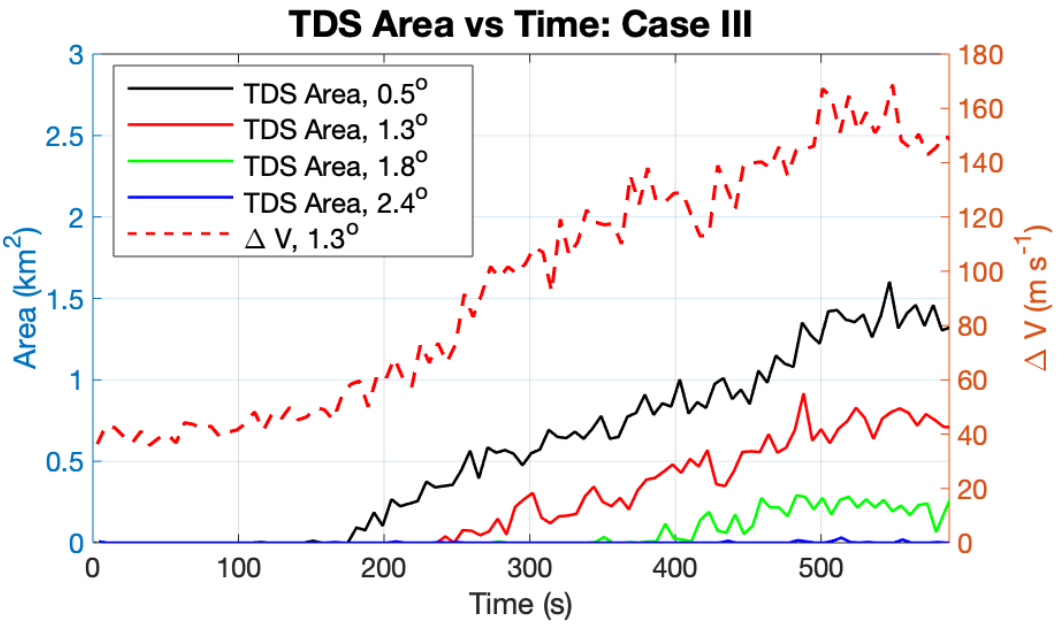

Figure 3.16: A plot of the area of pixels corresponding to a TDS classification at various elevations as a function of time, for Case III. Elevations of TDS area plotted are 0.5°, 1.3°, 1.8°, and 2.4° (approximately 140 m, 340 m, 470 m, and 620 m AGL, respectively). All times are relative to the start of the simulation.

simulations in section 3.2.2.2. This indicates that debris availability may impact this correlation, although cases with both a small and large debris initiation domain show the same general trend.

Case IV In Fig. 3.17 and Fig. 3.18, the ρ_{hv} and HCA output from Case IV is shown at 0.5° and 1.8°. Compared to Figs. 3.14 and 3.15, the times at which initial lofting is observed (both by ρ_{hv} lowering and a detection in the HCA) are earlier. This is likely due to the higher debris concentration, such that the increased amount

of debris that is lofted by the tornado and its updraft causes the TDS signature to be present earlier. As with Case III, the increase in TDS area at 0.5° appears to be more steady and confined to a single area of the scan domain, whereas the TDS area at 1.8° appears to be more sporadic, with larger fluctuations. The sporadic nature of the HCA-indicated TDS area at 1.8° could lead to reduced forecaster confidence; thus, having several scans could assure forecasters of the general trend, and whether or not a TDS is forming at this height. This would be especially helpful in cases where lower-level data is not available due to longer ranges between the radar and the tornado, and this further reinforces the advantage of having sub-1-min updates for operational purposes.

As in Case III, the initial appearance of lowered ρ_{hv} and a positive TDS detection occurs to the southwest of the domain center. This could imply that the updraft area is highly localized, and that only debris in a certain region is lofted. The location of the region of lowered ρ_{hv} in Fig. 3.17 is consistent with that in Fig. 3.14 at 0.5°. At 1.8°, the same pattern holds true for that in Case III: the lowered ρ_{hv} is diffuse, and the magnitude of lowered ρ_{hv} is not as large. Additionally, the area in the HCA that indicates a TDS is once again 'split' into a northern and a southern area (e.g., t = 297 s, t = 315 s, and t = 327 s in Fig. 3.19). This could be caused the two-cell nature of the tornado (i.e., multiple updrafts inducing lofting), but further analysis would be needed to support this hypothesis.

In Fig. 3.19, we can again analyze the rate at which the TDS area grows at various elevation scans. At the 0.5° scan, the rate of increase in Case IV is greater

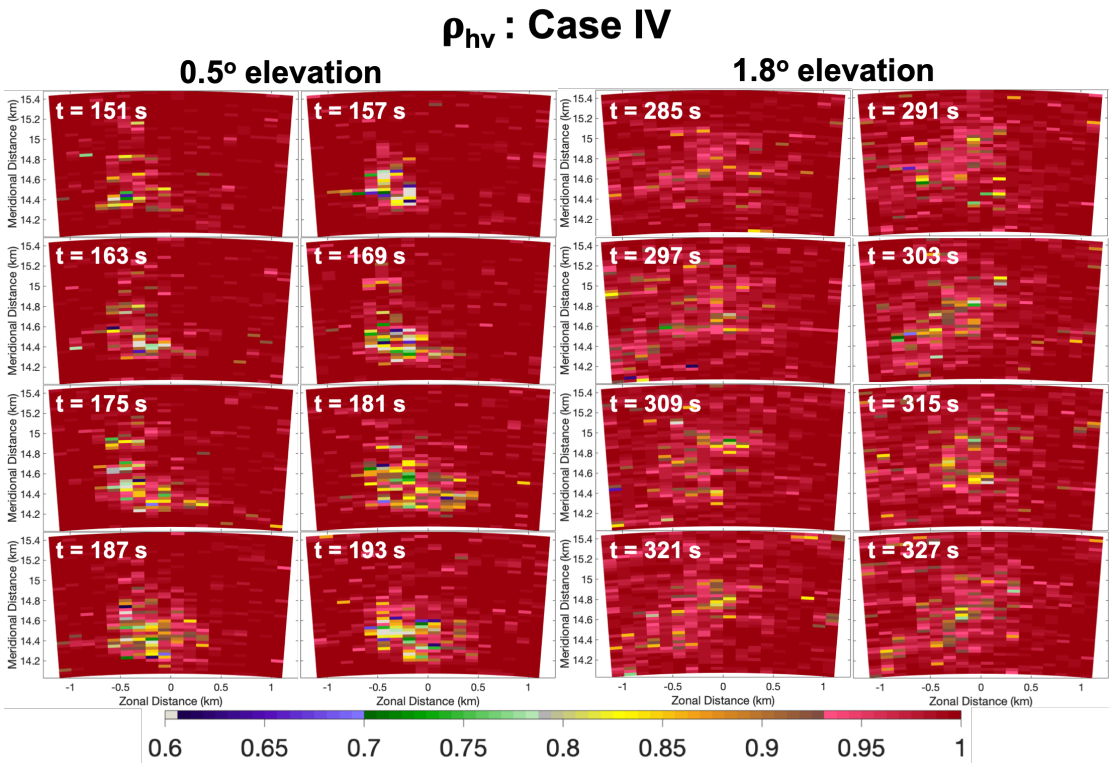

Figure 3.17: SimRadar estimated ρ_{hv} for Case IV at 0.5° and 1.8°. The time difference between the 0.5° and 1.8° scans is due to the delay in debris lofting between subsequent levels.

than that of the Case III. The TDS area is 0 km^2 at t $\sim$ 150 s, and increases to slightly greater than 2 km^2 at t $\sim$ 500 s. This corresponds to a growth rate of $\sim$6000 m^2 s^{-1}, which is approximately 50% faster than that of Case III. This result is in contrast to those in Cases I and II, where the debris count is not found to have an effect on the rate at which the TDS grows. The hypothesis is that at a certain debris concentration (i.e., debris per unit area), the lowest levels of the scan domain become 'saturated' with debris, such that an increase in debris count

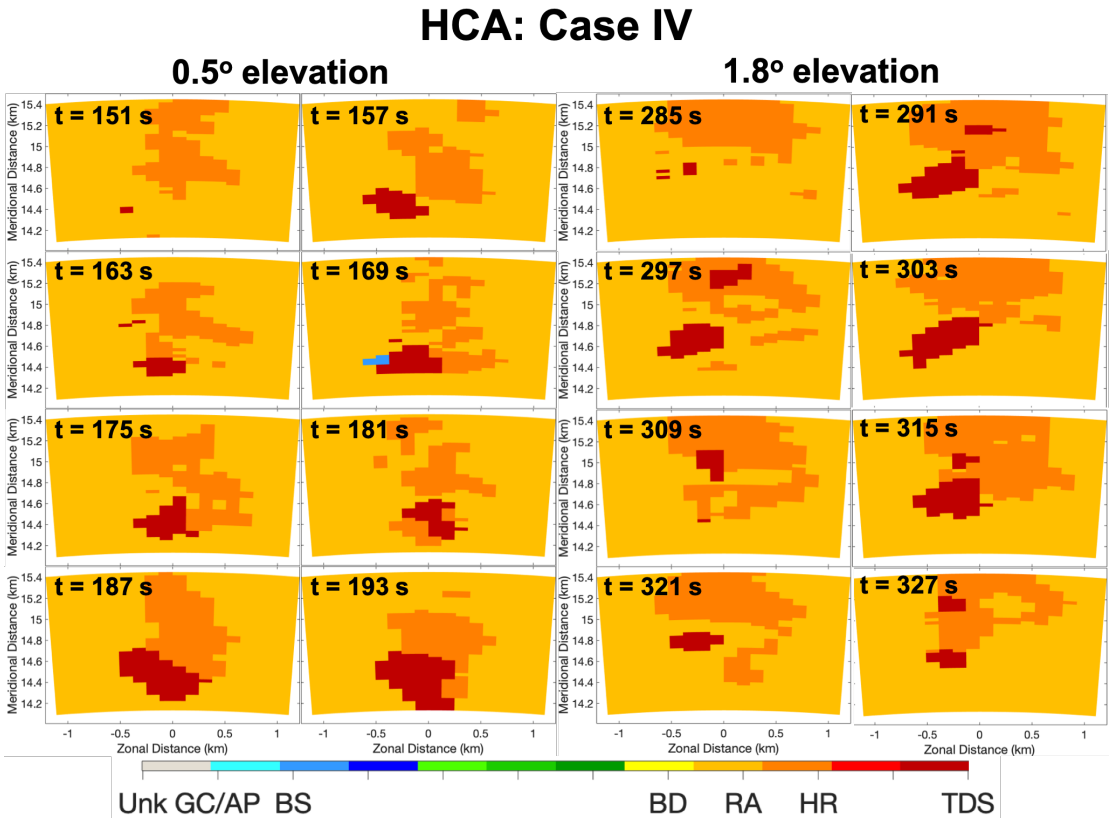

Figure 3.18: As in Fig. 3.17, but for output from the hydrometeor classification algorithm.

does not change the rate at which the TDS area grows. Additionally, the changes in availability of debris may play a larger role in the TDS area in cases I and II. For the larger domain cases (Cases III–V), it is possible that the lower levels (such as at 0.5°) have not yet become saturated with debris because of the lower debris concentration (i.e., the same number of pieces of debris is spread out over a larger area).

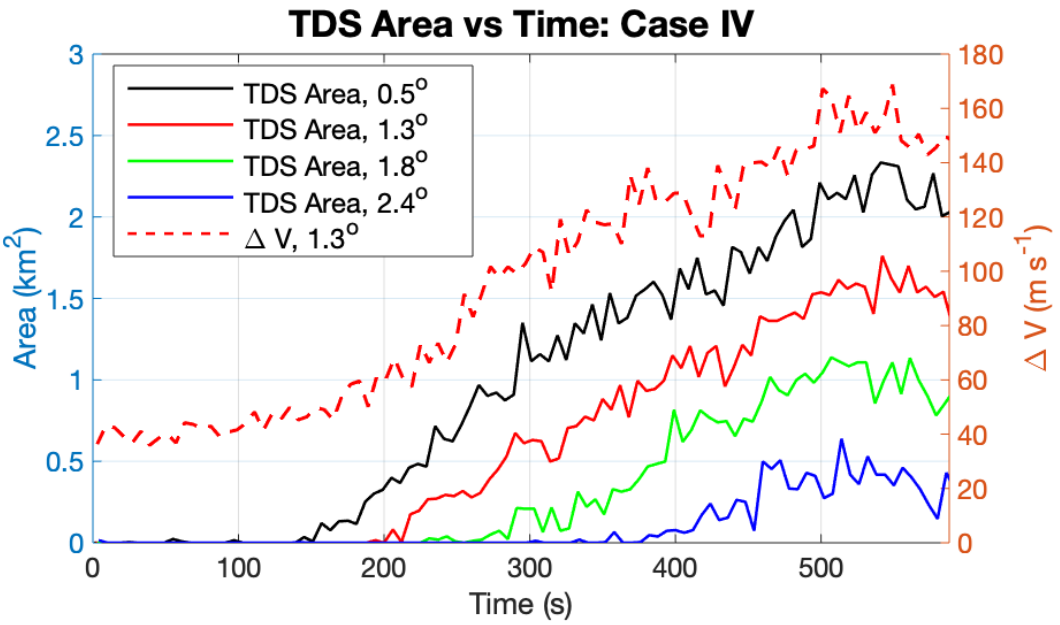

Figure 3.19: As in Fig. 3.16, but for Case IV. The plotted ΔV is for case III such that debris-induced bias of ΔV is minimized.

Case V Finally, the simulation is run at a high debris concentration for the large debris initiation domain (Case V); the ρ_{hv} output is shown in Fig. 3.20, and the HCA output is shown in Fig. 3.21. In general, the output shown in these two figures is qualitatively similar to that in the output figures of Cases III and IV. A closer analysis, however, reveals two interesting conclusions. First, the increased debris count does not change the initial time at which debris are lofted to 0.5° (140 m AGL). However, the increased debris count does reduce the time from the start of the simulation to the time at which a TDS is detected at 1.8° in elevation. Since less debris reaches higher altitudes in tornadoes, having more debris lofted may aid in producing a TDS at an earlier time. Second, the rate at which the

TDS area grows continues to increase. An estimate of the rate at which TDS area increases at the 0.5° scan (Fig. 3.22) indicates that the TDS area increases at a rate of approximately 10000 m^2 s^{-1}. This is ∼2.5 times faster than that of Case III, and ∼1.67 times faster than that of Case IV.

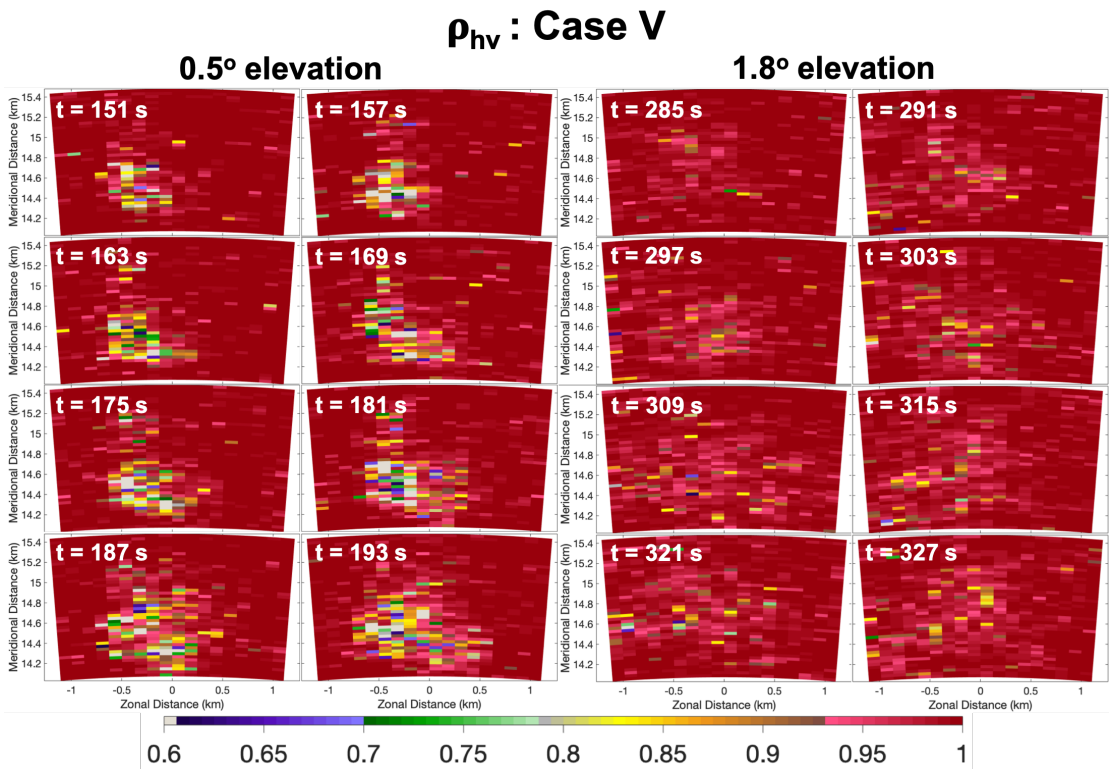

Figure 3.20: SimRadar estimated ρ_{hv} for Case V at 0.5° and 1.8°. The time difference between the 0.5° and 1.8° scans is due to the delay in debris lofting between subsequent levels.

A limitation of the simulations herein is that debris are placed near the ground from the beginning of the simulation. When an updraft forms prior to the tornado, this can cause debris to be lofted (especially lighter debris), when this debris may

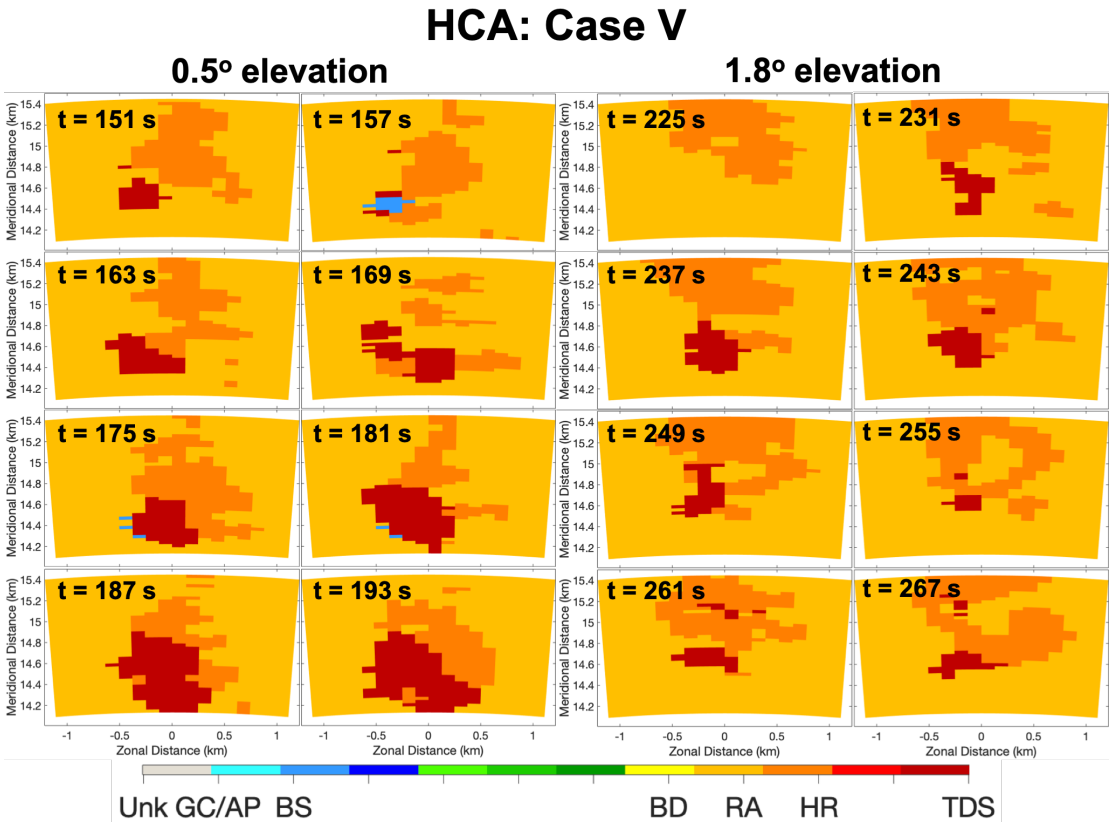

Figure 3.21: As in Fig. 3.20, but for output from the hydrometeor classification algorithm.

not be loose in a real-world scenario. A solution to this problem is the ability to create debris as a function of wind speed, where regions of higher wind speed would generate more debris. Initial implementation of this method has recently been completed on SimRadar; it is believed that this would offer significant benefit for enhancing the realism of these simulations going forward.

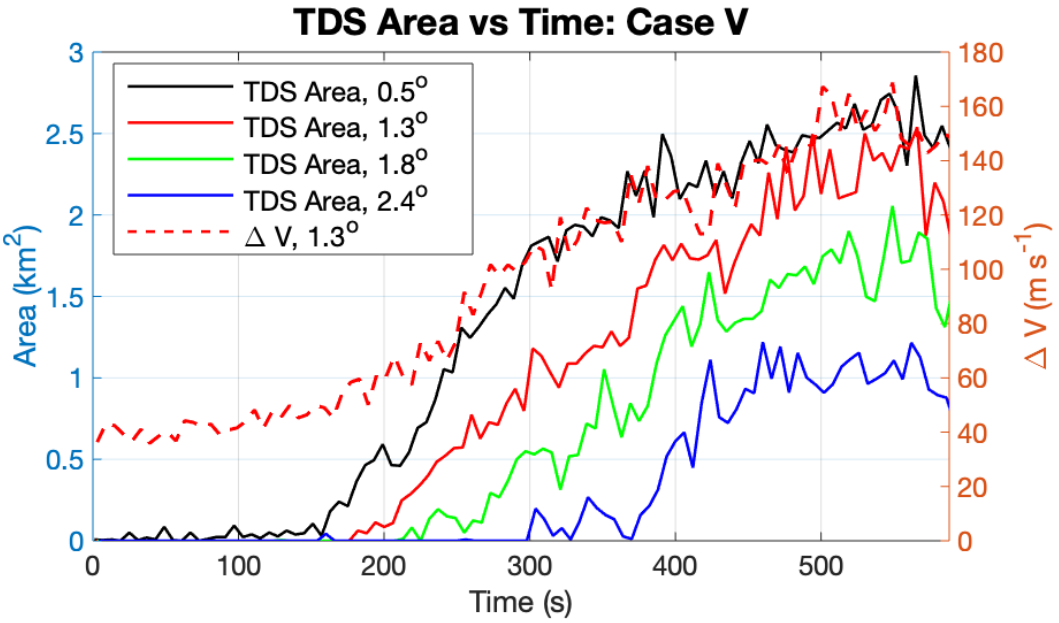

Figure 3.22: As in Fig. 3.16, but for Case V. The plotted ΔV is for case III such that debris-induced bias of ΔV is minimized.

3.3 Estimating Tornado Detection Latency Time

The second goal of this study is to quantify the changes in tornado detection using an objective algorithm, using this as a proxy for forecaster-based subjective tornado detection. To assess this, an objective method for tornado detection is created, and SimRadar (described in section 3.2.1.1) is used. While this clearly does not supplant the need for a human forecaster to issue warnings based on subjective criteria, it does provide a metric to directly compare the changes in tornado warning lead time (referred to as 'tornado detection latency time' herein) from multiple scenarios. The advantage of an objective warning metric for testing is the ability to

re-run simulations multiple times and directly assess the impact of variables on the objectively issued warning performance.

3.3.1 Methods

3.3.1.1 Large-Eddy Simulation (LES)

To assess the second goal of this study (i.e., assessing the difference in tornado detection latency time), an LES is used as the model wind field. The LES is a relatively steady-state tornado, which does not significantly change in intensity with time. The LES is run on a stretched grid, such that spatial resolution is finest at the center of the analysis domain, and becomes coarser when moving outward from the center. Horizontal grid spacing varies between 2.8 m and 16.8 m, while vertical grid spacing varies between 2.8 m and 98 m, with the slowest rate of grid stretching occurring within the radius of maximum winds, which is ∼200 m (Bodine et al. 2016a). The simulation in section 3.3 is 3000 s long, which is longer than the length of the LES wind table. When the end of the LES table is reached, the model wind field from the LES starts over from the beginning. Because the LES simulates a near-steady state tornado (as opposed to the tornadogenesis simulation of CM1), this is not believed to adversely affect the results. The reader is referred to Maruyama (2011) and Bodine et al. (2016a) for more information about the LES.

To artificially create a change in the debris present in the simulated radar return with time, a debris 'RCS ramp-up' is used. Using this method, debris are initially

released into the tornado, and are allowed to advect freely. The RCS is set to zero at the initial time, and is then linearly increased to the 'true' value over an extended period of time. This does not necessarily reflect an accurate depiction of tornadogenesis or the debris lofting process. However, this method is somewhat similar to what one would expect to see if a mature tornado passed from a region with minimal debris sources to a region where debris such as leaves and wood boards are more plentiful and readily lofted.

For the purposes of this portion of the study, the debris contributions within SimRadar change with time in order to assess the TDS latency time. This is achieved by linearly increasing the debris RCS as follows:

$$\begin{aligned} \sigma &= 0, \quad t < t_0 \\ \sigma &= \frac{(t - t_0)\sigma_0}{t_1 - t_0}, \quad t_0 \leq t < t_1 \\ \sigma &= \sigma_0, \quad t \geq t_1 \end{aligned} \tag{3.2}$$

Here, σ is the simulated debris RCS, σ_0 is the 'true' debris RCS, t_0 is the time at which the tornado begins to loft debris, and t_1 is the time after which the tornado does not loft additional debris. This is done to simulate the lofting of debris by a mature, violent tornado as it passes over a debris source. Using this method, the contribution of debris to the overall radar-derived variables will increase over time. In this portion of the study, the total ramp-up time (t_1 minus t_0) is 1000 s. This represents a significantly longer ramp-up time than that of the CM1 model, and could be more representative of a case where the amount of debris lofting is changing more slowly with time.

3.3.1.2 Tornado Detection Latency Time Calculation

One of the goals for this study is to test the performance of a simulated rapid-scan weather radar, compared to expected performance of the current NEXRAD system under similar conditions. In simulating a rapid-scan radar, the goal of this portion of the study is to test scanning strategies with update time and data quality metrics which would meet or exceed the requirements of a notional NexPAR system.

To quantify the benefits of rapid-scan weather radar, TDS latency times are computed/simulated for a variety of cases within SimRadar. For this portion of the study, the debris is 'released' into the tornado over a prescribed period of time; in this case, a ramp-up time of 1000 s is used. Here, latency time for a TDS is defined as the lag between the time at which RCS ramp-up begins and the time at which the threshold for a TDS is reached. Each pixel in a PPI is analyzed for the necessary TDS criteria: horizontal reflectivity factor above 40 dBZ ($Z_H > 40$ dBZ), copolar correlation coefficient below 0.825 ($\rho_{hv} < 0.825$), and proximal location to a velocity couplet with minimum ΔV of 60 m s^{-1}. Unlike the first experiment in this study–where an HCA is used–this portion of the study uses a binary determination of the presence of a TDS at each pixel. It is believed that while this changes the total area categorized as a TDS, the final results and conclusions should not change. The scanning strategy for the simulations uses 25 pulses per radial, a beamwidth of 1°, and a range resolution of 30 m.

These TDS thresholds are similar to those used in past observational studies (Bodine et al. 2013; Kurdzo et al. 2015a), and are evaluated at each elevation angle for each VCP tested, such that latency time can be analyzed as a function of both height and VCP update time. A positive detection of a TDS at a given elevation is defined as the first time at which the area of pixels meeting the TDS criteria exceeds some area threshold, where area is calculated by summing all of the pixels where the TDS criteria have been met. For example, if an area threshold is set at 50,000 m^2, the difference between the time of the first scan at which the area of pixels meeting the TDS criteria exceeds 50,000 m^2 and the time at which RCS ramp-up began is recorded as the TDS latency time for that VCP. To minimize the sensitivity of the results to a particular threshold, a large range of TDS area thresholds are used, in a range of nearly continuous values. For the realizations with a lower debris count, TDS area thresholds between 10,000 m^2 and 30,000 m^2 are used, in 100 m^2 increments. In higher-debris cases, TDS area thresholds between 10,000 m^2 and 150,000 m^2 in 100 m^2 increments are used. The difference in upper bounds accounts for the difference in observed TDS areas when lower and higher debris counts are lofted.

In theory, if there are no fluctuations or variations in TDS area with time, the difference in TDS latency time between two VCPs should be equal to the difference in VCP update times divided by two. The tornado detection time for any given VCP should be uniformly distributed between 0 s and N s, where N is the volumetric update time in seconds. Therefore, the mean update time for VCP 'A' is $\frac{N_A}{2}$ s,

and the mean update time for VCP 'B' is $\frac{N_B}{2}$ s, where VCPs A and B update at N_A s and N_B s, respectively. Therefore, the expected (theoretical) difference in TDS latency time is equal to $\frac{N_A - N_B}{2}$. This theoretical difference in update time is used as a reference value when making comparisons between VCPs.

3.3.2 Results

For this portion of the study, the latency time between tornado debris release and detection of a TDS is used as a performance metric for comparing multiple simulated VCPs. Changes in latency time are recorded for various combinations of debris counts and types, different debris starting positions ('seeds'), and different VCPs. The results in this section show a direct comparison between two VCPs: 'VCP A' and 'VCP B'. VCP A is extremely similar to VCP 215 implemented on NEXRAD; it scans at identical elevation angles to VCP 215, but with a constant scan rate to complete each elevation scan every 17.8 s, and no 'repeating' elevation scans for reflectivity versus velocity data collection. VCP B also scans at 17.8 s per PPI, but only elevation angles of 0.5°, 0.9°, and 1.3° are scanned. The result is a 5-fold change in total VCP update time (267 s for VCP A, and 53.4 s for VCP B), with identical data quality between the two VCPs. As shown later in this section, a difference in data quality has an appreciable effect on the observed TDS area, leading to spurious results. Thus, keeping the number of samples per scan constant ensures that the results are not influenced by changes in data quality between the two VCPs.

For a given set of SimRadar realizations, the only variable changing between realizations was random placement of debris. All other input parameters–LES, debris count, number of pulse pairs used, domain size, TDS criteria, etc.–are held constant within one set of simulations. At each pixel in the scan domain, emulated Z_H and ρ_{hv} are assessed for the TDS criteria, to determine if they satisfy the TDS thresholds. The sum of the area of pixels meeting the TDS threshold is computed, and is recorded as a time series for each elevation. This can then be compared between two VCPs with the same initial random debris placement; an example of a TDS area versus time plot is shown in Fig. 3.23, where TDS area is plotted as a function of time for a 0.5° elevation scan for both VCP A and VCP B.

In the example area versus time plot in Fig. 3.23, the 'stair-step' nature of the TDS area corresponding to both VCP A and VCP B is indicative of the fact that no new information about the nature of a TDS is gleaned between radar scans. As a result, each 'step' in TDS area for VCP A lasts for 267 s, and each step in TDS area for VCP B lasts for 53.4 s. Because the realization for both VCP A and VCP B uses the same input parameters and the same starting debris locations, each VCP A scan will align (both in area and time) with a scan collected by VCP B. This allows for a direct comparison between the two VCPs, as the two VCPs in a single realization are scanning the same spatial distribution of scatterers at the same time. To assess whether or not a VCP has 'detected' a TDS at a given time, the area of pixels meeting the TDS criteria are compared to a near-continuum of TDS area thresholds.

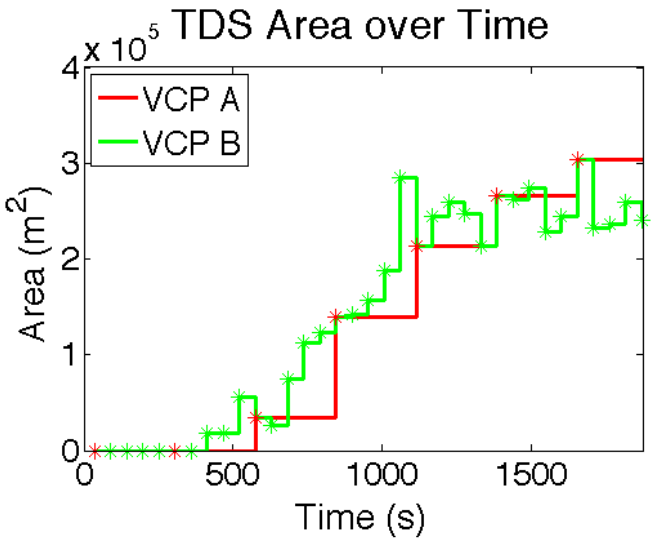

Figure 3.23: An example showing the TDS area with time for a slow VCP (VCP A; 267 s update time, red line) and a fast VCP (VCP B; 53.4 s update time, green line). Note the fluctuations in TDS area for VCP B, leading to TDS latency times greater than the theoretical values.

For each realization, the domain is scanned using both VCP A and VCP B. The time at which the total TDS area for each VCP reaches each threshold ('latency time') is recorded relative to the beginning of RCS ramp-up, and the mean of these latency times is calculated. The main interest in this study is the difference in latency times between the two VCPs, for a direct comparison of the improvement in lead time in tornado detection. This is then compared to the theoretical lead time improvement, based on the two VCP update times ($\frac{N_A - N_B}{2}$ = 106.8 s for VCPs A and B).

The first set of five SimRadar simulations was run at a range of approximately 14.3 km from the radar to the center of the tornado, with 50,000 leaves and 10,000 wood boards, with a linear RCS ramp-up over 1000 s ($t_0 = 115$ s and $t_1 = 1115$ s in (3.2)). Each realization uses a different initial random placement of debris, but are otherwise identical. Because the start time of VCP A relative to VCP B is arbitrary, the start time for VCP A is shifted in 53.4-s increments. This increases the number of samples for TDS latency time for each realization by a factor of 5, for a total of 25 realizations. To estimate statistical significance, nonparametric ordinary bootstrap resampling (Efron 1979) was applied using 25 samples with replacement and conducted 200,000 bootstrap resamples. A histogram of the bootstrapped means are plotted in panel a) of Fig. 3.24. This entire procedure is then repeated for a set of 5 SimRadar realizations with a higher debris count (250,000 leaves and 50,000 wood boards); this result is plotted in panel b) of Fig. 3.24. For reference, the 'theoretical' TDS latency time improvement of 106.8 s is plotted as a vertical red line in both panels.

The mean TDS latency time improvement over all 200,000 bootstrapped means for the low debris count is 207.1 s, and is 136.9 s for the high debris count. It is believed that the discrepancy between the mean improvement in TDS latency times in the realizations with low versus high debris counts is due to the fact that fluctuations in TDS area are much greater in the low debris cases, due to more transient debris lofting. More transient debris lofting should lead to more fluctuations in

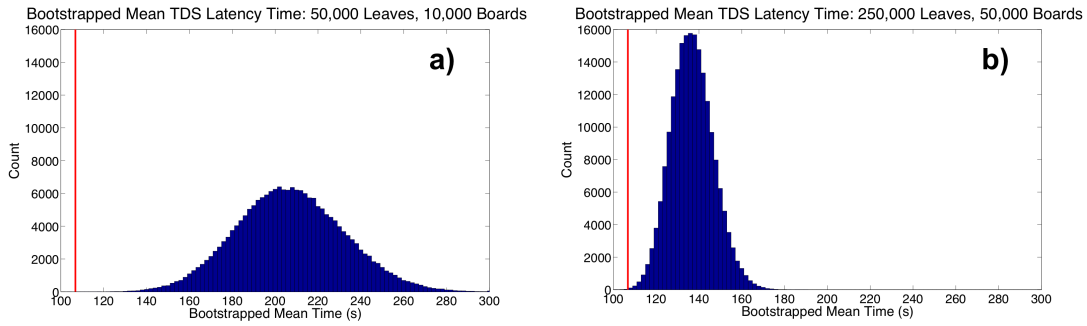

Figure 3.24: Histograms of bootstrapped means for TDS latency time with a low debris count (panel a) an a higher debris concentration (panel b).

TDS area, which is a situation where faster updates should provide more benefit to increase the lead time of tornado detections.

The histograms in Fig. 3.24 clearly show that the distribution of bootstrapped means is generally above the theoretical TDS latency time improvement of 106.8 s. For the lower debris case (panel a), all of the 200,000 bootstrapped means were greater than the 106.8 s theoretical value, while for the higher debris case (panel b), 199,930 (99.97%) of the 200,000 bootstrapped means were greater than 106.8 s. As a result, it can be conclusively said that the observed increase in TDS latency time is greater than the theoretical difference expected, based on the difference in VCP update times, and is statistically significant. This result supports the initial hypothesis and echoes a similar result in Wolfson and Meuse (1993) for wind shear detection.

The above results primarily focus on expected benefits in TDS latency time offered by rapid updates. However, when discussing faster radar updates, it is also

important to consider any possible drawbacks due to detrimental effects on data quality. For the automated tornado detection algorithm discussed previously, it is much easier to quantify improvements in TDS latency time, rather than assess any deleterious effects on the data quality caused by more rapid update times (i.e., false positives). However, when reducing the number of samples per radial, deteriorating data quality can cause erroneously low correlation coefficient (ρ_{hv}) (Bringi and Chandrasekar 2001). This can cause TDS criteria to be met, such that erroneously high values of TDS area are observed even when little or not debris is present. An example of this phenomenon is shown in Fig. 3.25, where the same observation is made using (a) 25 pulses per radial, and (b) 5 pulses per radial. The difference in observed ρ_{hv} can be seen in a comparison of panels (a) and (b), where more pixels of lowered ρ_{hv} are evident when the number of pulses per radial is reduced. Data quality for ρ_{hv} is worsened as a result of reducing the number of samples per radial, creating a scenario in which anomalously high TDS areas and reduced spatial continuity of the TDS are observed. Poor data quality has a deleterious effect not only on automated algorithm performance, but also on the ability of a human forecaster to detect tornadoes using polarimetric data.

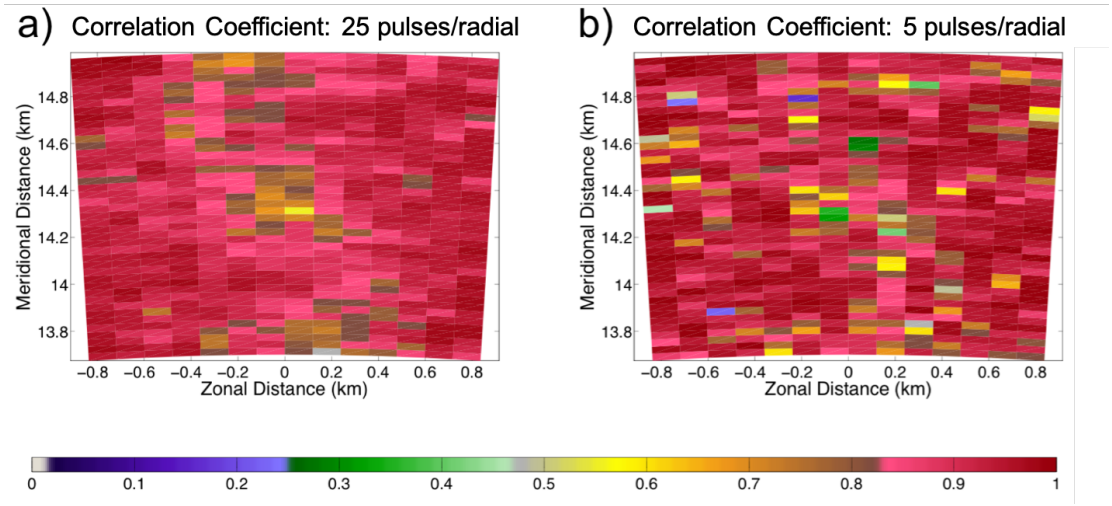

Figure 3.25: A comparison of the changes in ρ_{hv} with 25 pulses per radial (panel a) and with 5 pulses per radial (panel b).

3.4 Conclusions

In this study, the appearance and evolution of a TDS and TVS are analyzed for multiple heights, debris counts, and debris initiation domains in a simulated environment. This analysis is conducted for a tornadogenesis case using the CM1 model, where a violent tornado forms. The radar simulator was initially run at 1-min temporal resolution, where very significant changes were observed between successive scans. As a result, the study was conducted at 6-s temporal resolution. The results show that noticeable changes in various fields (ρ_{hv}, HCA class output, etc.) occur in as little as 6 s, and that significant changes in the spatial extent of the TDS are observed on timescales of 12-18 s, especially in cases where debris availability is limited. This finding motivates the desire to scan more rapidly than

both NEXRAD (300 s) and the proposed 1-min temporal resolution for NexPAR. Having polarimetric scans every 6 s ensures that the tornado is detected as early as possible. Seeing debris for several consecutive scans over ∼20 to 30 s will increase confidence in tornado detection where it might take a few minutes to achieve similar confidence with 1-min updates; this appears to be especially true at lower debris concentrations, where greater scan-to-scan TDS area fluctuations may occur. Additionally, rapid changes in TDS area may indicate a change in tornado intensity.

The results from the TDS evolution simulations with the CM1 model show that when debris availability is constant, the TDS area is highly correlated with the strength of the tornado (ΔV). This study is the first to use a storm-scale simulation to analyze the correlation between tornado intensity and TDS characteristics. Additionally, in the simulations where debris availability changes with time, there are significant changes in TDS area that correspond to the availability of loftable debris. This result is expected, but further underscores the point that the areal extent of the TDS signature depends on a combination of both tornado strength (e.g., Van Den Broeke and Jauernic 2014; Thompson et al. 2017), and availability of debris (Van Den Broeke and Jauernic 2014). This could indicate that in some cases–especially where debris availability is relatively low–using a TVS signature could be more useful than a TDS.

The results of the simulation also show that higher elevation scan angles tend to produce smaller TDS areas, despite having a similar TVS as lower elevation angles. This is likely due to a lack of debris being lofted to these higher heights. This is

consistent with observations that find TDS area decreasing with height (e.g., Fig. 8 in Bodine et al. 2013). At these elevations, the TDS area largely coincides with somewhat lower ρ_{hv}, but not a significant increase in Z_H. This likely suggests that the debris that are being lofted to these higher elevation angles are primarily lighter debris (i.e., leaves), rather than heavier debris with a higher RCS (i.e., wood boards). This agrees with expectations, as heavier debris tends to not be lofted as high as lighter debris.

Furthermore, the effect of the amount of debris on TDS area is studied. The primary result found is that increasing the debris count increases the total TDS area detected, and under some circumstances, the rate at which the TDS area increases. This result is observed at all analyzed elevation angles (e.g., Fig. 3.12). Increased debris count does not appear to have an effect on the time at which the TDS is initially observed at low levels when using a smaller debris initiation domain (Cases I and II), but the simulations with a larger debris initiation domain (Cases III–V) do indicate that debris count has an effect on the time at which a TDS is observed at higher heights AGL. It is theorized that this effect is due to a changing debris concentration (debris per unit area).

For the second goal of this study (changes in tornado detection latency times), the results show that improving the temporal resolution of a rapid-scanning weather radar improves the tornado detection latency time by a factor greater than that predicted by theory alone. The results from this study indicate that the improvement measured is 1.28–1.93x that of the theoretical lead time gain, likely owing to natural

fluctuations in the TDS area with time. This would indicate that the benefits of a rapid-scanning weather radar are greater than initially expected for tornado detection. This further emphasizes the desire for rapid updates in the next-generation nationwide weather surveillance radar. However, an example showing a spurious lowering in ρ_{hv} under poor data quality conditions emphasizes the point that rapid updates need to contain sufficient data quality.

This study is the first to analyze the timescales on which a major signature for tornado detection (TDS) appears and evolves, and is the first study to simulate a TDS during tornadogenesis. Because the TDS is observed to evolve on timescales much shorter than 1 min, a major impact of this study is to motivate the need for more rapid observations of tornadoes (i.e., every 20 s or less). Sub-1-min update times would almost certainly need to rely on PAR; 6-s update times like those in this study would likely require a fixed (i.e., not mechanically rotating) PAR. However, because of the challenges in meeting the 1 min full-volume update requirement while still maintaining acceptable data quality, obtaining volumetric updates every 15-20 s may not be feasible. The following question then arises: how can rapid updates be obtained for proper and timely tornado detection?

Scan techniques such as beam multiplexing (BMX; Yu et al. 2007) or radar imaging and digital beamforming (DBF; Isom et al. 2013) offer significant promise in achieving very rapid scans such as those proposed in this study. It is also believed that adaptive scanning–in large part only possible with a PAR–would provide the solution to this challenge. With a fully digital PAR, an area of interest such as a

tornado could be revisited with a much faster update time than that provided by an inflexible radar system such as a rotating dish antenna. In the future, one possible avenue for this research could be testing the tornado detection capabilities for an adaptively scanned system with that of a radar system with a fixed update time, while also taking data quality and non-uniform updates into account. Furthermore, real-world PAR systems such as Horus (Palmer et al. 2019) can be used to verify the adaptive scan ability for potential NEXRAD replacement applications.

Chapter 4

Adaptive Scanning and Pulse Reallocation to Improve Data Quality

4.1 Introduction

With the recent trend toward adopting phased array radar (PAR) in the weather radar community (Wurman and Randall 2001; Weber et al. 2007; Zrnić et al. 2007; Bluestein et al. 2010; Isom et al. 2013; Adachi et al. 2016; Kashiwayanagi et al. 2016; Palmer et al. 2019; Weber 2019; Yu et al. 2019), novel methods of improving both temporal resolution and data quality for weather radar should be explored. Chapter 2 primarily focuses on ways that scanning strategies can be applied for an entire scan domain. However, this may not be the most practical way to achieve an optimal balance between temporal resolution and data quality. Some scan strategies are shown to perform well in certain scenarios, while others are shown to be ideal in other areas. In an attempt to show the utility of cognitive radar concepts for improving data quality and/or temporal resolution, adaptive scanning is applied to leverage electronic beam steering in this chapter, such that data quality can be adaptively improved by reallocating radar resources.

Cognitive radar, in which radar resources are adaptively allocated toward a specific goal (Haykin 2006; Guerci 2010; Romero and Goodman 2013), provides significant promise for improving overall radar performance. Cognitive radar is advantageous for multiple reasons. First, it allows for a more efficient method of reallocating the resources of the radar. In a non-adaptive setting, all scan areas are treated as equal, even though some areas might have returns that are either unusable or of little/no interest to the end users of the radar. Second, the adaptive allocation can be either entirely automated or mostly automated. This has the advantage of providing superior data without increasing forecaster workload, which can be an obstacle in implementing new radar technology (e.g., Wilson et al. 2017). Third, the goals of an adaptive system can be altered to suit the needs of the radar end users (e.g., McLaughlin et al. 2005). In theory, this could mean that multiple scan goals are programmed into the system, and forecasters can choose which goal they would like to achieve with minimal oversight required.

In previous research, cognitive radar and/or adaptive scanning have been used in radar applications such as adaptive waveform transmission (Kurdzo et al. 2014, 2015b; Mitchell et al. 2018; Kurdzo et al. 2019), deriving human-attention models (Schvartzman et al. 2017), and adaptive scanning to improve temporal resolution (Chrisman 2009; Reinoso-Rondinel et al. 2010; Heinselman and Torres 2011). However, in many regards, the use of cognitive radar for weather radar systems has largely been unexplored. Possible reasons for this could be the relative novelty of PAR to the meteorological community, as well as the relatively low number of

PARs for weather observations currently in operation, thereby limiting the number of research opportunities. Despite the relative lack of prior research using cognitive radar techniques for weather radar, it is believed that this is a promising avenue of potential research moving forward, especially as PARs become more commonplace in the meteorological community.

One potential method for applying cognitive radar principles to weather radar observations is by attempting to maximize data quality while maintaining temporal resolution. This adaptive use of radar resources to improve data quality and volumetric update time is of great importance, as improved temporal resolution (compared to NEXRAD) is a primary goal of the NWS, and the ability to maintain current data quality levels while improving temporal resolution is still being studied (e.g., Mahre et al. 2020). Conversely, this method can be used in reverse; if a given level of data quality is desired, adaptive scanning can work backwards to estimate how much temporal resolution can be improved. This is especially important in areas where improving data quality beyond the NexPAR specifications may not be as advantageous as improving temporal resolution, such as in/around tornadoes, downbursts, or other rapidly evolving phenomena. An advantage of adaptive scanning is that various regions of the PPI can have different update times, depending on the needs of the end user; however, that is beyond the scope of this study.

Additionally, it is essential to show that such an improvement (or at the very least maintaining current levels while improving temporal resolution) in data quality is possible, as the final design decisions for a replacement of the current NEXRAD

system will be made in the near future. For example, one of the fundamental design decisions for a NEXRAD replacement system is whether the system will be a PAR or a parabolic dish system similar to NEXRAD. Prior to making such a decision, it is imperative that the scientific community has a full understanding of the pros and cons of a phased array system. As adaptive scanning is a significant advantage of PAR, it is believed that the ability of PAR to help meet the rapid-scan timeline is a worthwhile research opportunity.

In this project, the ability of PAR to improve weather radar data quality is studied by using cognitive radar principles. Herein, an improvement in data quality is said to correspond to a reduction in the statistical standard deviation of radar moment variables such as radial velocity (v_r); this could easily be expanded in the future to account for other moment variables such as reflectivity factor (Z_H) or polarimetric variables. In the future, the results of this study can also be generalized to 'work backwards', by starting with a minimum desired data quality and working to achieve the best possible temporal resolution for the desired level of data quality.

This chapter is organized as follows: section 4.2 describes the methods used in this study, and details the optimization setup and evaluation. Section 4.3 shows the results from two cases where adaptive scanning (pulse reallocation, or PR) has been applied. These results compare the impact of PR for the two cases in regions of high, moderate, and minimal importance. Finally, section 4.4 discusses the impact of these results, and their possible implications for the design of a nationwide rapid-scan weather radar system.

4.2 Methods

As stated in section 4.1, the purpose of this study is to adaptively reallocate radar pulses away from radials where either little is gained by dwelling longer, or the data quality is of minimal importance. For example, if there is a region with either minimal importance (e.g., a region where no precipitation is occurring or a region where precipitation is light and/or not rapidly evolving) or where decreasing the number of samples would not significantly affect the data quality, fewer pulses are transmitted along that radial.

4.2.1 Overview of Optimization Procedure

The model for optimization and PR proposed in this study is referred to as the 'ROI^2 model'. This is because the model relies on two major factors to decide where to reallocate radar pulses:

- What areas are of the most importance to the radar end users? In other words, where is the region of interest (ROI)?
- Where would increased samples have a significant impact on the data quality? In other words, what is our expected return on investment (ROI)?

Because the decision to reallocate pulses depends on both the region of interest (ROI) and the return on investment (ROI), the model is referred to as the ROI^2 model. A general overview of the procedure for the ROI^2 model is shown in Fig. 4.1.

The procedure begins with a surveillance scan, where the number of pulses transmitted and collected along each radar radial are equal. This is the baseline, to which all data quality after PR is compared. The surveillance scan is completed to assess where the areas of interest are, so the forecasters can assess what goals the ROI^2 model should focus on.

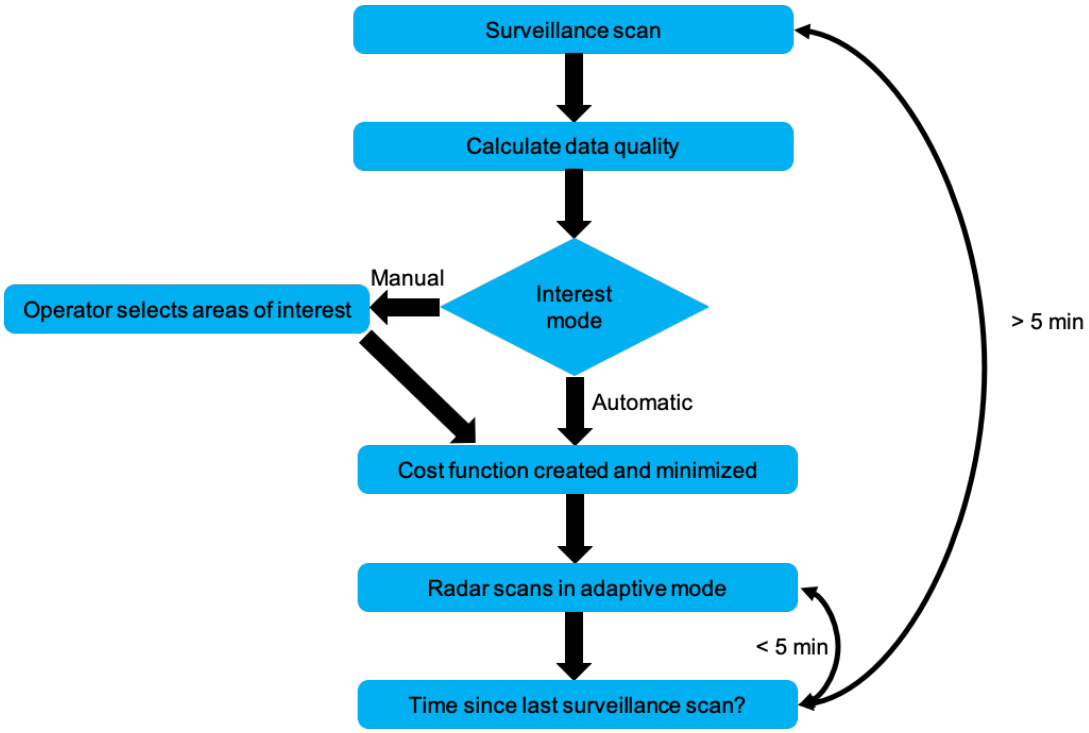

Figure 4.1: A high-level overview of the procedure for optimization in the proposed ROI^2 model.

After the surveillance scan has been completed, the data quality is estimated at each point in the PPI where the SNR is above a given threshold. Then, the user sets the interest level for each radial (either manually or automatically). A cost function is created for each range gate, and an 'optimized' number of pulses per

radial is estimated. This process then repeats for each of the analyzed range gates, such that a 'new' number of pulses has been calculated for each range and azimuth combination. These are then combined into a single pulse number per radial; further details of the optimization and the cost function are detailed in section 4.2.2.

The radar continues to scan in the adaptive (i.e., post-PR) mode for a set amount of time. In the example flow chart of Fig. 4.1, the amount of time is set to 5 min. This time limit is arbitrary, and could be changed depending on the situation. If the time limit has been reached, the radar begins another surveillance scan, and the process begins again. The reason 5 min is chosen as an example is that the region-based segmentation should be able to account for expected advection, such that the extent of each region does not need to be updated every 1 min. However, the choice of 5 min is somewhat arbitrary and should be evaluated for each application.

4.2.2 Optimization and Cost Function Setup

Prior to optimization, the importance value (one value for each radar radial) is set and the expected standard deviation of v_r for each pixel is calculated under non-adaptive conditions. The importance value (1–10) is set by the user and is set to be one value for each radar radial. There are many methods that could be used to assign importance values; this study uses a region-based segmentation method, where a connected region is segmented based on a 'seed point' and a minimum Z_H threshold chosen by the user. After the seed point and Z_H threshold have been set by the user,

a program is run which iteratively checks whether or not the neighboring points to the edges of the segmented region also fall within the parameters of the region to be segmented. An example of this region-growing method is given in Fig. S3 (`https://drive.google.com/file/d/1-pRofhvji_-CLZbaK7YW-eELJ_rio2hZ`), where the 16 May 2015 case (i.e., Case #1 in this study) is analyzed with a Z_H threshold of 43 dBZ.

All radials with at least one pixel in the segmented region are prescribed to have the user-defined importance value. For example, if the user sets the importance level to a 10 (i.e., high importance), selects a seed point, and the segmented region is found to span radials 45–120, then radials 45–120 are assigned an importance value of 10, and all other radials are assigned an importance value of 2 (i.e., baseline importance). Furthermore, radials within 5° of the edges of the segmented region are assigned the same importance value as the segmented region; this is done to account for advection between the surveillance scan and the end of the adaptive scanning period.

To achieve mathematical optimization, the first necessary step is to create a cost function to be minimized, subject to variable constraints. In this study, the cost function is centered around the statistical standard deviation of radial velocity (v_r). This equation is written in (2.4), and is re-written here for convenience:

$$\mathrm{var}(\hat{v}_C) = \frac{\lambda^2}{32\pi^2 M \rho^2(T_s) T_s^2}\Bigg[(1-\rho^2(T_s))\sum_{l=-(M-1)}^{M-1}\frac{M-|l|}{M}\rho^2(lT_s) + \frac{N^2}{S^2} + 2\frac{N}{S}\Big[1-\frac{M-1}{M}\rho(2T_s)\Big]\Bigg] \tag{4.1}$$

Here, $\mathrm{var}(\hat{v}_C)$ is taken to be the variance of the radial velocity estimator for CPS data processing mode with a pulse-pair processor, λ is the radar wavelength, M is the number of pulse pairs (equal to the number of pulses minus one for contiguous pulse pairs), T_s is the pulse repetition time (PRT), ρ is the normalized autocorrelation function, S is the signal power, and N is the noise power. The square root of $\mathrm{var}(\hat{v}_C)$ is taken to be the statistical standard deviation of v_r (σ_{vel}).

The cost function (J) is set up to be a scaled version of σ_{vel}. Here, σ_{vel} is multiplied by the importance level in each radial. This cost function is set up at each radar range gate, and is set up as follows:

$$J_i = \sum_{k=1}^{D} I_k \sigma_{vel}(k,i) \tag{4.2}$$

where J_i is the cost function for the i^{th} range gate, I_k is the importance level set for the k^{th} radial, and $\sigma_{vel}(k,i)$ is the standard deviation (i.e., the square root of the radial velocity variance in (4.1)) at the i^{th} range gate and the k^{th} radial. This cost function is calculated for the default number of pulses per radial, where the default number is assumed to be equal to the total scan time for a non-adaptive scan (18 s, which is consistent with NEXRAD, is used) divided by the pulse repetition time (PRT; herein, 1.5 ms is used). In the examples in this study, this allots 12,000

pulses for each scan, or 33.33 pulses per radial at 1° sampling; of course, the final number of pulses per radial must be an integer, but this conversion from floats to integers is done after optimization. The values for the total scan time and the PRT can be varied depending on the scan situation.

For each range gate, the cost function is minimized by changing the number of pulses along each radial. For example, if the default number of pulses per radial is 33, and it is found that changing the number of pulses for radial A to 34 and the number of pulses for radial B to 32 lowers J_i, then the number of pulses per radial is changed. This is done iteratively by using *fmincon* (i.e., Find MINimum of CONstrained nonlinear multivariable function) in MATLAB. The *fmincon* function uses linear and nonlinear constraints and upper/lower bounds on the number of pulses for each radial to constrain the cost function minimization. Herein, a minimum of 8 pulses per radial and a maximum of 128 pulses per radial are used. The constraints used are (1) the 12,000 pulse per range gate maximum, and (2) a maximum of 1.25x the default number of pulses for any given 90-degree sector at 1° sampling. This is done in order to simulate a single-faced PAR that is mechanically rotating. Because the PAR is mechanically rotating at a fixed rate (and the PAR can only beamsteer a certain amount off of broadside due to beam broadening and cross-pol contamination effects), the number of pulses for a given sector is restricted. The factor of 1.25 is somewhat arbitrary and can be changed in future simulations if desired; for example, a two-faced or four-faced system could likely have a higher factor than 1.25. Because

the beam in this experiment does not steer far off of broadside, beam broadening effects are not taken into account.

Once the constraints and bounds are specified, the minimization occurs in steps along the direction of greatest descent to find the local minimum of the cost function at each of the D range gates. While the radar can only transmit an integer number of pulses per radial, the optimization uses floats. Once the cost function minimization is complete for a given range gate, each radial has a floating-point decimal number of pulses. This process is then repeated D times, such that each range and radial combination have an initial number of (reallocated) pulses. Because the number of pulses must be constant along each radial, the D values for each radial must be combined into a single integer number of pulses for each radial, where the initial constraints from the optimization (no more than 1.25x the default number of pulses for any 90-degree sector, and no more than 12,000 pulses for the entire PPI) are still met. This is achieved by taking the X^{th} percentile of pulses in higher importance regions, and the Y^{th} percentile of pulses in lower importance regions, where $X > Y$.

4.2.3 Datasets Analyzed

Multiple real-world scenarios are used for this study, where NEXRAD moment data is used as input for the optimization model. The first scenario tested is a tornadic supercell case from 16 May 2015 near Tipton, OK. This data is collected by the KFDR NEXRAD radar, with the supercell approximately 30 km to the northwest

of the radar. The tornado from this case was rated as an EF-3 (Mahre et al. 2018), and was on the ground for nearly 90 min. For this study, the case is analyzed at 2302 UTC. The Z_H field is shown in Fig. 4.2, where the black contour represents a signal-to-noise ratio (SNR) of 15 dB, where the noise floor is assumed to be identical to that of NEXRAD (-7.5 dBZ at 50 km). One of the reasons that this case was chosen for analysis is that there are two storms of interest: the first is the primary supercell to the northwest of the radar, and the second is a smaller storm to the southwest of the radar. Choosing this case allows for an analysis of how the ROI^2 model performs when there are two distinct, spatially separated regions of interest.

The second case analyzed in this study is from a mesoscale convective system (MCS) over South Dakota on 6 July 2015 by the KFSD NEXRAD radar (Bodine and Rasmussen 2017), which was studied for the Plains Elevated Convection at Night (PECAN) field campaign (Geerts et al. 2017). The MCS spanned a wide range of azimuth angles relative to the radar, and was generally moving from northwest to southeast. A PPI of Z_H for this case is shown in Fig. 4.3; as in Fig. 4.2, the black contour represents 15 dB of SNR. This case was chosen because the segmented regions extend further out away from the radar, such that any effects from this can be explored.

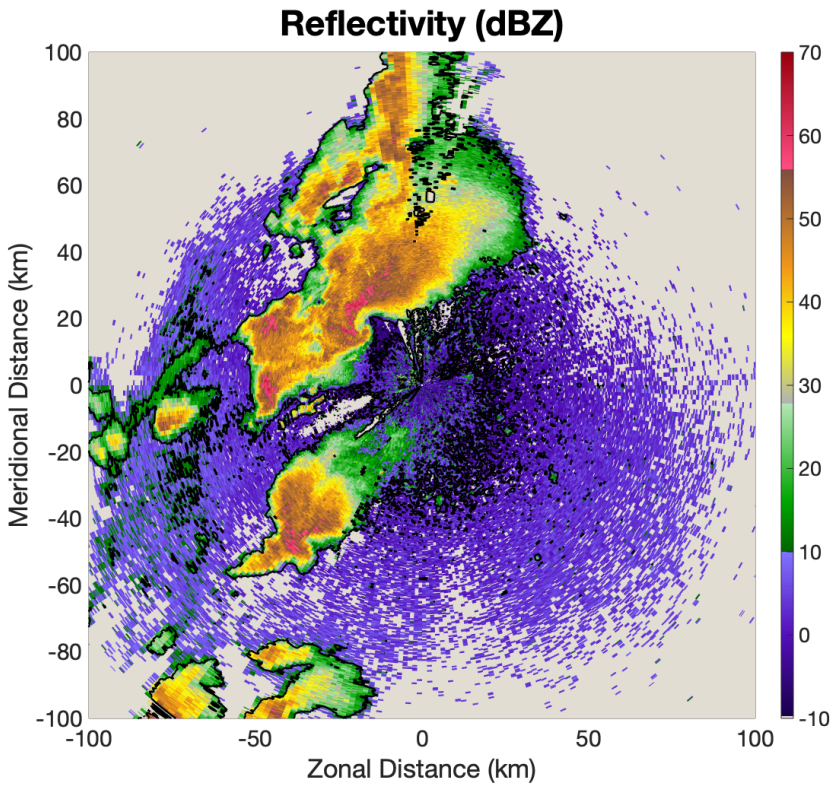

Figure 4.2: A PPI of Z_H from 16 May 2015 at 2302 UTC, from the KFDR (Frederick, OK) NEXRAD radar. The black contour represents an SNR of 15 dB. Only 200 km x 200 km are plotted, as the example optimization shown herein only analyzes the nearest 100 km to the radar.

4.3 Results

4.3.1 Case #1: 16 May 2015 'Tipton, OK Tornadic Supercell'

The first case analyzed is a tornadic supercell near Tipton, OK on 16 May 2015. The tornado associated with this storm has been studied in prior publications (Kurdzo

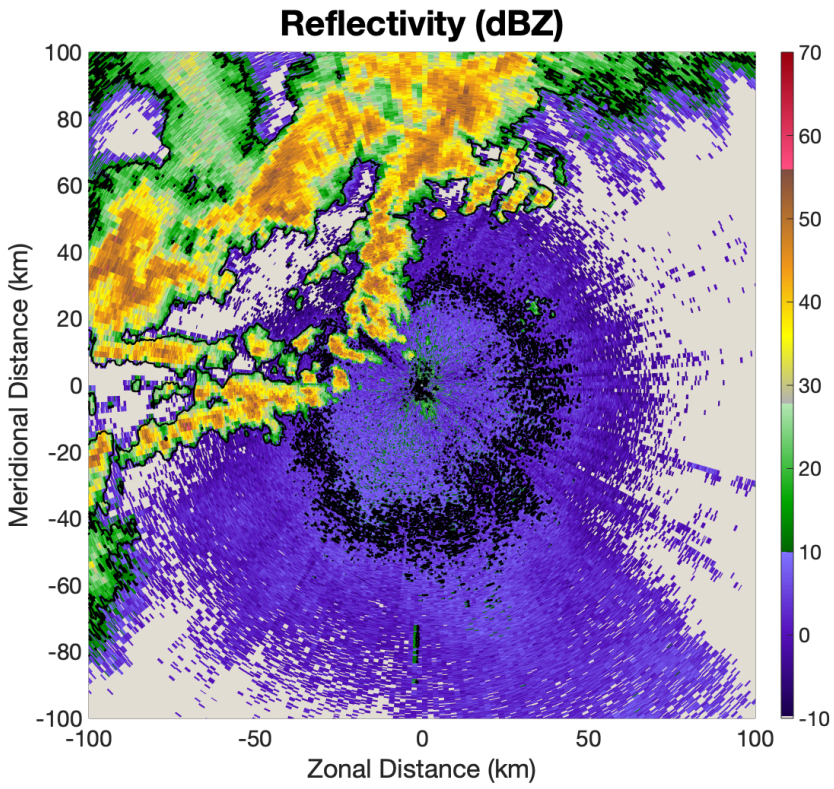

Figure 4.3: As in Fig. 4.2, but for the case from 6 July 2015 at 0401 UTC, from the KFSD NEXRAD radar.

et al. 2017; Mahre et al. 2018, 2019) with both NEXRAD data and with high-resolution mobile radar data. The data in this example is analyzed at 2302 UTC, when the tornado was approximately 30 km from KFDR (Fig. 4.2).

The data is first segmented into regions based on the input of the user. For this example, two regions are created by using seed points. The first is the primary supercell, to the northwest of the radar. This region was created by selecting a seed

point within the forward flank of the storm, and using the region-based segmentation method with a Z_H threshold of 43 dBZ. This region was classified as high importance (level 10). A second region was created by selecting the storm to the southwest of the radar; this region used a Z_H threshold of 32 dBZ, and was assigned medium importance (level 7). The two segmented regions are shown in Fig. 4.4. The remainder of the PPI is assigned to be of minimal importance (level 2). The importance level for each radial is assigned to be the highest importance level of any pixel in that radial; the importance level by radial is shown in Fig. 4.5.

Once these parameters are set, cost function minimization begins for each range gate. Pulses are reallocated subject to the constraints in section 4.2.2. This optimization is continually run until a local minimum has been found, subject to a function tolerance of 0.001 in the cost function. Once this criteria has been met, the optimization is stopped for that range gate, and optimization begins on the next range gate. This continues for each range gate to be analyzed. In this example, 400 range gates (100 km in range) are used in order to reduce the overall computational expense. After optimization has completed for all range gates in the analysis domain, the number of pulses per radial is determined by using the 'percentile method' described in section 4.2.2.

After PR has been completed, each radial has an integer number of pulses assigned to it (Fig. 4.6), where the number of pulses is subject to the original constraints. As mentioned in section 4.2.2, the number of pulses per radial is determined

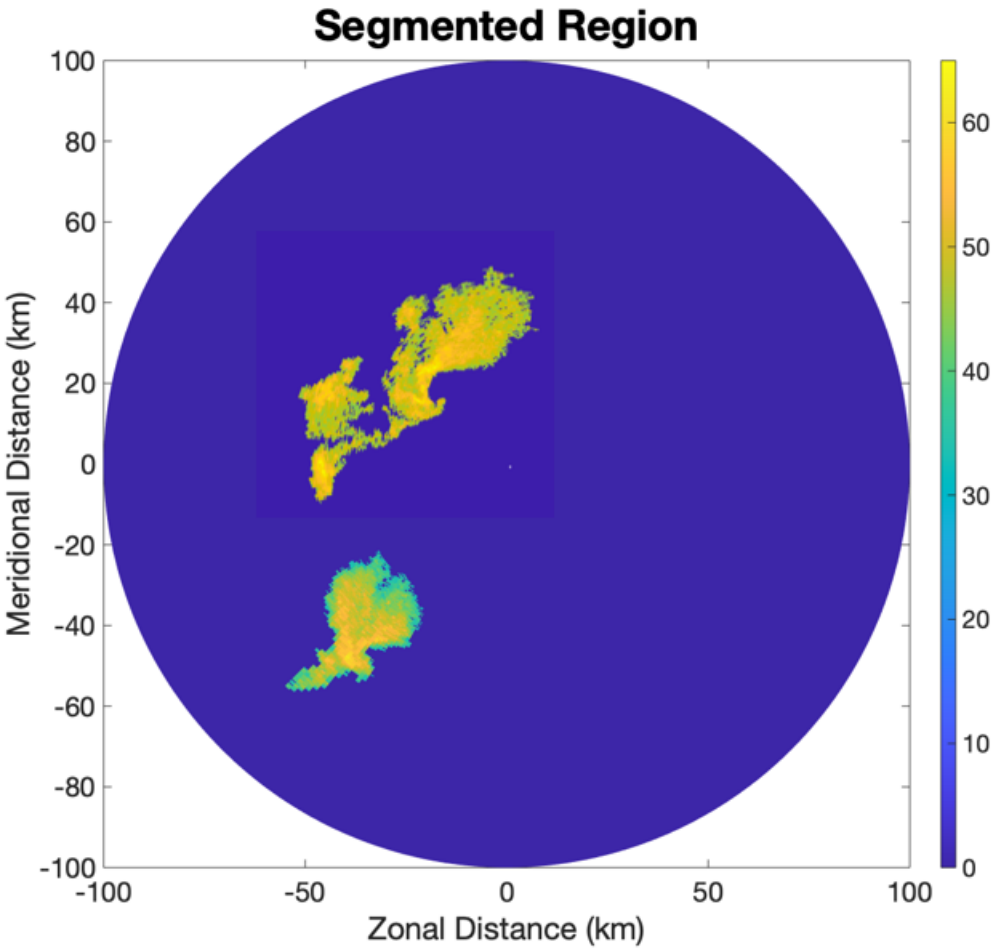

Figure 4.4: The regions which were segmented as being either 'high importance' or 'medium importance' for Case #1. This figure plots Z_H (in dBZ) for the high and medium importance regions only. In this example, the region to the northwest of the radar was classified as 'high importance', and the storm to the southwest of the radar was classified as 'medium importance'.

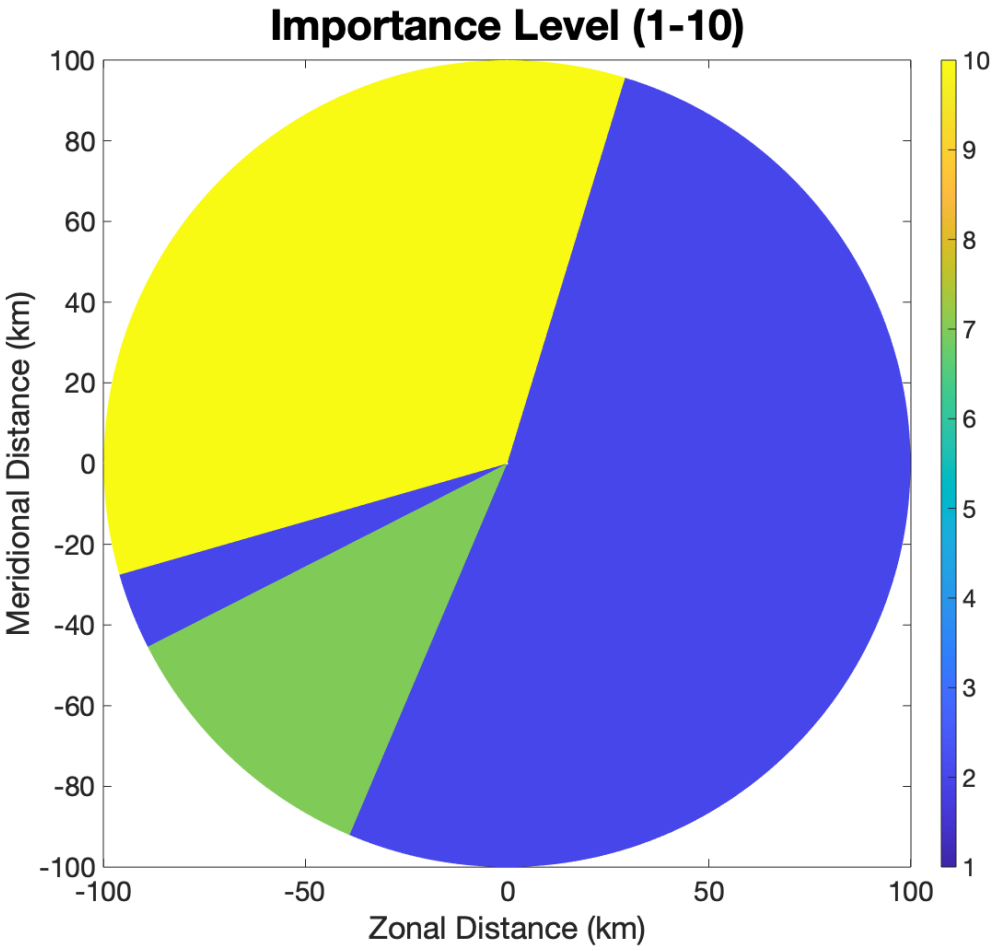

Figure 4.5: The importance level by radial, after region segmentation has been performed in Case #1. The storm to the northwest of the radar has been subjectively classified as high importance (10 out of 10) and the storm to the southwest of the radar has been classified as medium importance (7 out of 10). All other areas are classified as minimal importance (2 out of 10).

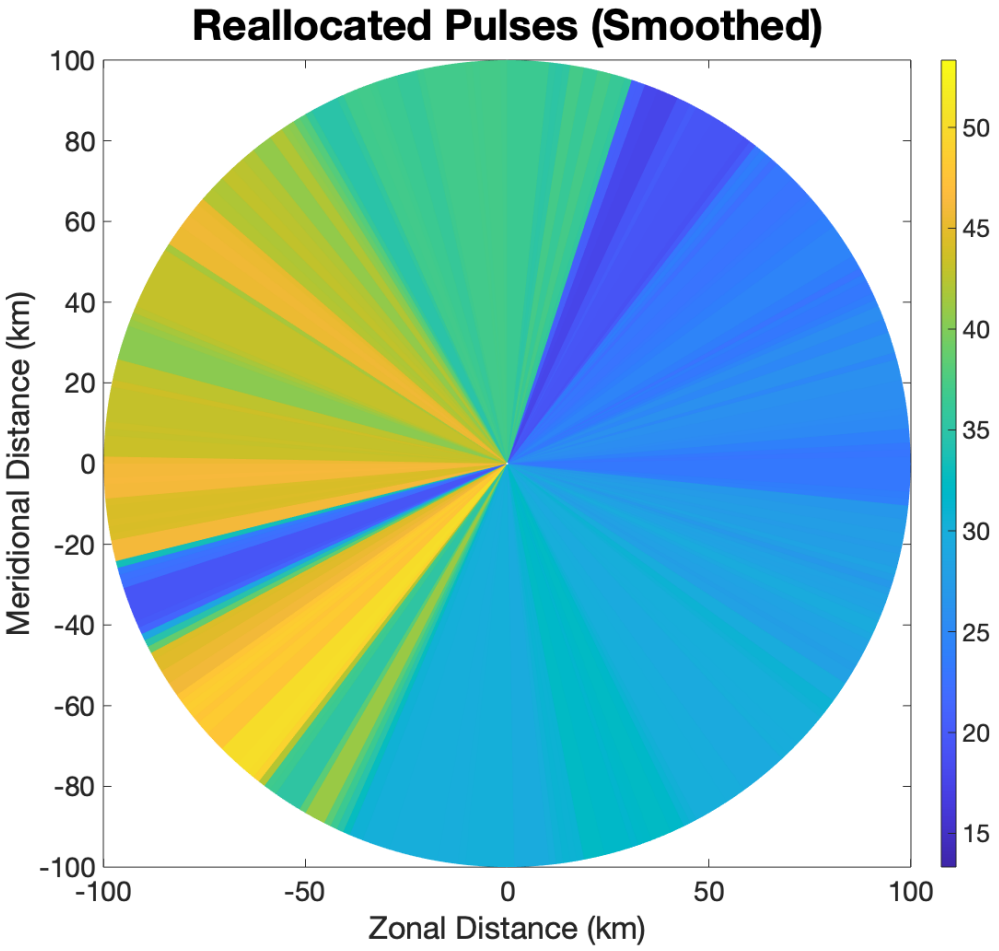

Figure 4.6: The 'new' number of pulses per radial after PR has been performed for Case #1.

by using a certain percentile of the reallocated pulses along each radial, where a different percentile is used for each region type. In this example, the number of pulses per radial in the high and medium importance regions were taken to be the 82^{nd} percentile along that radial, and the 62^{nd} percentile is used in the minimal importance

regions. It is evident in Fig. 4.6 that regions with high and medium importance have more pulses assigned to them than the remaining region(s). This result is expected, as in these regions, any decrease in σ_{vel} is weighted more heavily in the cost function because of it being multiplied by a higher importance factor. This makes it more advantageous to improve regions of higher importance than in regions of lower importance.

To verify that the data quality has improved, the standard deviation of v_r is plotted both before and after PR (Fig. 4.7). By comparing the two plots, it is clear that the the data quality has been improved in some regions. A few examples of these regions are circled in black in Fig. 4.7. For example, in the black circled region to the southwest of the radar, many of the points with high σ_{vel} (i.e., poor data quality) have lower σ_{vel} after PR. Note that both of the black circled regions are within either a 'high importance' or a 'medium importance' region.

Conversely, data quality has gotten worse in other regions. This is expected, as the total number of pulses in the PPI is fixed. Two examples of regions where data quality has gotten worse are shown in the red circled regions of Fig. 4.7. In both of the red circled regions, the σ_{vel} values are generally higher after PR. It should be noted that the regions circled in red in Fig. 4.7 are generally in the 'minimal importance' region, where poorer data quality should be expected.

To compare the data quality before and after PR, the difference in σ_{vel} is plotted in Fig. 4.8. In this figure, blue values represent an improvement in data quality after PR, and red values represent poorer data quality after PR. As expected, the

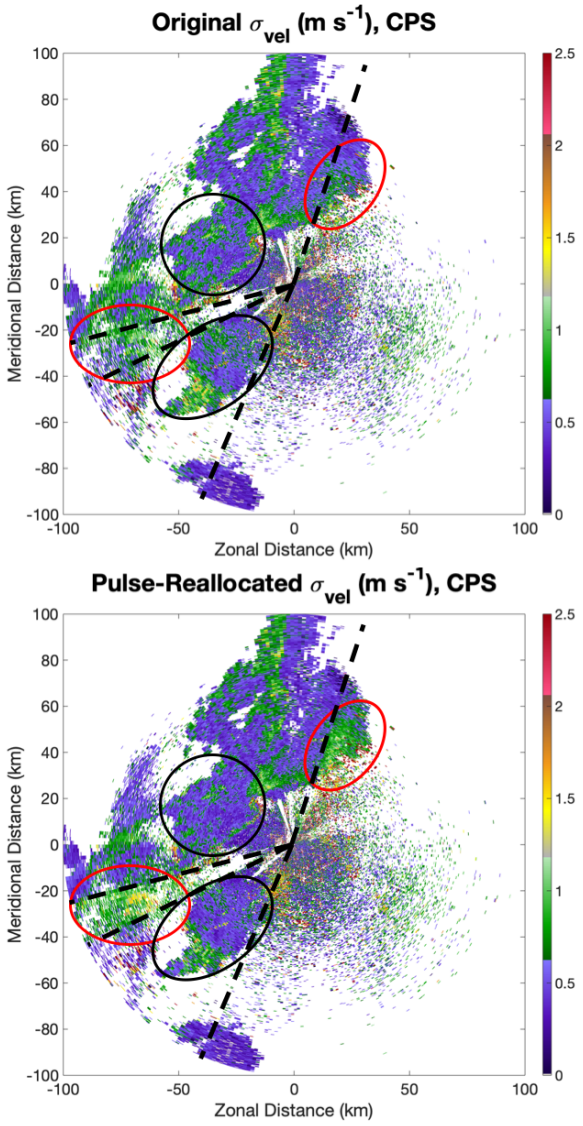

Figure 4.7: A comparison of σ_{vel} before and after PR has been performed for Case #1. The black circled areas represent regions where data quality has improved by using PR, and red circles represent areas where data quality has gotten worse because of PR (generally in the regions of minimal importance). Black dashed lines represent the edges of the various regions in Fig. 4.5.

areas with improved data quality correspond with the regions designated as being of higher importance in Fig. 4.5 and with more pulses per radial in Fig. 4.6. Compared with the original σ_{vel} values, the post-PR values of σ_{vel} are up to ∼35% higher in the minimal importance region, and are up to ∼35% lower in the medium or high importance regions.

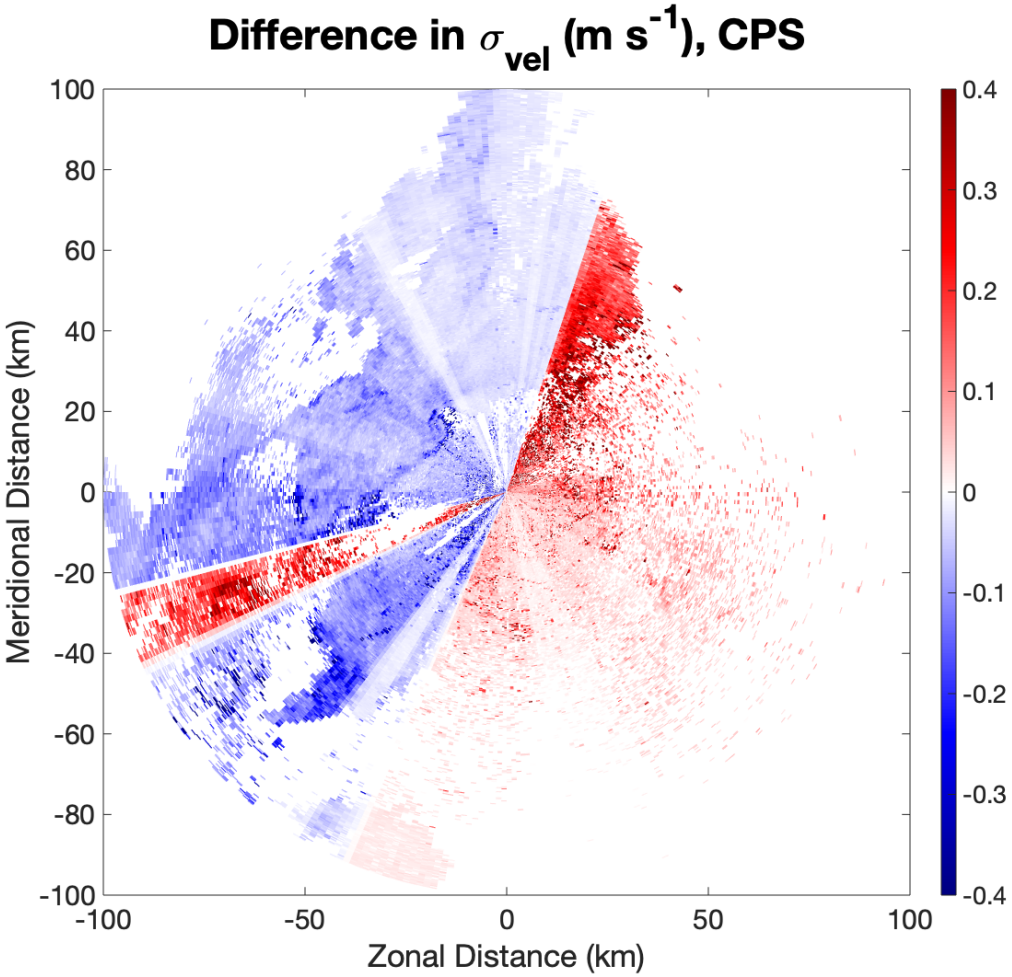

Figure 4.8: A measure of the difference in σ_{vel} before and after PR for Case #1. Blue (red) regions represent areas where data quality has gotten better (worse).

A line graph showing the change in mean data quality for the original scan and the simulated post-PR scan is shown in Fig. 4.9. These values are obtained by averaging the expected σ_{vel} at all points in each region type both before and after PR. As is evident from this figure, data quality is improved in the high and medium importance regions by performing PR, at the expense of data quality in the minimal importance regions. In the minimal importance region, the mean σ_{vel} increases from 0.920 m s^{-1} to 1.044 m s^{-1}, representing an increase of 13.5%. In the medium importance region, the mean σ_{vel} decreases from 0.822 m s^{-1} to 0.723 m s^{-1} (a decrease of 12.0%), and the mean σ_{vel} decreases from 0.738 m s^{-1} to 0.673 m s^{-1} in the high importance region, representing a decrease of 8.9%. One interesting note is that greater improvement is seen in the medium importance region than the high importance region. This result of the medium importance regions having greater improvement than high importance regions is not believed to be robust.

4.3.2 Case #2: 6 July 2015 'South Dakota MCS'

For the second case in this study, an MCS from South Dakota is examined. A seed point in the MCS to the north of the radar is selected, and a Z_H threshold of 30 dBZ is used. The segmented region is shown in Fig. 4.10, and all radials with at least one pixel in the segmented region (or any radial within 5° in azimuth of the segmented region) is classified as being high importance; all other radials are assigned to be minimal importance.

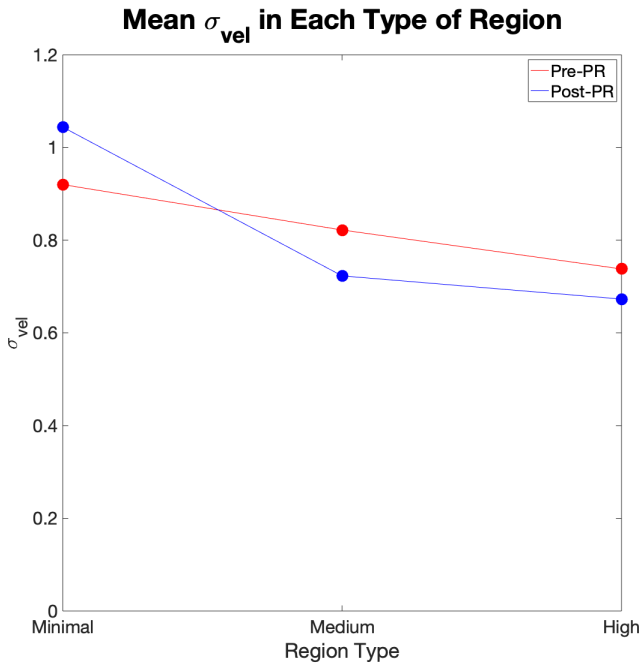

Figure 4.9: A comparison of data quality both before and after PR in each region type. The red line represents data before PR, and the blue line represents data after PR.

After optimization has been completed, the pulses are reassigned, and the new number of pulses per radial is shown in Fig. 4.11. As with Case #1, the number of pulses per radial in the high importance region was taken to be the 82^{nd} percentile along that radial, and the 62^{nd} percentile is used in the minimal importance regions. As expected, the radials containing the segmented region are assigned more pulses than the other radials. This closely follows the reallocation in Case #1. It is currently unknown why there is a sharp gradient in the number of pulses due north of the radar; it is unclear whether this is an artifact or a correct result of PR. Further

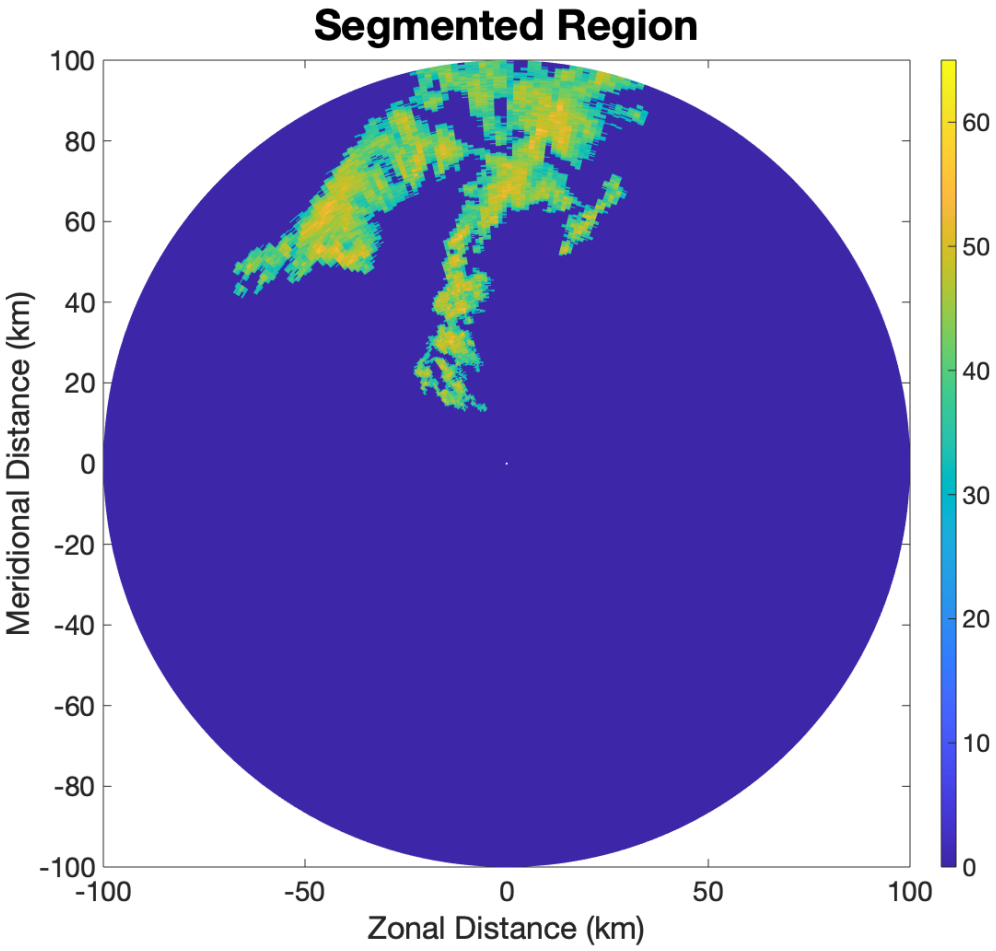

Figure 4.10: The regions which were segmented as being higher importance for Case #2. This figure plots Z_H (in dBZ) for the high importance region only. In this example, a portion of the MCS was classified as 'high importance', while the rest of the PPI was classified as minimal importance.

testing will be necessary to assess this phenomenon. In general, the reallocation of pulses follows the outline of the segmented region.

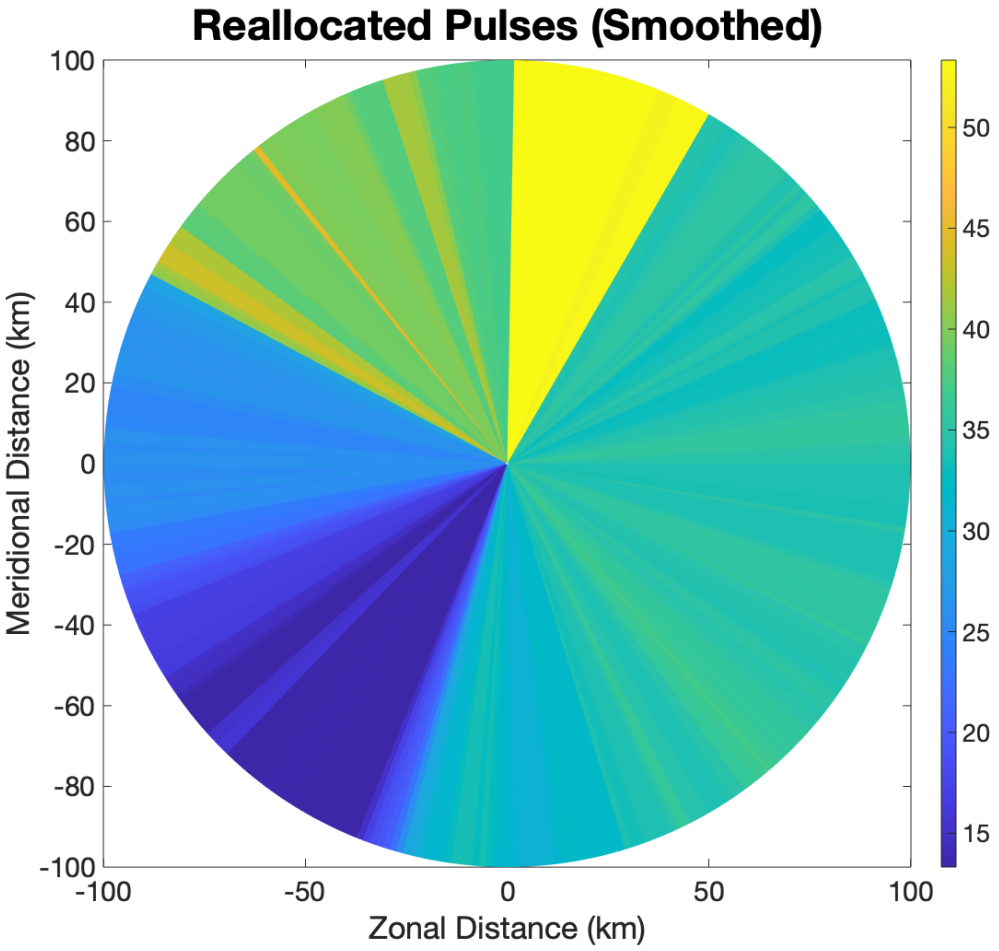

Figure 4.11: The 'new' number of pulses per radial after PR has been performed for Case #2.

As in Case #1, the data quality is compared both before and after PR. Fig. 4.12 shows the data quality both before and after PR, with black circles highlighting areas where data quality improved after PR and red circles highlighting areas where data quality got worse because of PR. The areas where data quality becomes better

and worse agree with expectations. Areas with increased numbers of pulses observe better data quality, while areas of minimal importance observe worsened data quality. This is explicitly shown in Fig. 4.13, where improved data quality (blue regions) closely correspond with the area of higher importance.

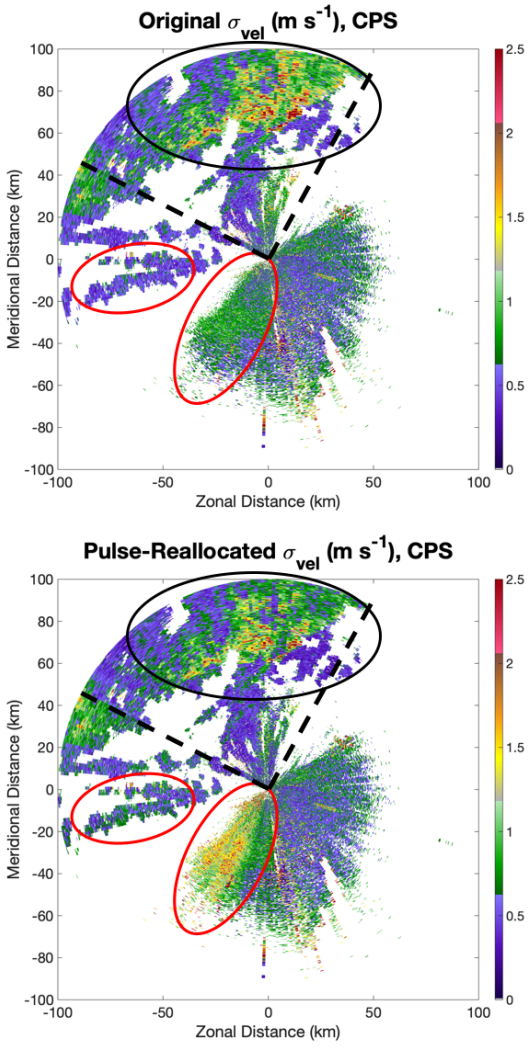

Figure 4.12: As in Fig. 4.7, but for a comparison of σ_{vel} before and after PR has been performed for Case #2.

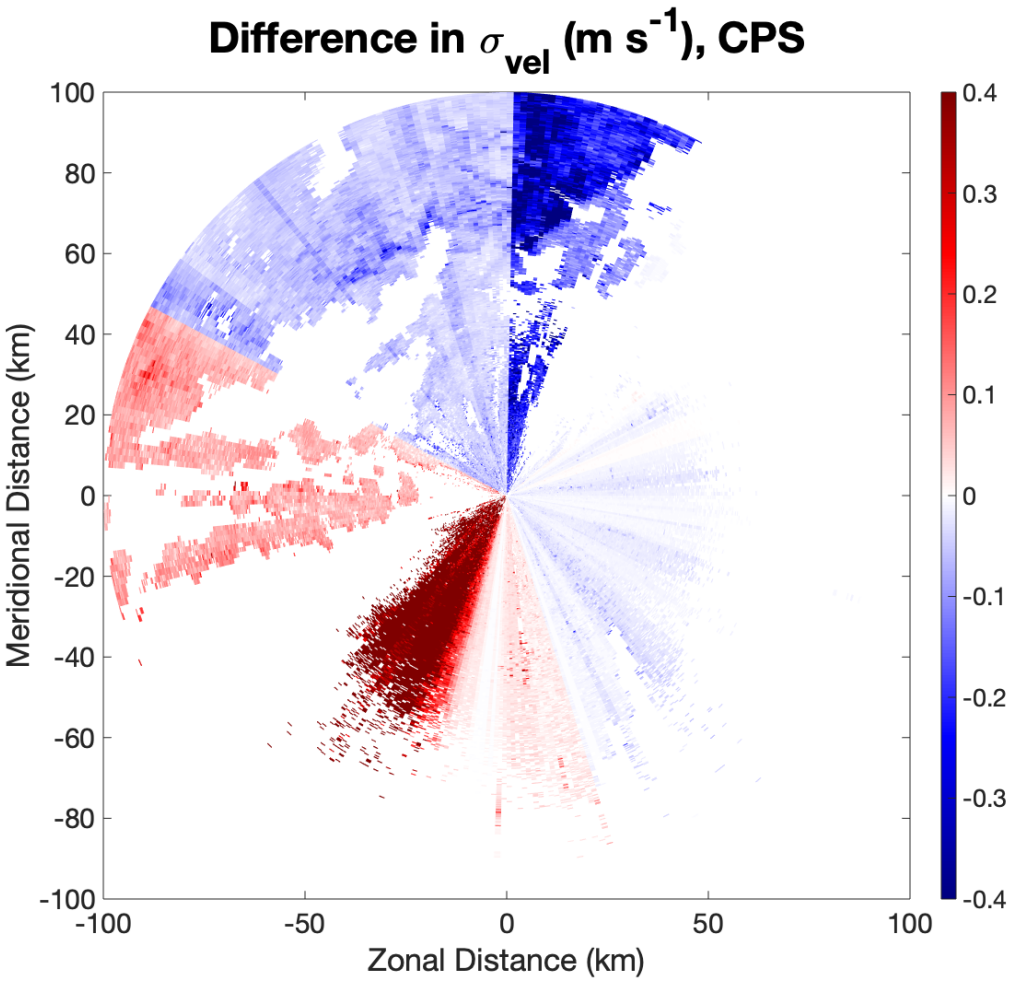

Figure 4.13: A measure of the difference in σ_{vel} before and after PR for Case #2. Blue (red) regions represent areas where data quality has gotten better (worse).

Finally, the mean σ_{vel} is compared for each region type. In the high importance region, the mean σ_{vel} is 0.758 m s^{-1} prior to PR; this decreases to 0.657 m s^{-1} after PR, representing a decrease of 13.3%. In the minimal importance region, the mean σ_{vel} increases from 0.762 m s^{-1} to 0.896 m s^{-1} (increase of 17.7%). This example

shows the same general result as Case #1: data quality is improved in the region of interest, while data quality becomes poorer outside of this region.

4.4 Conclusions

In this study, a new adaptive scanning model (ROI^2) is created and evaluated. This model takes in data from a non-adaptive scan (i.e., a surveillance scan) and performs adaptive PR in an attempt to improve data quality (herein defined as changes in σ_{vel}) in regions of heightened interest. The ROI^2 model is tested on two real-world NEXRAD cases: one is a supercell case where most of the data of interest are within 50 km of the radar (Case #1), while the other case is an MCS that extends further in range (Case #2). The resulting data quality both before and after PR is compared.

For Case #1, a high importance region and a medium importance region are defined. It is shown that the optimization model successfully increases the number of pulses in the higher importance regions by diverting pulses away from the minimal importance region. It is found that data quality improves by 8.9% in the high importance region and improves by 12.0% in the medium importance region. This result is encouraging, as this achieves the overall goal set out by the model. As expected, data quality gets poorer in the minimal importance regions.

Case #2 examines the effect of PR (based on the ROI^2 model) on an MCS case. In this example, only a high importance and a minimal importance region are examined. As expected, the number of pulses per radial increases in the high

importance region, and decreases outside of that region. Qualitatively, the effect is the same as in Case #1: the data quality is found to improve in the radials marked as high importance (13.3% decrease in σ_{vel}), while data quality becomes poorer outside of this region (17.7% increase in σ_{vel}).

The fact that both cases show similar results from PR and the ROI^2 model is encouraging, as the model successfully improves data quality in the desired regions in both cases. Because the ROI^2 model is only possible with a PAR, these results show utility of a PAR system for achieving high-quality rapid updates. This is an important point to consider, as it showcases a major advantage of PAR for a possible NEXRAD replacement.

In the future, there are multiple ways that this study can be expanded. For example, the current optimization method is a single-objective optimization, as the importance level and σ_{vel} are combined into a single cost function. An improved method for achieving the optimization is to use a multi-objective optimization (MOO), which should do a better job of accounting for multiple, competing goals. Further, the standard deviation of Z_H (σ_Z) can be considered. This was not considered in this study for two reasons. First, the use of σ_{vel} was primarily chosen as a proof of concept for the ROI^2 model, in order to see if the PR model would be successful on a general case. Second, considering σ_Z as the metric for data quality would present a challenge, as the interest level is generally tied to higher Z_H regions, while the most gain (i.e., return on investment) should be obtained in the lower SNR regions. Because there is a strong correlation between Z_H and SNR,

these two goals would be nearly directly competing against each other. Thus, it is believed that including σ_Z would be difficult while not using a true MOO.

Furthermore, the adaptive scanning paradigm can be expanded in other ways. In theory, the PRT can be adaptively changed depending on the extent of desired data in range. For example, if a PRT of 2 ms is used (such that the maximum unambiguous range is 300 km) but there is no data of interest beyond 150 km in range, the PRT can be shortened to 1 ms; this would have the effect of doubling the number of pulses along that radial for a given dwell time. Other scan methods that can be used adaptively are beam multiplexing (BMX) and radar imaging. As is shown in Chapter 2, BMX almost always improves data quality, while radar imaging needs to be used rather judiciously to avoid sharp gradients in Z_H. An adaptive scanning method, similar to that in Weber et al. (2017), would be extremely beneficial for improving data quality and/or temporal resolution.

Finally, the region-based segmentation can be expanded and/or improved upon if the forecaster workload is believed to be too high. Storm-tracking algorithms such as TITAN (Dixon and Wiener 1993) and SPA-MHT (Judy 2020) can be used to estimate the advection/evolution of the regions of interest with time, such that the forecaster would not have to re-select the regions of interest after every surveillance scan. To further automate the segmentation process, automated algorithms for certain hazards (e.g., hail, wind, tornadoes, etc.) can be used to automatically assign an importance level to certain storms. Additionally, seed points can be expanded to

search in three dimensions, as opposed to the two-dimensional search in this study. This would enable the same storm to be selected at all elevation angles.

Chapter 5

Conclusions and Future Work

5.1 Summary & Conclusions

In this dissertation, results are presented from various projects that focus on the goal of improving the temporal resolution of a future replacement for NEXRAD. In moving from a system with 5-min updates to 1-min updates, it is important to understand the benefits achieved from such a change. It is equally important to understand the scanning techniques and methods that can achieve 1-min volumetric updates, as design requirements and radar architecture decisions will depend upon the necessary scan modes.

In Chapter 2, the effect of various scanning strategies on data quality in a simulated 1-min update time scan is assessed. This work is essential to understanding the scanning strategies that can achieve rapid (i.e., $\sim$1 min) updates with acceptable data quality. While Chapter 2 primarily focuses on the specific methods for achieving faster updates (i.e., the 'how?'), Chapter 3 is primarily focused on the benefits achieved from employing rapid scans at sub-1-min temporal resolution for tornado detection. Finally, in Chapter 4, cognitive radar and adaptive scanning–which has been largely unexplored for weather radar applications–is considered for improving

data quality in certain regions based on varying levels of interest. The adaptive scanning method used in Chapter 4 can be used to either improve data quality in certain regions where high quality data is essential, or it can be used to improve temporal resolution in areas where phenomena may be evolving rather quickly (i.e., tornadoes, regions of high wind shear, downdrafts, etc.).

Chapter 2 analyzes the data quality for Z_H and v_r for three techniques: a pure reduction in the number of pulses per radar radial (i.e., the 'naive speedup method'), beam multiplexing (BMX), and radar imaging/digital beamforming. These three scanning strategies are tested for multiple times and elevation angles, such that the expected data quality (based on the expected statistical fluctuations) is calculated at approximately 500,000 points. These results show that compared to a baseline NEXRAD scan, simply reducing the number of samples per radar radial has a significant deleterious effect on data quality. This result is expected, but still emphasizes the point that other scan techniques will need to be employed in order to obtain rapid updates of 1 min or less. The second technique used is BMX; the results from the simulations of BMX show that BMX always provides an improvement in data quality in Z_H, and usually provides an improvement in v_r. Cases where data quality in v_r is reduced are generally caused by high spectrum width (such that successive pulse pairs were already highly decorrelated, even before using BMX mode), or in low-SNR regions, where pulse pairs are already more decorrelated than in high-SNR regions.

A disadvantage of using BMX is the lack of ground clutter filter support; this is because BMX data collection mode only collects two successive pulses at the same location, while a ground clutter filter requires long dwells to assess whether there is very long-term correlation over many pulses. Thus, BMX mode is not recommended for low elevation angles and/or areas where ground clutter contamination is a significant concern. However, outside of these areas, BMX offers significant promise for being able to offer rapid updates for a weather radar system, with calculated speed-up factors between 1.7 and 2.9.

Finally, radar imaging/digital beamforming is tested as another method to speed up data collection with high-quality results. The results from this portion of the study show that while radar imaging does tend to provide better data quality and/or faster scan times for the domain as a whole, the higher two-way sidelobes from the spoiled transmit beam cause regions of very poor data quality. The poor data quality in these regions can cause the average data quality for the whole domain to become so poor that the 'net gain' is completely removed, and the average data quality is worse than in a pencil beam-scanned mode. From these results, it is clear that radar imaging should be used judiciously, and should be avoided in regions with a significant gradient in either Z_H or v_r.

The results from Chapter 2 show that many of the scan techniques necessary to achieve rapid updates require a PAR. Both BMX and radar imaging require a PAR, and these methods combined show considerable promise for achieving the desired scan times of 1 min. Therefore, it is believed that use of a PAR is essential to

achieving rapid updates for the NOAA/NWS desired goal of improving volumetric temporal resolution.

In Chapter 3, the benefits of improving temporal resolution to 1 min or less is evaluated for tornado detection. Previous literature has suggested that tornadoes and severe storms can evolve on the order of tens of seconds or less, and that very rapid updates are necessary for proper research to be conducted. However, the literature on the operational effects of rapid updates on tornado detection is relatively scant, with the exception of some human-in-the-loop studies such as Heinselman et al. (2012) and Wilson et al. (2017). This study is the first to examine possible operational impacts of radar updates much faster than 1 min, and is also the first to examine the growth of a TDS and TVS in time using NWP data. To achieve this goal, a tornadogenesis simulation is used in conjunction with a radar simulator.

The results from this study show that the TDS does evolve on timescales much faster than 1 min. As a result of this, it appears that sub-1-min updates in and around a tornado may be necessary for proper and timely detection. Fig. 3.7 shows that there can be a significant change in the radar moment fields and the HCA over the 60 s between scans. When improving temporal resolution by a factor of 10 (i.e., 6 s updates), the short-term changes in moment fields and the HCA are more properly observed. For cases where the debris are initiated in a small domain (such that the tornado initially starts outside the domain and moves into the domain with time), the total area identified as a TDS grows by 1.43 km^2 in 42 s at the lowest analyzed elevation angle. This simulation configuration would most closely mimic a

case where a growing tornado forms in a region with very little loftable debris, before moving into a region where leaves or pieces of wood would be available for lofting. When this simulation is repeated for a wider debris initiation domain–where the tornado is fully contained within the debris domain at all points in its lifecycle–the rate at which TDS area increases with time is lowered to 4000–10000 $m^2\ s^{-1}$. Despite this reduction in TDS ramp-up rate, there are still significant changes observed in the various radar fields on timescales less than 1 min. Additionally, even a ramp-up rate of 10000 $m^2\ s^{-1}$ implies that a TDS can grow from 0 km^2 to 0.6 km^2 over a 60 s period. The changes in TDS area are found to closely follow changes in the strength of the tornado, which is expected based on previous results by Van Den Broeke and Jauernic (2014) and Thompson et al. (2017). The total TDS area is also found to change considerably based on availability of debris, so a combination of these two variables should be considered when trying to assess possible tornado strength from an ongoing TDS. The rapid updates offered in this simulation are also believed to be useful for forecaster confidence; seeing the same trend over several scans can help to assure a forecaster that a trend is real, rather than due to statistical fluctuations. This should help aid timely and accurate issuance of warnings.

Additionally, changes are observed based on height AGL. At lower heights, the rate at which the TDS area increases is greater than at higher heights. This would imply that rapid updates are especially important closer to the ground. However, many of the common signs of a TDS (e.g., significantly lowered ρ_{hv}) are not as pronounced at higher heights AGL. For example, many ρ_{hv} values near the ground

are clearly lowered due to the presence of heavier debris that cannot be lofted as high as lighter debris such as leaves. At higher heights, where the debris counts tend to primarily consist of smaller debris and the ratio of debris to hydrometeors may be lower, the typical TDS signatures are not as obvious, which could further drive the need to scan more rapidly at higher heights AGL as well.

Finally, the amount of debris in the initiation domain is examined as possibly having an effect on the rate at which TDS area increases. It is found that in the smaller debris initiation domain (400 m x 400 m), the amount of debris does not significantly affect the rate at which the TDS area increases, whereas in cases with a larger debris initiation domain (where the debris concentration is lower), there does appear to be a correlation between the debris count and the rate at which the TDS area increases. Furthermore, the total observed TDS area does appear to be a function of initial debris count in all cases. Given the implied correlation between TDS area and the intensity of the tornado (Thompson et al. 2017), timely updates may be valuable for forecasters in providing up-to-date information about possible tornado strength, which could in turn affect messaging for the public.

The study in Chapter 3 is the first to track a TDS as it grows and evolves during and after tornadogenesis. While previous studies have primarily focused on the research-related benefits of sub-1-min updates of tornadoes, the results in Chapter 3 show that sub-1-min updates could be extremely helpful for operations as well. Changes in TDS area with height and debris count, concentration, and

availability indicate that rapid updates will be useful for timely, accurate warning issuance with specific communication language for the public.

In Chapter 4, a novel optimization model for adaptive scanning based on cognitive radar principles is used. This chapter presents the optimization model as a proof-of-concept for an adaptive scanning method for improving data quality and/or temporal resolution. The optimization used herein relies on the minimization of a cost function that takes both data quality (as assessed by the expected standard deviation of v_r) and importance level into account. The optimization is run, and the results from both a supercell case and an MCS case are shown.

In the first case, a 'high importance region' and a 'medium importance region' are created. The purpose of these regions is to encourage better data quality, at the expense of allowing data quality to become poorer outside of these regions. Case #1 (supercell) decreases the expected RMSE (i.e., improves data quality) by 8.9–12.0% in the high and medium importance regions. In the second case, only a high importance region is demarcated; RMSE decreases by 13.3% in this region. These improvements in data quality in the higher importance regions come at the expense of poorer data quality in the minimal importance regions; this result is expected, as the total number of pulses per PPI is fixed. Overall, the ROI^2 model is successful in proving that adaptive PR can be used for improving data quality in the areas of interest.

5.2 Future Work

Going forward with this project, there are several areas where further work could be done. Beginning with Chapter 2, a way that this type of project could provide even more useful information is to expand the scope of examining the effects of scanning strategies and radar design on data quality. For example, this study does not consider any polarimetric variables in its data quality assessment. The reason for this is that polarimetric bias in planar PARs is considered a much larger obstacle to obtaining high-quality radar data. Additionally, because radar architecture and design is currently unknown (with several possible options), the large number of possibilities precludes an in-depth study for all scanning strategy and radar design combinations. Therefore, one valuable avenue for future research on this topic is to examine how the data quality would change for polarimetric variables, when assuming a few specific radar designs. Furthermore, the effect of radar design is not considered in Chapter 2, such that these results can be applicable for any PAR application with a similar (i.e., 1°) beamwidth. Thus, the effects of steering off of broadside–such as beam broadening–are not considered herein. It is believed that a more complete treatment of various radar design ideas (especially as it relates to polarimetric radar data quality) would be a fruitful continuation of this project. Testing the scanning strategies of Chapter 2 on a real-world radar system such as Horus (Palmer et al. 2019) would also be a logical next step for this research.

Combining the 'improved data quality' goal of Chapter 2 and the 'rapid update' goal of Chapter 3, another area where future research could be useful is for achieving a balance between data quality and sub-1-min updates. In some regions, phenomena may not be evolving quickly, and the primary goal should be longer dwells to assure that data quality is maximized for a 1-min update time. Conversely, some regions evolve on timescales much faster than 1 min, so it may be acceptable to sacrifice data quality for the purpose of obtaining sub-1-min updates in these specific regions. Additionally, it should be noted that the case examined in Chapter 2 is a high-impact supercell/tornado case. Most of the time, radars will be scanning other phenomena that do not evolve as quickly. Therefore, it may be useful to explore the possibility of adaptively dwelling longer (such that update times exceed 1 min in certain regions) to achieve even better data quality, especially in regions where data quality from 1-min updates may be poor due to high spectrum width, low SNR, etc.

Combining the results of these two chapters, another area where future research could be useful is investigation of adaptive beam spoiling. As mentioned in the conclusions from Chapter 2, radar imaging provides superior data quality for most of the domain, but causes very poor data quality in certain regions due to higher two-way sidelobes. As a result, it may be useful to devise a strategy for adaptively spoiling the transmit beam, similar to Weber et al. (2017), but expanded to meet multiple goals such as spatially variable data quality and temporal update requirements. This could be especially valuable when examining the results from several different types of cases, rather than just a high-impact supercell.

Finally, the ROI^2 model in Chapter 4 shows utility as a proof of concept for adaptive scanning. However, there are several ways in which this model can be improved or expanded. First, the current version of the ROI^2 model only incorporates the data quality of v_r into the cost function; this could be expanded to evaluate the data quality of Z_H and polarimetric variables. Second, the current version of ROI^2 combines the data quality and importance level into a single cost function. In the future, a multi-objective optimization (MOO) should be implemented, as this more accurately balances optimization between multiple (possibly competing) goals. Third, the examples shown are analyzed at one time only, and in two dimensions (i.e., at one elevation). This can be expanded to run at several consecutive times for the same case in order to show spatial and temporal continuity of PR and can be expanded into multiple elevations, such that the same storm and features are assigned the same importance value across multiple elevation angles. Finally, other scan methods such as BMX, radar imaging, and a variable PRT can be assessed in an adaptive environment. Overall, there are many scan-based applications for cognitive radar and adaptive scanning, and the results in Chapter 4 are meant primarily as a proof of concept of how cognitive radar and adaptive scanning principles can improve data quality and/or temporal resolution.

Bibliography

Adachi, T., K. Kusunoki, S. Yoshida, K.-I. Arai, and T. Ushio, 2016: High-speed volumetric observation of a wet microburst using X-band phased array weather radar in Japan. *Mon. Wea. Rev.*, **144**, 3749–3765.

Bell, K. L., G. E. Smith, A. E. Mitchell, and M. Rangaswamy, 2019: Fully adaptive radar for target classification. *2019 IEEE Radar Conf.*, IEEE, Boston, MA.

Bieringer, P. and P. S. Ray, 1996: A comparison of tornado warning lead times with and without NEXRAD Doppler radar. *Wea. Forecasting*, **11**, 47–52.

Bluestein, H. B., M. M. French, I. PopStefanija, R. T. Bluth, and J. B. Knorr, 2010: A mobile, phased-array Doppler radar for the study of severe convective storms: The MWR-05XP. *Bull. Amer. Meteor. Soc.*, **91**, 579–600.

Bluestein, H. B., M. M. French, R. L. Tanamachi, S. Frasier, K. Hardwick, F. Junyent, and A. L. Pazmany, 2007: Close-range observations of tornadoes in supercells made with a dual-polarization, X-band, mobile Doppler radar. *Mon. Wea. Rev.*, **135**, 1522–1543.

Bluestein, H. B., K. J. Thiem, J. C. Snyder, and J. B. Houser, 2018: The multiple-vortex structure of the El Reno, Oklahoma, tornado on 31 May 2013. *Mon. Wea. Rev.*, **146**, 2483–2502.

—, 2019: Tornadogenesis and early tornado evolution in the El Reno, Oklahoma, supercell on 31 May 2013. *Mon. Wea. Rev.*, **147**, 2045–2066.

Bodine, D. J., M. R. Kumjian, R. D. Palmer, P. L. Heinselman, and A. V. Ryzhkov, 2013: Tornado damage estimation using polarimetric radar. *Wea. Forecasting*, **28**, 139–158.

Bodine, D. J., T. Maruyama, R. D. Palmer, C. J. Fulton, H. B. Bluestein, and D. C. Lewellen, 2016a: Sensitivity of tornado dynamics to soil debris loading. *J. Atmos. Sci.*, **73**, 2783–2801.

Bodine, D. J., R. D. Palmer, T. Maruyama, C. J. Fulton, Y. Zhu, and B. L. Cheong, 2016b: Simulated frequency dependence of radar observations of tornadoes. *J. Atmos. Oceanic Technol.*, **33**, 1825–1842.

Bodine, D. J., R. D. Palmer, and G. Zhang, 2014: Dual-wavelength polarimetric radar analyses of tornadic debris signatures. *J. Appl. Meteor. Climatol.*, **53**, 242–261.

Bodine, D. J. and K. L. Rasmussen, 2017: Evolution of mesoscale convective system organizational structure and convective line propagation. *Mon. Wea. Rev.*, **145**, 3419–3440.

Brewster, K. A. and D. S. Zrnić, 1986: Comparison of eddy dissipation rate from spatial spectra of Doppler velocities and Doppler spectrum widths. *J. Atmos. Oceanic Technol.*, **3**, 440–452.

Bringi, V. N. and V. Chandrasekar, 2001: *Polarimetric Doppler Weather Radar*. Cambridge University Press, 636 pp.

Brooks, H. E. and J. Correia Jr., 2018: Long-term performance metrics for National Weather Service tornado warnings. *Wea. Forecasting*, **33**, 1501–1511.

Brown, R. A., L. R. Lemon, and D. W. Burgess, 1978: Tornado detection by pulsed Doppler radar. *Mon. Wea. Rev.*, **106**, 29–38.

Brown, R. A., V. T. Wood, and D. Sirmans, 2002: Improved tornado detection using simulated and actual WSR-88D data with enhanced resolution. *J. Atmos. Oceanic Technol.*, **19**, 1759–1771.

Bryan, G. H. and J. M. Fritsch, 2002: A benchmark simulation for moist nonhydrostatic numerical models. *Mon. Wea. Rev.*, **130**, 2917–2928.

Burgess, D. W., L. R. Lemon, and R. A. Brown, 1975: Tornado characteristics revealed by Doppler radar. *Geophys. Res. Lett.*, **2**, 183–184.

Capraro, G. T., A. Farina, H. Griffiths, and M. C. Wicks, 2006: Knowledge-based radar signal and data processing: A tutorial review. *IEEE Signal Process. Mag.*, **23**, 18–29.

Carbone, R. E., M. J. Carpenter, and C. D. Burghart, 1985: Doppler radar sampling limitations in convective storms. *J. Atmos. Oceanic Technol.*, **2**, 357–361.

Chen, F. and J. Dudhia, 2001: Coupling an advanced land surface-hydrology model with the Penn State-NCAR MM5 modeling system. Part I: Model implementation and sensitivity. *Mon. Wea. Rev.*, **129**, 569–585.

Cheong, B. L., D. J. Bodine, C. J. Fulton, S. M. Torres, T. Maruyama, and R. D. Palmer, 2017: SimRadar: A polarimetric radar time-series simulator for tornadic debris studies. *IEEE Trans. Geosci. Remote Sens.*, **55**, 2858–2870.

Cho, J. Y. N. and J. M. Kurdzo, 2019: Weather radar network benefit model for tornadoes. *J. Appl. Meteor. Climatol.*, **58**, 971–987.

—, 2020: Weather radar network benefit model for tornadoes. *J. Appl. Meteor. Climatol.*, **59**, accepted.

Chrisman, J. N., 2009: Automated volume scan evaluation and termination AVSET: A simple technique to achieve faster volume scan updates for the WSR-88D. *34th Conf. Radar Meteor.*, Amer. Meteor. Soc., Williamsburg, VA, P4.4.

Curtis, C. D. and S. M. Torres, 2011: Adaptive range oversampling to achieve faster scanning on the National Weather Radar Testbed phased-array radar. *J. Atmos. Oceanic Technol.*, **28**, 1581–1597.

Dixon, M. and G. Wiener, 1993: TITAN: Thunderstorm identification, tracking, analysis, and nowcasting–A radar-based methodology. *J. Atmos. Oceanic Technol.*, **10**, 785–797.

Donaldson Jr., R. J., 1970: Vortex signature recognition by a Doppler radar. *J. Appl. Meteor.*, **9**, 661–670.

Doviak, R. J. and D. S. Zrnić, 1993: *Doppler Radar & Weather Observations*. Dover Publications, Inc., 562 pp.

Dowell, D. C., C. R. Alexander, J. M. Wurman, and L. J. Wicker, 2005: Centrifuging of hydrometeors and debris in tornadoes: Radar-reflectivity patterns and wind-measurement errors. *Mon. Wea. Rev.*, **133**, 1501–1524.

Dudhia, J., 1989: Numerical study of convection observed during the winter monsoon experiment using a mesoscale two-dimensional model. *J. Atmos. Sci.*, **46**, 3077–3107.

Efron, B., 1979: Bootstrap methods: Another look at the jackknife. *Ann. Statist.*, **7**, 1–26.

Fang, M., R. J. Doviak, and V. Melnikov, 2004: Spectrum width measured by WSR-88D: Error sources and statistics of various weather phenomena. *J. Atmos. Oceanic Technol.*, **21**, 888–904.

Federal Aviation Administration, 2017: Spectrum efficient national surveillance radar program (SENSR) - Formal request for information (RFI). Preliminary Program Requirements, FAA, [Available from https://faaco.faa.gov/index.cfm/attachment/download/73825].

Forsyth, D. E., J. F. Kimpel, D. S. Zrnić, R. Ferek, J. F. Helmmer, T. McNellis, J. E. Crain, A. M. Shapiro, R. J. Vogt, and W. Benner, 2005: Progress report on the National Weather Radar Testbed (phased-array). *21st International Conf. on Interactive Information Processing Systems (IIPS) for Meteor., Oceanography, and Hydrology*, Amer. Meteor. Soc., San Diego, CA, 19.5.

French, M. M., , P. S. Skinner, L. J. Wicker, and H. B. Bluestein, 2015: Documenting a rare tornado merger observed in the 24 May 2011 El Reno-Piedmont, Oklahoma, supercell. *Mon. Wea. Rev.*, **143**, 3025–3043.

French, M. M., H. B. Bluestein, I. PopStefanija, C. A. Baldi, and R. T. Bluth, 2013: Reexamining the vertical development of tornadic vortex signatures in supercells. *Mon. Wea. Rev.*, **141**, 4576–4601.

—, 2014: Mobile, phased-array, Doppler radar observations of tornadoes at X band. *Mon. Wea. Rev.*, **142**, 1010–1036.

Frisch, A. S. and R. G. Strauch, 1976: Doppler radar measurements of turbulent kinetic energy dissipation rates in a northeastern Colorado convective storm. *J. Appl. Meteor.*, **15**, 1012–1017.

Fulton, C., J. L. Salazar, Y. Zhang, G. Zhang, R. Kelley, J. Meier, M. McCord, D. Schmidt, A. D. Byrd, L. M. Bhowmik, S. Karimkashi, D. S. Zrnić, R. J. Doviak, A. Zahrai, M. Yeary, and R. D. Palmer, 2017: Cylindrical Polarimetric Phased Array Radar: Beamforming and calibration for weather applications. *IEEE Trans. Geosci. Remote Sens.*, **55**, 2827–2841.

Geerts, B., D. Parsons, C. L. Ziegler, T. M. Weckwerth, M. I. Biggerstaff, R. D. Clark, M. C. Coniglio, B. B. Demoz, R. A. Ferrare, W. A. Gallus Jr., K. Haghi, J. M. Hanesiak, P. M. Klein, K. R. Knupp, K. Kosiba, G. M. McFarquhar, J. A. Moore, A. R. Nehrir, M. D. Parker, J. O. Pinto, R. M. Rauber, R. S. Schumacher, D. D. Turner, Q. Wang, X. Wang, Z. Wang, and J. Wurman, 2017: The 2015 plains elevated convection at night field project. *Bull. Amer. Meteor. Soc.*, **98**, 767–786.

Griffin, C. B., D. J. Bodine, J. M. Kurdzo, A. Mahre, and R. D. Palmer, 2019: High-temporal resolution observations of the 27 May 2015 Canadian, Texas, tornado using the Atmospheric Imaging Radar. *Mon. Wea. Rev.*, **147**, 873–891.

Guerci, J. R., 2010: Cognitive radar: A knowledge-aided fully adaptive approach. *2010 IEEE Radar Conf.*, IEEE, Washington, DC.

Haykin, S., 2006: Cognitive radar: A way of the future. *IEEE Signal Process. Mag.*, **23**, 30–40.

Heinselman, P. L., D. S. LaDue, and H. Lazrus, 2012: Exploring impacts of rapid-scan radar data on NWS warning decisions. *Wea. Forecasting*, **27**, 1031–1044.

Heinselman, P. L., D. L. Priegnitz, K. L. Manross, T. M. Smith, and R. W. Adams, 2008: Rapid sampling of severe storms by the National Weather Radar Testbed phased array radar. *Wea. Forecasting*, **23**, 808–824.

Heinselman, P. L. and S. M. Torres, 2011: High-temporal-resolution capabilities of the National Weather Radar Testbed phased-array radar. *J. Appl. Meteor. Climatol.*, **50**, 579–593.

Hong, S.-Y., Y. Noh, and J. Dudhia, 2006: A new vertical diffusion package with an explicit treatment of entrainment processes. *Mon. Wea. Rev.*, **134**, 2318–2341.

Houser, J. L., H. B. Bluestein, and J. C. Snyder, 2015: Rapid-scan, polarimetric, Doppler radar observations of tornadogenesis and tornado dissipation in a tornadic supercell: The El Reno, Oklahoma storm of 24 May 2011. *Mon. Wea. Rev.*, **143**, 2685–2710.

—, 2016: A finescale radar examination of the tornadic debris signature and weak-echo reflectivity band associated with a large, violent tornado. *Mon. Wea. Rev.*, **144**, 4101–4130.

Huang, Y., X. Wang, C. Kerr, A. Mahre, T.-Y. Yu, and D. Bodine, 2020: Impact of assimilating clear-air radial velocity observations on the forecasting of supercell thunderstorm: An observing system simulation experiment study. *Mon. Wea. Rev.*, in review.

Isom, B., R. Palmer, R. Kelley, J. Meier, D. Bodine, M. Yeary, B.-L. Cheong, Y. Zhang, T.-Y. Yu, and M. I. Biggerstaff, 2013: The Atmospheric Imaging Radar: Simultaneous volumetric observations using a phased array weather radar. *J. Atmos. Oceanic Technol.*, **30**, 655–675.

Ivić, I. R., 2018: Effects of phase coding on Doppler spectra in PPAR weather radar. *IEEE Trans. Geosci. Remote Sens.*, **56**, 2043–2065.

Ivić, I. R. and D. Schvartzman, 2020: Weather calibration efforts on the Advanced Technology Demonstrator. *36th Conf. on Environmental Information Processing Techniques*, Amer. Meteor. Soc., Boston, MA, P8.4.

Judy, M., 2020: *Multiple Hypothesis Tracking and Strong Point Analysis for Storm Tracking with Weather Radar*. Master's thesis, University of Oklahoma.

Jung, Y., G. Zhang, and M. Xue, 2008: Assimilation of simulated polarimetric radar data for a convective storm using the ensemble Kalman filter. Part I: Observation operators for reflectivity and polarimetric variables. *Mon. Wea. Rev.*, **136**, 995–1012.

Karimkashi, S. and G. Zhang, 2015: Optimizing radiation patterns of a cylindrical polarimetric phased-array radar for multimissions. *IEEE Trans. Geosci. Remote Sens.*, **53**, 2810–2818.

Kashiwayanagi, T., K. Morotomi, O. Sato, and H. Sugawara, 2016: Rapid 3D scanning high resolution X-band weather radar with active phased array antenna. *WMO Tech. Conf. on Meteor. and Environ. Instrum. and Methods of Obs.*, World Meteor. Assoc., Madrid, Spain, P2(34).

Kumjian, M. R. and A. V. Ryzhkov, 2008: Polarimetric signatures in supercell thunderstorms. *J. Appl. Meteor. Climatol.*, **47**, 1940–1961.

Kurdzo, J. M., D. J. Bodine, B. L. Cheong, and R. D. Palmer, 2015a: High-temporal resolution polarimetric X-band Doppler radar observations of the 20 May 2013 Moore, Oklahoma, tornado. *Mon. Wea. Rev.*, **143**, 2711–2735.

Kurdzo, J. M., B.-L. Cheong, R. D. Palmer, G. Zhang, and J. B. Meier, 2014: A pulse compression waveform for improved-sensitivity weather radar observations. *J. Atmos. Oceanic Technol.*, **31**, 2713–2731.

Kurdzo, J. M., J. Y. N. Cho, B. L. Cheong, and R. D. Palmer, 2019: A neural network approach for waveform generation and selection with multi-mission radar. *2019 IEEE Radar Conf.*, IEEE, Boston, MA.

Kurdzo, J. M., E. F. Joback, P.-E. Kirstetter, and J. Y. N. Cho, 2020: QPE accuracy benefits for weather radar network design. *J. Appl. Meteor. Climatol.*, in review.

Kurdzo, J. M., F. Nai, D. J. Bodine, T. A. Bonin, R. D. Palmer, B.-L. Cheong, J. Lujan, A. Mahre, and A. D. Byrd, 2017: Observations of severe local storms and tornadoes with the Atmospheric Imaging Radar. *Bull. Amer. Meteor. Soc.*, **98**, 915–935.

Kurdzo, J. M., R. D. Palmer, B. L. Cheong, and M. E. Weber, 2015b: Adaptive waveform design for multi-sector array isolation. *2015 European Radar Conf.*, IEEE, Paris, France, 93–96.

Kuster, C. M., P. L. Heinselman, and T. J. Schuur, 2016: Rapid-update radar observations of downbursts occurring within an intense multicell thunderstorm on 14 June 2011. *Wea. Forecasting*, **31**, 827–851.

Lakshmanan, V., K. Hondl, C. K. Potvin, and D. Preignitz, 2013: An improved method for estimating radar echo-top height. *Wea. Forecasting*, **28**, 481–488.

Lawson, J. R., J. S. Kain, N. Yussouf, D. C. Dowell, D. M. Wheatley, K. H. Knopfmeier, and T. A. Jones, 2018: Advancing from convection-allowing NWP to warn-on-forecast: Evidence of progress. *Wea. Forecasting*, **33**, 599–607.

Lewellen, D. C., B. Gong, and W. S. Lewellen, 2008: Effects of finescale debris on near-surface tornado dynamics. *J. Atmos. Sci.*, **65**, 3247–3262.

Mahre, A., C. B. Griffin, Z. B. Weinhoff, H. B. Bluestein, J. B. Houser, J. C. Snyder, and D. J. Bodine, 2019: A study on oscillations in low-level tornado couplet intensity. *35th Conference on Environmental Information Processing Technologies*, Amer. Meteor. Soc., Phoenix, AZ, 825.

Mahre, A., J. M. Kurdzo, D. J. Bodine, C. B. Griffin, R. D. Palmer, and T.-Y. Yu, 2018: Analysis of the 16 May 2015 Tipton, Oklahoma, EF-3 tornado at high spatiotemporal resolution using the Atmospheric Imaging Radar. *Mon. Wea. Rev.*, **146**, 2103–2124.

Mahre, A., T.-Y. Yu, and D. J. Bodine, 2020: A comparison of scan speedup strategies and their effect on rapid-scan weather radar data quality. *J. Atmos. Oceanic Technol.*, accepted pending revisions.

Mahre, A., T.-Y. Yu, R. D. Palmer, and J. M. Kurdzo, 2017: Observations of a cold front at high spatiotemporal resolution using an X-band phased array imaging radar. *Atmosphere*, **8**, 30.

Maruyama, T., 2011: Simulation of flying debris using a numerically generated tornado-like vortex. *J. Wind Eng. Ind. Aerodyn.*, **99**, 249–256.

McLaughlin, D. J., V. Chandrasekar, K. Droegemeier, S. Frasier, J. Kurose, F. Junyent, B. Philips, S. Cruz-Pol, and J. Colom, 2005: Distributed collaborative adaptive sensing (DCAS) for improved detection, understanding, and predicting of atmospheric hazards. *9th Symposium on Integrated Observing and Assimilation Systems for the Atmosphere, Oceans, and Land Surface (IOAS-AOLS)*, Amer. Meteor. Soc., San Diego, CA, P11.3.

Melnikov, V. M., R. J. Doviak, and D. S. Zrnić, 2015: A method to increase the scanning rate of phased-array weather radar. *IEEE Trans. Geosci. Remote Sens.*, **53**, 5634–5643.

Mishchenko, M. I., 2000: Calculation of the amplitude matrix for a nonspherical particle in a fixed orientation. *Appl. Opt.*, **39**, 1026–1031.

Mishchenko, M. I., L. D. Travis, and D. W. Mackowski, 1996: T-matrix computations of light scattering by nonspherical particles: A review. *J. Quant. Spectrosc. Radiat. Transfer*, **55**, 535–575.

Mitchell, A. E., G. E. Smith, K. L. Bell, A. Duly, and M. Rangaswamy, 2018: Fully adaptive radar cost function design. *Proc. 2018 IEEE Radar Conference*, IEEE, Oklahoma City, OK, 1301–1306.

Mlawer, E. J., S. J. Taubman, P. D. Brown, M. J. Iacono, and S. A. Clough, 1997: Radiative transfer for inhomogeneous atmospheres: RRTM, a validated correlated-k model for the longwave. *J. Geophys. Res.*, **102**, 16663–16682.

Nastrom, G. D. and F. D. Eaton, 1997: Turbulence eddy dissipation rates from radar observations at 5-20 km at White Sands Missile Range, New Mexico. *J. Geophys. Res.*, **102**, 19495–19505.

National Research Council, 1995: Assessment of NEXRAD coverage and associated weather services. *Washington, DC: The National Academies Press*, 112 pp.

Newman, J. F. and P. L. Heinselman, 2012: Evolution of a quasi-linear convective system sampled by phased array radar. *Mon. Wea. Rev.*, **140**, 3467–3486.

NOAA OFCM, 2017: WSR-88D meteorological observations. Part C: WSR-88D products and algorithms. Federal meteorological handbook, NOAA OFCM, [Available from https://www.ofcm.gov/publications/fmh/FMH11/fmh11partC.pdf].

Orf, L., 2019: A violently tornadic supercell thunderstorm simulation spanning a quarter-trillion grid volumes: Computational challenges, I/O framework, and visualizations of tornadogenesis. *Atmosphere*, **10**, 578.

Orf, L., R. Wilhelmson, B. Lee, C. Finley, and A. Houston, 2017: Evolution of a long-track violent tornado within a simulated supercell. *Bull. Amer. Meteor. Soc.*, **98**, 45–68.

Orfanidis, S. J., 2016: *Electromagnetic Waves and Antennas*. Sophocles J. Orfanidis, 1413 pp.

Palmer, R. D., C. J. Fulton, J. Salazar, H. Sigmarsson, and M. Yeary, 2019: The "Horus" radar: An all-digital polarimetric phased array radar for multi-mission surveillance. *35th Conference on Environmental Information Processing Technologies*, Amer. Meteor. Soc., Phoenix, AZ, 8A.6.

Park, H., A. Ryzhkov, D. S. Zrnić, and K.-E. Kim, 2009: The hydrometeor classification algorithm for the polarimetric WSR-88D: Description and application to an MCS. *Wea. Forecasting*, **24**, 730–748.

Pazmany, A. L., J. B. Mead, H. B. Bluestein, J. C. Snyder, and J. B. Houser, 2013: A mobile rapid-scanning X-band polarimetric (RaXPol) Doppler radar system. *J. Atmos. Oceanic Technol.*, **30**, 1398–1413.

Pittman, K., A. Mahre, C. B. Griffin, D. Bodine, J. M. Kurdzo, and V. A. Gensini, 2020: Analysis of tornadogenesis failure using rapid-scan data from the Atmospheric Imaging Radar. *Severe Local Storms Symposium*, Amer. Meteor. Soc., Boston, MA, 919.

Polger, P. D., B. S. Goldsmith, R. C. Przywarty, and J. R. Bocchieri, 1994: National Weather Service warning performance based on the WSR-88D. *Bull. Amer. Meteor. Soc.*, **75**, 203–214.

Reinoso-Rondinel, R., T.-Y. Yu, and S. Torres, 2010: Multifunction phased-array radar: Time balance scheduler for adaptive weather sensing. *J. Atmos. Oceanic Technol.*, **27**, 1854–1867.

Romero, R. A. and N. A. Goodman, 2013: Cognitive radar network: Cooperative adaptive beamsteering for integrated search-and-track application. *IEEE Trans. Aerosp. Electron. Syst.*, **49**, 915–931.

Ryzhkov, A. V., T. J. Schuur, D. W. Burgess, and D. S. Zrnić, 2005: Polarimetric tornado detection. *J. Appl. Meteor.*, **44**, 557–570.

Schultz, C. J., L. D. Carey, E. V. Schultz, B. C. Carcione, C. B. Darden, C. C. Crowe, P. N. Gatlin, D. J. Nadler, W. A. Petersen, and K. R. Knupp, 2012: Dual-polarization tornadic debris signatures. Part I: Examples and utility in an operational setting. *Electron. J. Oper. Meteor.*, **13**, 120–137.

Schvartzman, D., S. Torres, and T.-Y. Yu, 2017: Weather radar spatiotemporal saliency: A first look at an information theory-based human attention model adapted to reflectivity images. *J. Atmos. Oceanic Technol.*, **34**, 137–152.

Siggia, A. D. and R. E. Passarelli Jr., 2004: Gaussian Model Adaptive Processing (GMAP) for improved ground clutter cancellation and moment calculation. *3rd European Conf. on Radar in Meteor. and Hydrology*, Copernicus GmBH, Visby, Sweden, 67–73.

Simmons, K. M. and D. Sutter, 2005: WSR-88D radar, tornado warnings, and tornado casualties. *Wea. Forecasting*, **20**, 301–310.

—, 2008: Tornado warnings, lead times, and tornado casualties: An empirical investigation. *Wea. Forecasting*, **23**, 246–258.

Skamarock, W. C., J. B. Klemp, J. Dudhia, D. O. Gill, D. M. Barker, M. G. Duda, X.-Y. Huang, W. Wang, and J. G. Powers, 2008: A description of the advanced research WRF version 3. *NCAR Technical Note NCAR/TN-475+STR*.

Snyder, J. C. and A. V. Ryzhkov, 2015: Automated detection of polarimetric tornadic debris signatures using a hydrometeor classification algorithm. *J. Appl. Meteor. Climatol.*, **54**, 1861–1870.

Sun, J., M. Xue, J. W. Wilson, I. Zawadzki, S. P. Ballard, J. Onvlee-Hooimeyer, P. Joe, D. M. Barker, P.-W. Li, B. Golding, M. Xu, and J. Pinto, 2014: Use of NWP for nowcasting convective precipitation: Recent progress and challenges. *Bull. Amer. Meteor. Soc.*, **95**, 409–426.

Supinie, T. A., N. Yussouf, Y. Jung, M. Xue, J. Cheng, and S. Wang, 2017: Comparison of the analyses and forecasts of a tornadic supercell storm from assimilating phased-array radar and WSR-88D observations. *Wea. Forecasting*, **32**, 1379–1401.

Tanamachi, R. L. and P. L. Heinselman, 2016: Rapid-scan, polarimetric observations of central Oklahoma severe storms on 31 May 2013. *Wea. Forecasting*, **31**, 19–42.

Tanamachi, R. L., P. L. Heinselman, and L. J. Wicker, 2015: Impacts of a storm merger on the 24 May 2011 El Reno, Oklahoma, tornadic supercell. *Wea. Forecasting*, **30**, 501–524.

Thompson, R. L., B. T. Smith, J. S. Grams, A. R. Dean, J. C. Picca, A. E. Cohen, E. M. Leitman, A. M. Gleason, and P. T. Marsh, 2017: Tornado damage rating probabilities derived from WSR-88D data. *Wea. Forecasting*, **32**, 1509–1528.

Torres, S. M., C. D. Curtis, E. Forren, S. Gregg, I. R. Ivić, J. R. Mendoza, D. Schvartzman, C. Schwarz, D. Wasielewski, and A. Zahrai, 2020: An update on the Advanced Technology Demonstrator at the National Severe Storms Laboratory. *36th Conf. on Environmental Information Processing Techniques*, Amer. Meteor. Soc., Boston, MA, P8.1.

Umeyama, A., B. L. Cheong, S. Torres, and D. Bodine, 2018: Orientation analysis of simulated tornadic debris. *J. Atmos. Oceanic Technol.*, **35**, 993–1010.

Van Den Broeke, M. S., 2015: Polarimetric tornadic debris signature variability and debris fallout signatures. *J. Appl. Meteor. Climatol.*, **54**, 2389–2405.

—, 2017: Potential tornado warning improvement resulting from utilization of the TDS in the warning decision process. *J. Oper. Meteor.*, **5**, 121–133.

Van Den Broeke, M. S. and S. T. Jauernic, 2014: Spatial and temporal characteristics of polarimetric tornadic debris signatures. *J. Appl. Meteor. Climatol.*, **53**, 2214–2231.

Wakimoto, R. M., N. T. Atkins, K. M. Butler, H. B. Bluestein, K. Thiem, J. Snyder, and J. Houser, 2015: Photogrammetric analysis of the 2013 El Reno tornado combined with mobile X-band polarimetric radar data. *Mon. Wea. Rev.*, **143**, 2657–2683.

Wakimoto, R. M., N. T. Atkins, K. M. Butler, H. B. Bluestein, K. Thiem, J. C. Snyder, J. Houser, K. Kosiba, and J. Wurman, 2016: Aerial damage survey of the 2013 El Reno tornado combined with mobile radar data. *Mon. Wea. Rev.*, **144**, 1749–1776.

Wakimoto, R. M., Z. Wienhoff, H. B. Bluestein, D. J. Bodine, and J. M. Kurdzo, 2020: Mobile radar observations of the evolving debris field compared with a damage survey of the Shawnee, Oklahoma tornado of 19 May 2013. *Mon. Wea. Rev.*, in press.

Wang, Y. and V. Chandrasekar, 2010: Quantitative precipitation estimation in the CASA X-band dual-polarization radar network. *J. Atmos. Oceanic Technol.*, **27**, 1665–1676.

Wang, Y. and T.-Y. Yu, 2015: Novel tornado detection using an adaptive neuro-fuzzy system with S-band polarimetric weather radar. *J. Atmos. Oceanic Technol.*, **32**, 195–208.

Wang, Y., T.-Y. Yu, M. Yeary, A. Shapiro, S. Nemati, M. Foster, D. L. Andra Jr., and M. Jain, 2008: Tornado detection using a neuro-fuzzy system to integrate shear and spectral signatures. *J. Atmos. Oceanic Technol.*, **25**, 1136–1148.

Weber, M. E., 2019: Meteorological phased array radar research at NOAA's National Severe Storms Laboratory. *2019 IEEE International Conf. on Microwaves, Antennas, Communications, and Electronic Systems (COMCAS)*, IEEE, Tel-Aviv, Israel.

Weber, M. E., J. Y. N. Cho, J. S. Herd, J. M. Flavin, W. E. Benner, and G. S. Torok, 2007: The next-generation multimission U.S. surveillance radar network. *Bull. Amer. Meteor. Soc.*, **88**, 1739–1751.

Weber, M. E., J. Y. N. Cho, and H. G. Thomas, 2017: Command and control for multifunction phased array radar. *IEEE Trans. Geosci. Remote Sens.*, **55**, 5899–5912.

Weber, M. E. and J. S. Herd, 2019: Aperture size considerations for future operational phased array weather radar. *35th Conf. on Environmental Information Processing Technologies*, Amer. Meteor. Soc., Phoenix, AZ, 7A.4.

Weber, M. E., V. Melnikov, D. Zrnić, K. Hondl, R. R. Zellner, and B. Hudson, 2020: Experimental validation of the multibeam technique for rapid-scan, meteorological phased-array radar. *36th Conf. on Environmental Information Processing Techniques*, Amer. Meteor. Soc., Boston, MA, P8.3.

Weber, M. E., J. Pica, C. D. Curtis, I. R. Ivic, D. Conway, and J. Y. N. Cho, 2019: Panel discussion: The next-generation operational weather radar network. *Phased Array Radar Symposium*, Amer. Meteor. Soc., Phoenix, AZ, PD1.1.

Wilson, K. A., P. L. Heinselman, C. M. Kuster, D. M. Kingfield, and Z. Kang, 2017: Forecaster performance and workload: Does radar update time matter? *Wea. Forecasting*, **32**, 253–274.

Wolfson, M. M. and C. A. Meuse, 1993: Quantifying airport terminal area weather surveillance requirements. Preprints, *26th International Conf. on Radar Meteor.*, Amer. Meteor. Soc., Norman, OK, 47–49.

Wurman, J. and K. Kosiba, 2013: Finescale radar observations of tornado and mesocyclone structures. *Wea. Forecasting*, **28**, 1157–1174.

Wurman, J., K. Kosiba, P. Robinson, and T. Marshall, 2014: The role of multiple-vortex tornado structure in causing storm researcher fatalities. *Bull. Amer. Meteor. Soc.*, **95**, 31–45.

Wurman, J. and M. Randall, 2001: An inexpensive, mobile, rapid-scan radar. *30th Int. Conf. on Radar Meteor.*, Amer. Meteor. Soc., Munich, Germany, P3.4.

Yu, T.-Y., M. S. McCord, J. L. Salazar, C. Fulton, R. D. Palmer, and H. B. Bluestein, 2019: Development of a shared mobile C-band Polarimetric Atmospheric Imaging Radar (PAIR). *39th International Conf. on Radar Meteor.*, Amer. Meteor. Soc., Nara, Japan, 2–07.

Yu, T.-Y., M. B. Orescanin, C. D. Curtis, D. S. Zrnić, and D. E. Forsyth, 2007: Beam multiplexing using the phased-array weather radar. *J. Atmos. Oceanic Technol.*, **24**, 616–626.

Yussouf, N. and D. J. Stensrud, 2010: Impact of phased-array radar observations over a short assimilation period: Observing system simulation experiments using an ensemble Kalman filter. *Mon. Wea. Rev.*, **138**, 517–538.

Zhang, G., R. J. Doviak, D. S. Zrnić, R. Palmer, L. Lei, and Y. Al-Rashid, 2011: Polarimetric phased-array radar for weather measurement: A planar or cylindrical configuration? *J. Atmos. Oceanic Technol.*, **28**, 63–73.

Zhang, G., J. Vivekanandan, and E. Brandes, 2001: A method for estimating rain rate and drop size distribution from polarimetric radar measurements. *IEEE Trans. Geosci. Remote Sens.*, **39**, 830–841.

Zhang, P., P. W. Chan, R. Doviak, and M. Fang, 2009: Estimate of the eddy dissipation rate using spectrum width observed by the Hong Kong TDWR radar. *Proc. 34th Conf. on Radar Meteor.*, Amer. Meteor. Soc., Williamsburg, VA, P6.9.

Zrnić, D. S., 1977: Spectral moment estimates from correlated pulse pairs. *IEEE Trans. Aerosp. Electron. Syst.*, **AES-13**, 344–354.

Zrnić, D. S., J. F. Kimpel, D. E. Forsyth, A. Shapiro, G. Crain, R. Ferek, J. Heimmer, W. Benner, T. J. McNellis, and R. J. Vogt, 2007: Agile-beam phased array radar for weather observations. *Bull. Amer. Meteor. Soc.*, **88**, 1753–1766.

Zrnić, D. S., V. M. Melnikov, R. J. Doviak, and R. Palmer, 2015: Scanning strategy for the multifunction phased-array radar to satisfy aviation and meteorological needs. *IEEE Geosci. Remote Sens. Letters*, **12**, 1204–1208.

Appendix A

Effect of Beam Multiplexing on Radar Reflectivity Factor Variance Distribution

This section is intended to provide a more complete mathematical explanation of why the histogram shape for RMSE($\hat{Z}_H$) looks distinctly different when scanning using BMX, rather than CPS data collection mode. By qualitatively analyzing Fig. 2.4 it is clear that when scanning in BMX data collection mode, the histogram of RMSE($\hat{Z}_H$) is much narrower than that of the other histograms in Fig. 2.4.

First, we can analyze the right-hand side of (2.3), re-written here:

$$\frac{\mathrm{var}(\hat{S}_C)}{S^2} = \frac{1}{P}\left[\sum_{l=-(P-1)}^{P-1} \frac{P-|l|}{P}\rho^2(lT_s) + \frac{N^2}{S^2} + 2\frac{N}{S}\right] \tag{A.1}$$

As a reminder, P is the number of pulses, T_s is the pulse repetition time (PRT), ρ is the normalized autocorrelation function, S is the signal power, N is the noise power, and $\hat{S}$ is the estimator for signal power. If we take the high-SNR limit (such that the last two terms in brackets are treated as negligible), the equation reduces to

$$\mathrm{var}(\hat{S}_C) = S^2\left[\sum_{l=-(P-1)}^{P-1} \frac{P-|l|}{P^2}\rho^2(lT_s)\right] \tag{A.2}$$

However, the term in brackets is simply $\frac{1}{P_I}$, where P_I is the number of independent samples obtained, so the equation reduces further, to

$$\mathrm{var}(\hat{S}_C) = S^2\left[\frac{1}{P_I}\right] \tag{A.3}$$

where P_I is a function of spectrum width and the total number of pulses transmitted. By performing a similar analysis (i.e., taking the high-SNR limit) of (2.6), we find that (2.6) reduces to

$$\mathrm{var}(\hat{S}_I) = S^2\left[\frac{(1+\rho^2)}{P}\right] \tag{A.4}$$

Now, the two equations can be analyzed in the limit of both high and low interpulse correlation. In the low interpulse correlation regime (i.e., $\rho = 0$ and $P_I = P$) where all pulses are entirely independent of one another, (A.3) and (A.4) both reduce to $\mathrm{var}(\hat{S}) = \frac{S^2}{P}$. This result makes intuitive sense; if all pulses are already entirely independent, then BMX should not offer any further reduction in variance, because the number of pulses (P) is already equal to the number of independent pulses (P_I).

In the high interpulse correlation limit (i.e., $\rho = 1$ and $P_I = 1$), two pulses in the same pulse pair are assumed to be entirely correlated, but the time between successive pulse pairs is long enough such that each pulse pair is considered independent. Making this assumption, (A.3) reduces to $\mathrm{var}(\hat{S}_C) = S^2$, while (A.4) reduces to $\mathrm{var}(\hat{S}_I) = S^2(\frac{2}{P})$.

This has significant implications for the shape of the histogram of CPS data collection compared to BMX/IPS data collection mode. The variance of $\hat{S}$ in CPS data collection mode is proportional to $\frac{S^2}{P}$ in the low ρ limit, and is proportional to S^2 in the high ρ limit. This corresponds to a P-fold range in values of variance (i.e., x to Px). For BMX/IPS data collection mode, the variance of $\hat{S}$ is proportional to

$\frac{S^2}{P}$ in the low ρ limit, and is proportional to $2\frac{S^2}{P}$ in the high ρ limit. This yields only a two-fold range of values in variance (x to $2x$), which is significantly smaller than that of CPS data collection mode (assuming $P >> 2$). This is the reason why the histogram shape of RMSE($\hat{Z}_H$) is noticeably narrower for BMX data collection.